A NOVEL ARRAY SIGNAL PROCESSING TECHNIQUE FOR MULTIPATH CHANNEL PARAMETER ESTIMATION

A THESIS

SUBMITTED TO THE DEPARTMENT OF ELECTRICAL AND

ELECTRONICS ENGINEERING

AND THE INSTITUTE OF ENGINEERING AND SCIENCES

OF BILKENT UNIVERSITY

IN PARTIAL FULFILLMENT OF THE REQUIREMENTS

FOR THE DEGREE OF

MASTER OF SCIENCE

By

Mehmet Burak Güldoğan

July 2006

I certify that I have read this thesis and that in my opinion it is fully adequate, in scope and in quality, as a thesis for the degree of Master of Science.

Prof. Dr. Orhan Arıkan(Supervisor)

I certify that I have read this thesis and that in my opinion it is fully adequate, in scope and in quality, as a thesis for the degree of Master of Science.

Prof. Dr. Enis Çetin

I certify that I have read this thesis and that in my opinion it is fully adequate, in scope and in quality, as a thesis for the degree of Master of Science.

Asst. Prof. Dr. İbrahim Körpeoğlu

Approved for the Institute of Engineering and Sciences:

Prof. Dr. Mehmet Baray
Director of Institute of Engineering and Sciences

ABSTRACT

A NOVEL ARRAY SIGNAL PROCESSING TECHNIQUE FOR MULTIPATH CHANNEL PARAMETER ESTIMATION

Mehmet Burak Güldoğan
M.S. in Electrical and Electronics Engineering
Supervisor: Prof. Dr. Orhan Arıkan
July 2006

Many important application areas such as mobile communication, radar, sonar and remote sensing make use of array signal processing techniques. In this thesis, a new array processing technique called **C**ross **A**mbiguity **F**unction - **D**irection **F**inding (CAF-DF) is developed. CAF-DF technique estimates direction of arrival (DOA), time delay and Doppler shift corresponding to each impinging signals onto a sensor array in an iterative manner. Starting point of each iteration is CAF computation at the output of each sensor element. Then, using incoherent integration of the computed CAFs, the strongest signal in the delay-Doppler domain is detected and based on the observed phases of the obtained peak across all the sensors, the DOA of the strongest signal is estimated. Having found the DOA, CAF of the coherently integrated sensor outputs is computed to find accurate delay and Doppler estimates for the strongest signal. Then, for each sensor in the array, a copy of the strongest signal that should be observed at that sensor is constucted and eliminated from the sensor output to start the next iteration. Iterations continue until there is no detectable peak on the incoherently integrated CAFs. The proposed technique is compared with a MUSIC based

technique on synthetic signals. Moreover, performance of the algorithm is tested on real high-latitude ionospheric data where the existing approaches have limited resolution capability of the signal paths. Based on a wide range of comparisons, it is found that the proposed CAF-DF technique is a strong candidate to define the new standard on challenging array processing applications.

Keywords: Array signal processing, direction of arrival (DOA), MUSIC, delay and Doppler estimation, cross ambiguity function

ÖZET

ÇOKLUYOL KANAL PARAMETRE KESTİRİMİ İÇİN YENİ BİR DİZİ SİNYAL İŞLEME TEKNİĞİ

Mehmet Burak Güldoğan
Elektrik ve Elektronik Mühendisliği Bölümü Yüksek Lisans
Tez Yöneticisi: Prof. Dr. Orhan Arıkan
Temmuz 2006

Mobil haberleşme, radar, sonar ve uzaktan algılama gibi bir çok önemli uygulamada, dizi sinyal işleme tekniklerinden faydalanılır. Bu tezde, **Ç**arpraz **B**elirsizlik **F**onksiyonu - **Y**ön **B**ulma (ÇBF-YB) adında yeni bir dizi işleme tekniği geliştirilmiştir. ÇBF-YB tekniği, bir algılayıcı dizisine gelen sinyallerden herbirinin geliş yönünü (GY), zaman gecikmesini ve Doppler kaymasını yinelemeli bir şekilde kestirir. Herbir algılayıcı çıktısındaki ÇBF hesaplaması, yinelemelerin başlangıç noktasını oluşturur. Daha sonra, ÇBF'lerin faz uyumsuz bir şekilde entegrasyonunu kullanarak, gecikme-Doppler alanındaki en güçlü sinyal tespit edilir ve tüm algılayıcılarda elde edilen tepe noktalarında gözlemlenen fazlar esas alınarak en güçlü sinyalin GY'si kestirilir. GY'yi bulduktan sonra, en güçlü sinyalin gecikme ve Doppler kaymasını kestirmek için, uyumlu entegre edilmiş dizi çıktısının ÇBF'si hesaplanır. Takiben, dizideki herbir algılayıcı için, aygılayıcıda gözlemlenmesi gereken en güçlü sinyalin bir kopyası oluşturulur ve bir sonraki yinelemeyi başlatmak için algılayıcı çıktısından çıkarılır. Faz uyumsuz olarak entegre edilmiş ÇBF'ler üzerinde algılanabilecek tepe noktası kalmayıncaya kadar yinelemeler devam eder. Sentetik olarak oluşturulmuş sinyaller kullanılarak önerilen teknik ile MUSIC tabanlı tekniğin karşılaştırılması yapılmıştır.

Ek olarak, algoritmanın peformansı, literatürdeki yaklaşımların sinyal yollarını ayırmada sınırlı kabiliyetlere sahip olduğu gerçek yüksek-enlem iyonosfer verileri üzerinde test edilmiştir. Geniş bir yelpazede yapılan kıyaslamalara göre, ÇBF-YB tekniği karmaşık dizi işleme uygulamalarında standartları belirleyebilecek güçlü bir adaydır.

Anahtar Kelimeler: Dizi sinyal işleme, geliş yönü (GY), MUSIC, zaman gecikmesi ve Doppler kayması kestirimi, çarpraz belirsizlik fonksiyonu

ACKNOWLEDGMENTS

I would like to express my thanks and gratitude to my supervisor Prof. Dr. Orhan Arıkan for his supervision, suggestions and invaluable encouragement throughout the development of this thesis. He is not only the best advisor that I have seen but also a role model as a researcher and a teacher to me. His intuition to see and solve a problem was amazing to me and it was a big pleasure to be advised by him.

I wish to thank Dr. Mike Warrington and his research group at the University of Leicester for the HF data, processing codes and for permission to use them in this thesis.

Special thanks to Prof. Dr. Feza Arıkan, Prof. Dr. Enis Çetin, and Asst. Prof. Dr. İbrahim Körpeoğlu, for their valuable comments and suggestions on the thesis.

I would like to thank Assoc. Prof. Dr. Ezhan Karaşan, Assoc. Prof. Dr. Nail Akar and Güray Gürel for their help and support in using the facilities at BINLAB.

I would also like to thank my colleagues in TÜBİTAK-UEKAE for their support and encouragement during my graduate study.

Finally, I would like to say thanks to my mother,Gündüz, and my sister,Berrak, for always believing in me and encouraging me to achieve my goals. My deepest gratitude goes to my wife, Seher, for her support and love which have been invaluable in helping me focus on my academic pursuits.

Contents

List of Figures

List of Tables

To the memory of my father ...

Chapter 1

INTRODUCTION

1.1 Objective and Contributions of this Work

Recent advances in wireless communication resulted in significant improvement in our living standards. Information transmission can be achieved via several ways by using electromagnetic, sonar, acoustic, or seismic waves as the carrier. In addition to wireless communications, radar applications also process information that bounced back from targets to deduce their position and velocity. To obtain best results, sensor arrays are widely used [1].

Compared to single sensor systems, array systems have some crucial advantages. First of all, for an M-sensor array, by proper processing of the received signal signal-to-noise ratio (SNR) can be increased by M times . Secondly, beams of the array can be steered freely in any desired directions. Flexible steering ability enables wireless equipment to separate multiple signals and suppress intentional or unintentional interference.

Array signal parameter estimation is a very popular research field of focus by applied statisticians and engineers as problems required ever improving performance. Direction of arrival (DOA) is one of the most important parameters which plays a crucial role in many real life applications. In radar, estimation of the DOA is a main issue in localization and tracking of targets. Moreover, in multi-user mobile communications, generally waves reach the receiver within a delay interval shorter than the resolution. In these cases, DOA estimates can provide spatial diversity to the receiver to enable reliable communication in multi-user scenarios [2]. Because of its importance, wide variety of algorithms have been proposed for reliable estimation of DOAs . Initial trials of signal source localization using arrays was through beamforming techniques. The idea is to form a beam in the direction of waves coming from only one particular direction. The steering directions which result in maximum signal power yields the DOA estimates [3]. Subspace methods are very well known DOA estimation techniques with high performance and relatively low computational cost. These methods basically make use of the eigen-structure of the covariance matrix of observed signals from the sensor array. The most commonly used technique in this family is the MUSIC (Multiple SIgnal Classification) technique [4, 5]. Although, mentioned approaches are very efficient in terms of computational power, they do not provide enough accuracy in correlated signal scenarios. On the otherhand, maximum likelihood (ML) techniques are highly accurate but computationally quite intensive [6, 7, 8, 9, 10]. Most recent subspace fitting methods such as signal subspace fitting (SSF) and noise subspace fitting (NSF) have the same statistical performance as the ML methods with a less computational cost [11, 12, 13]. Recently, there are some efforts dealing with the DOA estimation for chirp signals by making use of ambiguity function [14, 15]. The method called AMBIGUITY-DOMAIN MUSIC (AD-MUSIC) in [14], uses the spatial ambiguity function (SAF) of the sensor array output. Once the noise subspace of the SAF matrix is estimated, the technique estimates the DOA's

by finding the largest peaks of a localization function. In [15], details of two broadband DOA estimation methods for chirp signals based on the ambiguity function is introduced. Most of these methods take advantage of the fact that there is only a phase difference between sensor outputs, when the signals are narrowband.

Estimating the time delays and Doppler shifts of a known waveform by an array of antennas is another crucial aspect of the signal parameter estimation. For instance, in active radar and sonar, a known signal is transmitted and reflections from targets are received. The received signals are generally modeled as delayed, Doppler-shifted and scaled versions of the transmitted one. Estimation of the delay and Doppler-shift enables us to gather information about the position and the radial velocities of targets. Secondly, estimation of the parameters of the multipath communication channel, in cases where the transmitter has a rapid movement or has an unknown frequency offset, is another important application. Accurate delay and Doppler estimations are very critical in establishing a reliable communication link. Classical techniques to time-delay and Doppler estimation are based on matched filtering [16]. Matched filtering techniques are optimal for single signal arrival but are not good when multiple overlapping copies of the signal are present. In [17], a deconvolution approach for resolving multiple delayed and Doppler shifted paths where path parameters are constrained to a quantized grid is presented. Alternatively, two popular and efficient algorithms called signal subspace fitting (SSF) and noise subspace fitting (NSF), which also provide promising results when correlated signals received, can be found in [11].

In this thesis, a new signal parameter estimation technique called CAF-DF (**C**ross **A**mbiguity **F**unction - **D**irection **F**inding) based on the cross-ambiguity function calculation will be presented. CAF-DF technique estimates DOA, time delay and Doppler shift corresponding to one of the impinging signals onto the

array in an iterative manner. Starting point of each iteration is CAF computation at the output of each sensor element. Then, these 2D CAF matrixes are incoherently integrated and the largest peak on the integrated CAF is found. After that, DOA for the observed signal peak is estimated. Having found the DOA, CAF of the coherently integrated sensor outputs is computed to find accurate delay and Doppler estimates for the strongest signal. Then, the signal whose parameters are estimated is eliminated from the array outputs to search for the next strong signal component in the residual array outputs. Iterations continue until there is no detectable peak on the incoherently integrated CAFs.

CAF-DF is different from the mentioned techniques because it both uses coherent and incoherent integration of data. It performs significantly better than the MUSIC in simulations. Especially in difficult scenarios involving low SNR and highly correlated signals, resolution capability of the CAF-DF is very promising. Moreover, there are three important differences between CAF-DF and mentioned ambiguity function based techniques [14, 15]. First of all, there isn't any requirement to use chirp signals. Secondly, there is no need to use any other estimation technique. Lastly, CAF-DF uses cross ambiguity function instead of auto ambiguity function.

1.2 Organization of the Thesis

The organization of the thesis is as follows. In Chapter 2, a general parametric data model, which is used throughout the thesis, is introduced for sensor array systems. Then formulation and some important properties of the matched filter and ambiguity function are given. Lastly, some commonly used applications of array signal processing is presented.

In Chapter 3, spectral-based algorithmic solutions and parametric methods of DOA estimation for narrowband signals in array signal processing are presented.

In Chapter 4, basics of HF communication is introduced.The theory of wave propagation through the ionosphere is briefly discussed.

The novel DOA, delay and Doppler estimation algorithm, CAF-DF, is introduced in Chapter 5. Following the basic theory, detailed formulation of the CAF-DF technique is given.

The theory of an alternative MUSIC based approach proposed for HF-DF is discussed in Chapter 6. After that, simulation results and comparisons for different scenarios with the CAF-DF is presented.

Chapter 7 presents the estimated parameters of a real ionospheric data using CAF-DF and MUSIC based approach.

Finally, Chapter 8 concludes the thesis by highlighting the contributions made and list of work for future research on the subject.

Chapter 2

BASICS OF ARRAY SIGNAL PROCESSING

The basics of array signal processing is briefly discussed in this chapter. First, underlying parametric data model for sensor arrays is introduced. Then some important points of matched filter and ambiguity function is presented. Lastly, applications of array processing are discussed.

2.1 Parametric Data Model for Sensor Arrays

Sensor arrays consists of a set of sensors that are spatially distributed at known locations with reference to a common reference point [18]. A sensor may be represented as a point receiver. The propagating signals are simultaneously sampled and collected by each sensor. The source waveforms undergo some modifications, depending on the path of propagation and the sensor characteristics. In this section a general parametric model will be given.

Usually, the direction and the speed of the propagation are defined by a vector $\boldsymbol{\alpha}$ in (2.11) which is called the *slowness vector*. Using the reference coordinate

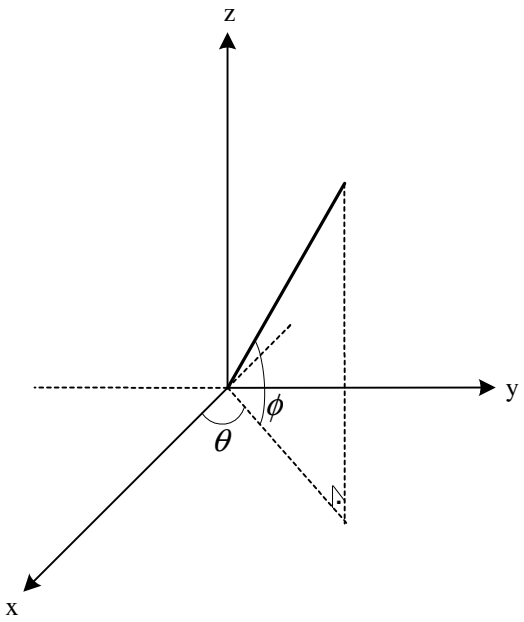

Figure 2.1: Direction of the signal and reference coordinate system.

system in Fig. 2.1, the slowness vector is

$$\boldsymbol{\alpha} = \frac{1}{c}[\cos\phi\cos\theta\ ;\ \cos\phi\sin\theta\ ;\ \sin\phi] \quad , \tag{2.1}$$

where θ is the azimuth angle, ϕ is the elevation angle and c is the speed of light. A circular array geometry is depicted in Fig. 2.2. Position of each sensor is represented by vector $\boldsymbol{r_m} = [x_m\ ;\ y_m\ ;\ z_m] = [r_m\sin(\theta_m)\ ;\ r_m\cos(\theta_m)\ ;\ 0]$ and the propagation direction of each impinging signal is represented by unit vector $\boldsymbol{\alpha}_i = (1/c)[x_i\ ;\ y_i\ ;\ z_i]$, and $i = 1, ..., d$ is the signal index. Using Eqn. 2.1, the field measured at sensor m due to a source whose DOA is (θ_i, ϕ_i), can be written as

$$E(\boldsymbol{r_m}, t) = s(t)e^{jw(t-\xi_{m,i})} \tag{2.2}$$

where $s(t)$ is the data signal and $\xi_{m,i}$ is the relative phase of the m^{th} sensor due to i^{th} impinging signal with respect to the origin of the sensor array. This phase can be written in cartesian coordinates as

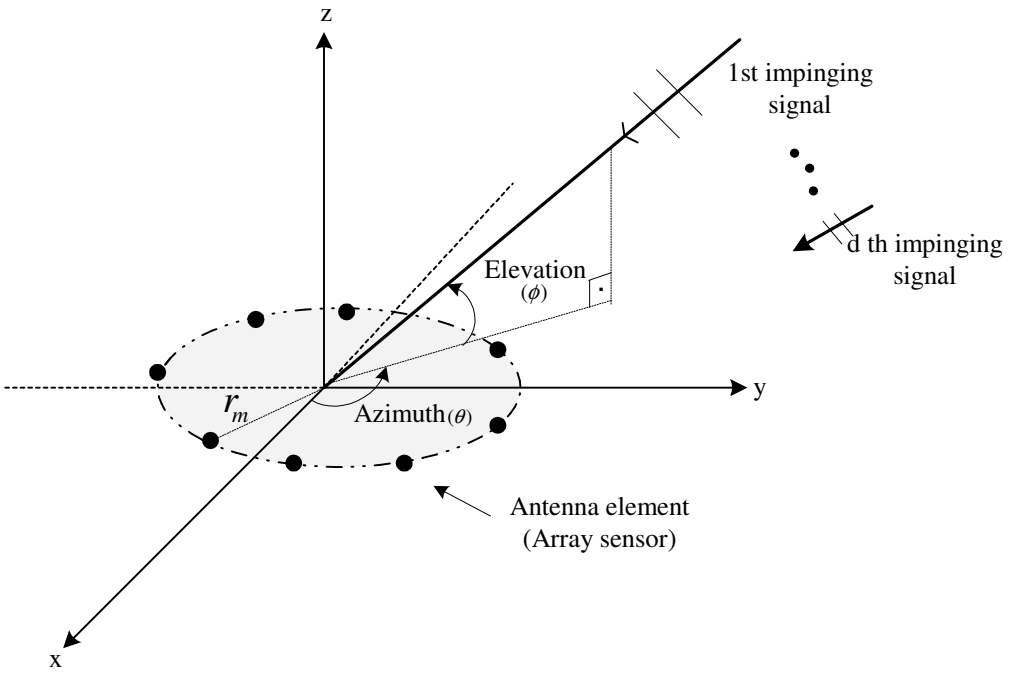

Figure 2.2: Circular array and multipath enviroment.

$$\begin{aligned}\xi_{m,i}(\theta,\phi) &= \boldsymbol{\alpha}_i \cdot \boldsymbol{r_m} \\ &= \frac{1}{c}\begin{bmatrix}\cos(\theta_i)\cos(\phi_i)\\ \sin(\theta_i)\cos(\phi_i)\\ \sin(\phi_i)\end{bmatrix}\cdot\begin{bmatrix}r_m\cos(\theta_m)\\ r_m\sin(\theta_m)\\ 0\end{bmatrix} \\ &= \frac{1}{c}\left[r_m\cos(\theta_i)\cos(\phi_i)\cos(\theta_m) + r_m\sin(\theta_i)\cos(\phi_i)\sin(\theta_m)\right] \quad . \end{aligned} \tag{2.3}$$

In practice, before sampling takes place, the signal is down-converted to baseband which will be discussed in the following section. Therefore, without the carrier term $\exp(jwt)$, the output is modeled by

$$x_m(t) = a_m(\theta,\phi)s(t) \quad . \tag{2.4}$$

For an M-element antenna array, the array output vector is obtained as

$$\mathbf{x}(t) = \mathbf{a}(\theta,\phi)s(t) \quad . \tag{2.5}$$

where $\mathbf{a}(\theta,\phi)$ is called the *steering vector*. Assuming a linear receiving system, if G signals impinge on an M-dimensional array from distinct DOAs

$(\theta_1, \phi_1), ..., (\theta_d, \phi_d)$ the output vector takes the form

$$\mathbf{x}(t) = \sum_{i=1}^{d} \mathbf{a}(\theta_i, \phi_i) s_i(t) \quad , \tag{2.6}$$

where $s_i(t)$, denote the i^{th} baseband signal. Last equation, can be written in a more compact form by defining a *steering matrix* and a vector of signal waveforms as

$$\mathbf{A}(\theta, \phi) = \left[\mathbf{a}(\theta_1, \phi_1), ..., \mathbf{a}(\theta_d, \phi_d)\right]_{(M \times d)} \tag{2.7}$$

$$\mathbf{s}(t) = \left[s_1(t); ...; s_d(t)\right] \quad . \tag{2.8}$$

Moreover, in the presence of noise $\mathbf{n}$(t) we reach the well-known representation for the array input output relation;

$$\mathbf{x}(t) = \mathbf{A}(\theta, \phi)\mathbf{s}(t) + \mathbf{n}(t) \quad . \tag{2.9}$$

The signal parameters in this thesis are spatial in nature, so the following *spatial covariance matrix* plays an important role:

$$\mathbf{R} = E\{\mathbf{x}(t)\mathbf{x}^H(t)\} = \mathbf{A}E\{\mathbf{s}(t)\mathbf{s}^H(t)\}\mathbf{A}^H + E\{\mathbf{n}(t)\mathbf{n}^H(t)\} \tag{2.10}$$

where E denotes expected value operation,

$$E\{\mathbf{s}(t)\mathbf{s}^H(t)\} = \mathbf{P} \tag{2.11}$$

can be called source covariance matrix and

$$E\{\mathbf{n}(t)\mathbf{n}^H(t)\} = \sigma^2\mathbf{I} \tag{2.12}$$

is the noise covariance matrix. At all sensors we have an uncorrelated and spatially white receiver noise which has variance σ^2 and is assumed to have circularly symmetric Gaussian distribution.

In a more compact form, (2.10) can be written as

$$
\begin{aligned}
\mathbf{R} &= \mathbf{A}\mathbf{P}\mathbf{A}^H + \sigma^2\mathbf{I} \qquad (2.13)\\
&= \mathbf{U}\mathbf{\Lambda}\mathbf{U}^H \\
&= \begin{bmatrix}\mathbf{u}_1 \ \dots \ \mathbf{u}_d \ , \ \mathbf{u}_{d+1} \ \dots \ \mathbf{u}_M\end{bmatrix}
\begin{bmatrix}
\mu_1+\sigma^2 & & & & & & \\
& \ddots & & & & & \\
& & \mu_d+\sigma^2 & & & & \\
& & & \sigma^2 & & & \\
& & & & \ddots & & \\
& & & & & \sigma^2 &
\end{bmatrix}
\begin{bmatrix}\mathbf{u}_1^H \\ \vdots \\ \mathbf{u}_d^H \\ \mathbf{u}_{d+1}^H \\ \vdots \\ \mathbf{u}_M^H\end{bmatrix} \\
&= \begin{bmatrix}\mathbf{U}_s \ , \ \mathbf{U}_n\end{bmatrix}
\begin{bmatrix}\mathbf{\Lambda}_s+\sigma^2\mathbf{I} & \mathbf{0} \\ \mathbf{0} & \sigma^2\mathbf{I}\end{bmatrix}
\begin{bmatrix}\mathbf{U}_s^H \\ \mathbf{U}_n^H\end{bmatrix} \\
&= \mathbf{U}_s\mathbf{\Lambda}_s\mathbf{U}_s^H + \sigma^2\mathbf{U}_s\mathbf{U}_s^H + \sigma^2\mathbf{U}_n\mathbf{U}_n^H \\
&= \mathbf{U}_s\mathbf{\Lambda}_s\mathbf{U}_s^H + \mathbf{U}_n\mathbf{\Lambda}_n\mathbf{U}_n^H
\end{aligned}
$$

where $\mathbf{\Lambda}$ is a diagonal matrix with real eigenvalues and $\mathbf{U}$ is a unitary matrix. From the equation above, it is easily seen that

$$\mathbf{A}\mathbf{P}\mathbf{A}^H = \mathbf{U}_s\mathbf{\Lambda}_s\mathbf{U}_s^H \quad . \qquad (2.14)$$

This says that the span of the columns of $\mathbf{A}$ is equal to the span of the columns of $\mathbf{U}_s$ (assuming that $\mathbf{A}$ and $\mathbf{P}$ are full rank). The eigenvectors associated with the first d eigenvalues of $\mathbf{R}$ are the same as the eigenvectors of $\mathbf{A}\mathbf{P}\mathbf{A}^H$. These eigenvectors constitute the *signal subspace*. The eigenvectors associated with the remaining $M-d$ eigenvalues of $\mathbf{R}$ constitute the *noise subspace* and are orthogonal to the signal subspace.

Throughout the thesis, the number of underlying signals, d, is assumed to be known. Otherwise, we can use the techniques presented in [19, 20, 21] to estimate the number of signals impinging onto the sensor array.

2.2 Matched Filter and the Ambiguity Function

A matched filter can be defined as a type of filter matched to the known or assumed characteristics of a target signal, designed to optimize the detection of that signal in the presence of noise [22]. In the case of white additive noise, the highest SNR at the detector is obtained when the received signal is correlated with the replica of the transmitted signal. In this section, firstly complex envelopes of the narrow bandpass signals, which make the design of the matched filter simple, will be described. After that, basics of the matched filter and how we get to the ambiguity function will be discussed.

Narrowband bandpass signals can be represented in several ways. The simplest one is

$$s(t) = g(t)\cos[\omega_c t + \Phi(t)] \tag{2.15}$$

where $\Phi(t)$ is the instantaneous phase and $g(t)$ is the envelope of $s(t)$. Second form is

$$s(t) = g_c(t)\cos(\omega_c t) - g_s(t)\sin(\omega_c t) \tag{2.16}$$

where $g_c(t)$ and $g_s(t)$ are the *in-phase* and *quadrature* baseband components, respectively, and represented as follows

$$g_c(t) = g(t)\cos(\Phi(t)) \tag{2.17}$$

$$g_s(t) = g(t)\sin(\Phi(t)) \quad . \tag{2.18}$$

An I/Q detector, depicted in Fig. 2.3 is used to eliminate the in-phase **I** and the quadrature **Q** components using a low-pass filter which discards the high frequency terms. A third form of a narrow bandpass signal is

$$s(t) = Re\{u(t)\exp(jw_c t)\} \tag{2.19}$$

where u(t) is called the complex envelope of the signal s(t) and is defined as

$$u(t) = g_c(t) + jg_s(t) \quad . \tag{2.20}$$

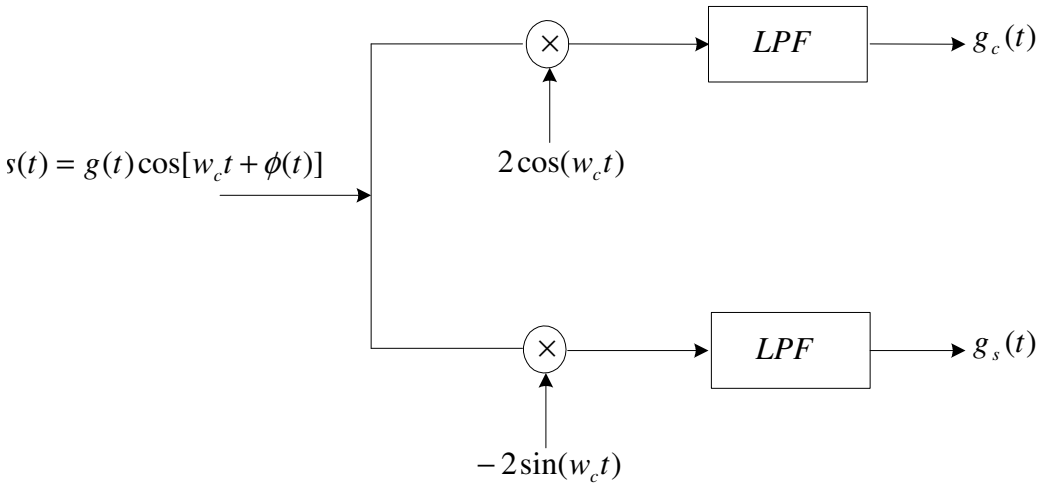

Figure 2.3: IQ Detector.

The angular frequency w_c is called as the carrier frequency and it is significantly larger than the bandwidth of the baseband signal. The fourth and the most general form of a narrow bandpass signal is

$$s(t) = \frac{1}{2}u(t)\exp(jw_c t) + \frac{1}{2}u^*(t)\exp(-jw_c t) \quad . \tag{2.21}$$

Now we can get into the motivation and derivation of the matched filter and the ambiguity function.

Matched filters can be designed for both baseband and bandpass real signals. In the following derivations, a filter matched to the complex envelope of the signal will be considered. In Fig. 2.4, the input signal to the filter is the s(t) in additive white gaussian noise with a two-sided power spectral density of $N_0/2$ [22]. Impulse response of the filter is h(t) and the frequency response is H(w). The objective here is to find a h(t), which yields the maximum output SNR at a specific t_0 when we decide on the presence or absence of $s(t)$ in white noise. The mathematics of this objective is maximizing

$$\left(\frac{S}{N}\right)_{out} = \frac{|s_o(t_0)|^2}{\overline{n_o^2(t)}} \quad . \tag{2.22}$$

Assuming S(w) is the Fourier transform of the s(t), one can write the output of the matched filter at t_0 as

$$s_o(t_0) = \frac{1}{2\pi}\int_{-\infty}^{\infty} H(w)S(w)\exp(jwt_0)dw \tag{2.23}$$

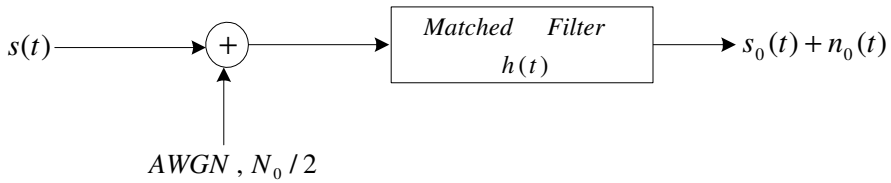

Figure 2.4: Matched filter block diagram.

The mean-squared value of the noise is

$$\overline{n_o^2(t)} = \frac{N_0}{4\pi}\int_{-\infty}^{\infty}|H(w)|^2 dw \tag{2.24}$$

If we substitute (2.23) and (2.24) into (2.22) output SNR becomes

$$\left(\frac{S}{N}\right)_{out} = \frac{\left|\int_{-\infty}^{\infty} H(w)S(w)\exp(jwt_0)dw\right|^2}{\pi N_0\int_{-\infty}^{\infty}|H(w)|^2 dw} \quad . \tag{2.25}$$

Using the *Schwarz inequality*, (2.41) can be rewritten as

$$\left(\frac{S}{N}\right)_{out} \leq \frac{1}{\pi N_0}\int_{-\infty}^{\infty}|S(w)|^2 dw = \frac{2E}{N_0} \tag{2.26}$$

where E is the energy of the signal:

$$E = \int_{-\infty}^{\infty} s^2(t)dt = \frac{1}{2\pi}\int_{-\infty}^{\infty}|S(w)|^2 dw \tag{2.27}$$

The equality in the above, *Schwarz* upper bound can be achieved by the following filter response which is the matched filter:

$$H(w) = KS^*(w)\exp(-jwt_0) \quad . \tag{2.28}$$

Taking the inverse fourier transform, impulse response of the filter reveals as

$$h(t) = Ks^*(t_0 - t) \quad , \tag{2.29}$$

meaning that delayed mirror image of the conjugate of the signal is impulse response of the matched filter. Using this configuration, at $t = t_0$, one can obtain a maximum output SNR value of $2E/N_0$. This result is interesting in the sense that, maximum SNR at the output of a matched filter is only a function of the signal energy but not its shape.

Let's now investigate a filter matched to a narrowband bandpass signal. If we use the forth form of s(t), given in (2.21), in (2.23) we get the equation below:

$$s_o(t) = \frac{K}{4}\int_{-\infty}^{\infty} \big[u(\tau)\exp(jw_c\tau) + u^*(\tau)\exp(-jw_c\tau)\big] \\ .\big\{u^*(\tau - t + t_0)\exp[-jw_c(\tau - t + t_0)] \\ +u(\tau - t + t_0)\exp[jw_c(\tau - t + t_0)]\big\}d\tau \qquad (2.30)$$

After straightforward simplifications, $s_o(t)$ can be obtained as:

$$s_o = Re\left(\left[\frac{1}{2}K\exp(-jw_ct_0)\int_{-\infty}^{\infty} u(\tau)u^*(\tau - t + t_0)d\tau\right]\exp(jw_ct)\right) \quad . \qquad (2.31)$$

From this long equation, we can separate out a new complex envelope:

$$u_o(t) = \frac{1}{2}K\exp(-jw_ct_0)\int_{-\infty}^{\infty} u(\tau)u^*(\tau - t + t_0)d\tau \quad , \qquad (2.32)$$

and in the end we obtain the output of the matched filter as

$$s_o(t) = Re\big\{u_o(t)\exp(jw_ct)\big\} \quad . \qquad (2.33)$$

This equation tells us that the output of a filter matched to a narrowband bandpass signal has a complex envelope $u_o(t)$ obtained by passing the complex envelope $u(t)$ of the narrowband bandpass signal through its own matched filter. Therefore, in applications where narrowband bandpass signals used, it is sufficient to work with the complex envelope $u(t)$ of the signal and its matched filter output $u_o(t)$. Once $u_o(t)$ is obtained, $s_o(t)$ could be found by (2.33).

The above derivation of the matched filter ignored the potential Doppler shift on the received signals. However in wireless communication, when the receiver is moving relative to the transmitter or the received waves bounced off from moving objects, the received signal suffers a Doppler shift. When the Doppler shift is not known, performance of the receiver that makes use of a matched filter matched to the transmitted signal may significantly degrade. Now let's modify the input complex envelope with a Doppler shift as below:

$$u_d(t) = u(t)\exp(j2\pi\nu t) \quad . \qquad (2.34)$$

In order to find the output complex envelope we replace the first $u(t)$ in (2.32) by $u_d(t)$ and choose $t_0 = 0, K = 1$ yields a function carrying both doppler shift and time information:

$$u_o(t,\nu) = \int_{-\infty}^{\infty} u(\tau)\exp(j2\pi\nu\tau)u^*(\tau - t)d\tau \quad . \tag{2.35}$$

Another form of (2.35) is the well-known *ambiguity function* and given as

$$\chi_{u,u}(\tau,\nu) = \int_{-\infty}^{\infty} u(t)u^*(t-\tau)\exp(j2\pi\nu t)dt \quad . \tag{2.36}$$

The ambiguity function (AF), characterizes the output of a matched filter when the input signal is delayed by τ and Doppler shifted by ν. This function was first introduced by Woodward in 1953 and found useful in wide variety of applications.

Let's now mention some of the important properties of AF. If we assume that the energy E of $u(t)$ is normalized to unity, maximum value of the ambiguity function occurs at the origin and equals to one. We can formalize it as

$$\left|\chi(\tau,\nu)\right| \leq \left|\chi(0,0)\right| = 1 \quad . \tag{2.37}$$

Total volume under the normalized ambiguity surface equals unity, independent of the signal waveform:

$$\int_{-\infty}^{\infty}\int_{-\infty}^{\infty} \left|\chi(\tau,\nu)\right|^2 d\tau d\nu = 1 \quad . \tag{2.38}$$

These two properties states that, if one try to squeeze the AF to a narrow peak at the origin, that peak cannot exceed a value of one and the volume squeezed out of that peak must reappear somewhere else [23]. Therefore, the behavior of the ambiguity diagram indicates that there have to be trade-offs made among the resolution, accuracy, and ambiguity. Thirdly, AF is symmetric with respect to the origin;

$$\left|\chi(-\tau,-\nu)\right| = \left|\chi(\tau,\nu)\right| \tag{2.39}$$

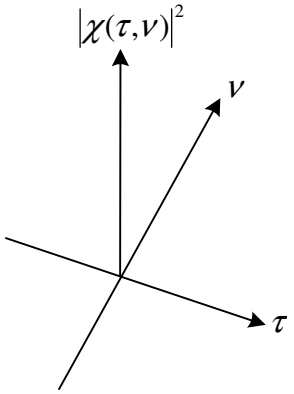

Figure 2.5: Ideal ambiguity function; $\left|\chi(\tau,\nu)\right|^2 = \delta(\tau,\nu)$.

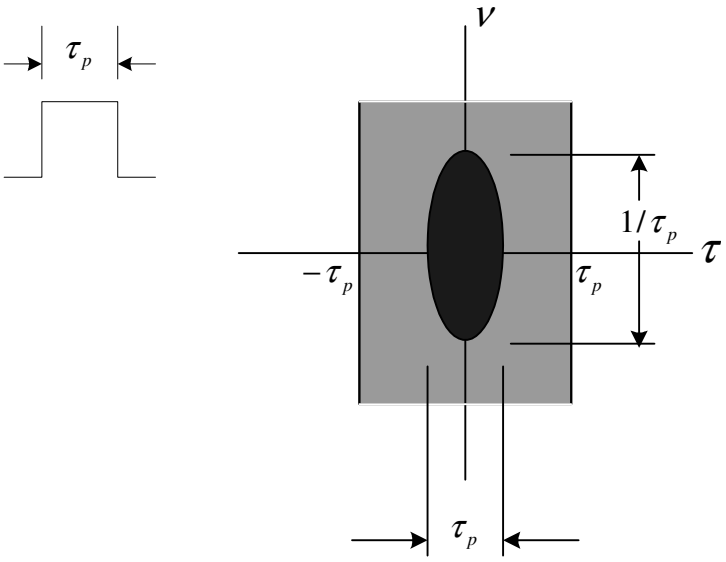

Figure 2.6: 2D view of the ambiguity function for a single pulse of width τ_p.

which suggests that it is sufficient to study only two adjacent quadrant of the AF.

Although it is not realistic, the "ideal" ambiguity diagram would consists of a single infinitesimal thickness peak at the origin and be zero everywhere else, as shown in Fig. 2.5. This figure tells us that we have no ambiguities in range or doppler frequency. Time delay and/or frequency could be determined simultaneously to as high a degree of accuracy as wanted.

Usually two dimensional plots of ambiguity diagrams are used to gather information. In Fig. 2.6, two dimensional representation of the ambiguity diagram

for a single unmodulated pulse obtained by gating a sinusoid signal of width τ_p is given. Black shaded regions indicate that $\left|\chi(\tau,\nu)\right|^2$ is large and gray regions indicate that $\left|\chi(\tau,\nu)\right|^2$ is small. This figure says that if τ_p is large corresponding to a long pulse, we have poor delay and good doppler accuracy. The opposite occurs for a short pulse. The short pulse is doppler tolerant, meaning that the output from a filter matched to a zero doppler shift will not change much when there is a doppler shift. However, the long pulse is not doppler tolerant, and produce reduced output for a doppler-frequency shift. Lastly for this unmodulated pulse, the time bandwidth product (TBP) which is defined as the 3-dB timewidth times the 3-dB bandwidth of the pulse is one. For modulated pulses the TBP may significantly exceed one.

Each different waveform yields a new distribution of ambiguity. There are several types of signals that are commonly used in practice. Two important examples are the periodic continuous wave (CW) radar signal and a coherent train of identical pulses. In Fig. 2.7, ambiguity distribution of a uniform pulse train is shown. If there are N pulses of duration τ_p in a pulse train where pulses are separated by T/N, the Doppler measurement accuracy becomes $1/T$ which can be many time more accurate than the accuracy provided by a single pulse. This fact is illustrated in Fig. 2.7. To increase the delay accuracy, transmitted pulses can be modulated either by using phase or frequency modulations. For example, if the pulse of duration τ_p is divided into 13 subpulses where the phase of each subpulse is chosen to be $\{11111-1-111-11-11\}$, which is known as the Barker-13 sequence, the delay accuracy can be increased by 13 times. Note that, the Ambiguity distribution of a Barker-13 sequence is plotted in Fig. 2.8. The TBP of this sequence is thirteen.

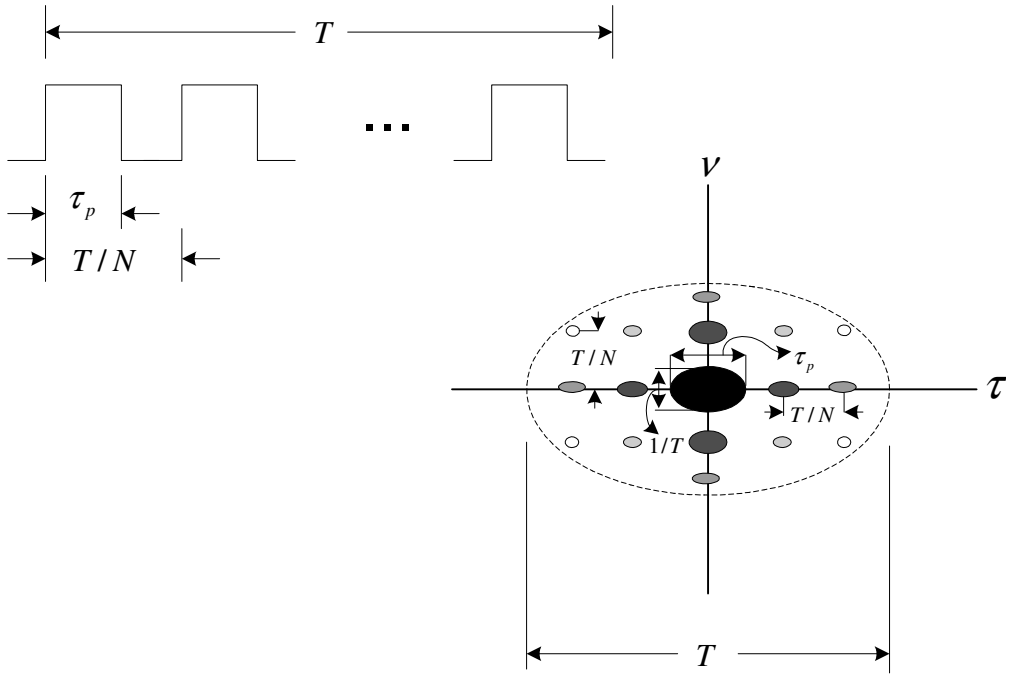

Figure 2.7: Ambiguity function distribution of an uniform pulse train.

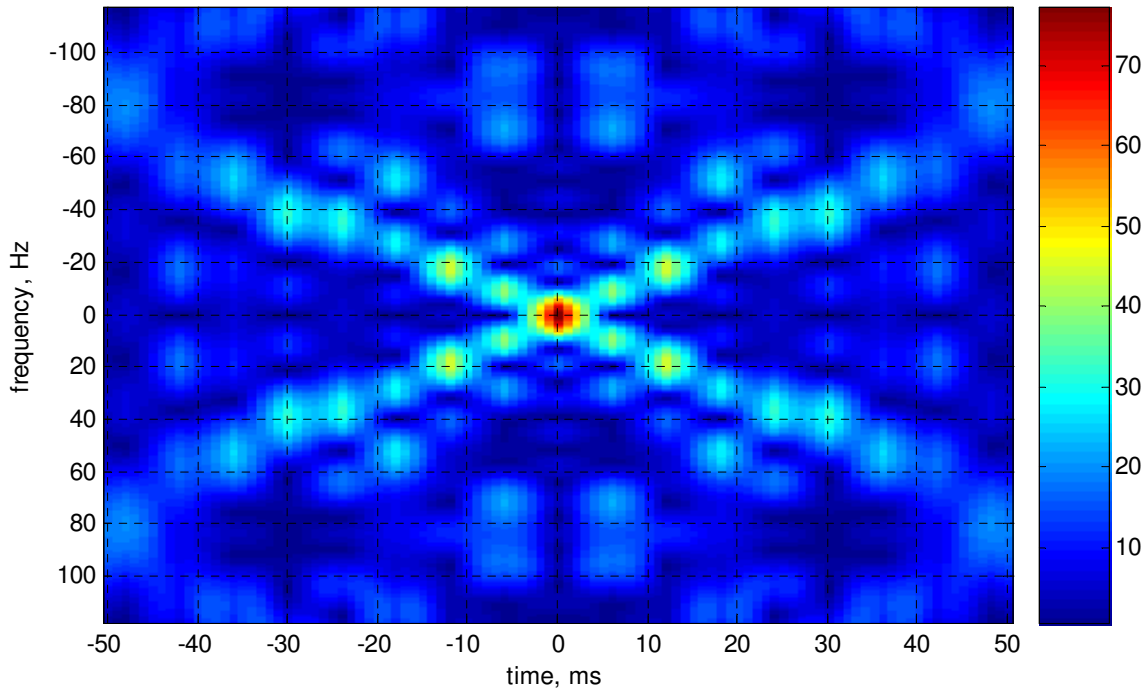

Figure 2.8: Ambiguity function distribution of a Barker-13 sequence.

2.3 Applications of Array Processing

The practical and theoretical improvements of parameter estimation in array signal processing has resulted in a many types of applications. In this section, only the three important areas, namely radar-sonar, communications and industrial applications will be discussed.

The very first application of array signal processing is in radar. Phased arrays are the most advanced type of antenna used in modern radars. Its a kind of array whose beam direction is controlled by the relative phases of the excitation coefficients of the relative elements [24]. Some important issues which provide radar with great flexibility can be given as: high directivity and power gain; capability of combining search and track functions when operating in multiple-target and severe interference environments; ability to change beam position in space almost instantaneously; generating very high powers from many sources distributed across the aperture; better throughput; and compatibility with digital signal processing algorithms and digital computers. Furthermore, in sonar applications the signal energy is usually acoustic and measured using arrays of hydrophones. The receiving antenna usually towed under water and has the capability of detecting and locating distant sources.

Antenna arrays are extremely important in personal communications. One of the most crucial problems in a multiuser environment is the inter-user interference. This type of problems degrade the performance severely which is also the case in Code Division Multiple Access (CDMA) systems. CDMA is a form of multiplexing and a method of multiple access that does not divide up the channel by time (as in TDMA), or frequency (as in FDMA), but encodes data with a special code associated with each channel and uses the constructive interference properties of the special codes to perform the multiplexing [25]. CDMA exploits at its core mathematical properties of orthogonality. In real life applications,

varying delays of different users induce non-orthogonal codes. An implementation of multiple signal classification algorithm (MUSIC), which will be discussed in Chapter 3, is presented in [26] for estimating these propagation delays. Spatial diversity had been used for a long time in order to handle the fading problem due to multipath. Nevertheless, array antennas have several additional advantages such as obtaining higher selectivity. For instance, a receiving array can be steered in the direction of one user at a time, while simultaneously nulling interference from other users. In [27], a similar version of the beamspace array processing describes how to localize incoming users waveforms.

In many areas of industry, array signal processing plays a central role. Medical applications are the most important commercial application areas of the sensor arrays. Circular arrays are widely used as a means to focus energy, in medical imaging and hyperthermia treatment [28]. Planar arrays are found important applications in electrocardiograms. They used to track the changes of wavefronts which in turn provide information about the situation of patient's heart. In tomography, array signal processing used to characterize shapes of the objects [29]. Moreover, biomagnetic sensor arrays, so called super-conducting quantum interference device (SQUID) magnetometers localize brain activity [30]. Other application areas in industry may be given as; fault detection/localization and automatic monitoring. For instance, sensors are placed to detect and localize faults such as broken gears [31].

Chapter 3

DIRECTION-OF-ARRIVAL (DOA) ESTIMATIONS

The interest in array signal processing originates from a wide range of applications such as radar, radio and microwave communications where waveforms are measured at several poins in space and/or time. Many estimation techniques for estimating unknown signal parameters from the measured output of a antenna array have been proposed.

Much of the current work in array signal processing has focused on methods for high-resolution DOA estimation. In this chapter, well known parameter estimation techniques will be discussed in two main categories, namely *spectral-based* and *parametric* approaches [32]. In spectral-based approaches, we form a function of the parameter(s) of interest, e.g., the DOAs. The locations of the highest peaks of the function are considered as the DOAs estimates. Differently, in parametric techniques, we search for all parameters of interests simultaneously. In this latercase, one gets more accurate estimates however, the computational complexity also increases.

3.1 Spectral-Based Algorithmic Solutions

In the following, we will investigate the spectral-based approaches in two categories: beamforming techniques and subspace-based methods.

3.1.1 Beamforming Techniques

Beamforming is a signal processing technique used with antenna arrays that controls the directionality and localize signal sources. The basic idea behind the technique is to concentrate the array to waves coming from only one particular direction. The steering directions which result in maximum signal power yields the DOA estimates. The array response can be obtained by multiplying the each sensor output with an appropriate weighting factor and forming a linear combination:

$$y(t) = \sum_{m=1}^{M} w_m^* x_m(t) = \mathbf{w}^H \mathbf{x}^t \quad . \tag{3.1}$$

If we digitize (3.1), the output power is measured by

$$\begin{aligned} P(\mathbf{w}) &= \frac{1}{N} \sum_{n=1}^{N} |y(n)|^2 \\ &= \frac{1}{N} \sum_{n=1}^{N} \mathbf{w}^H \mathbf{x}(n) \mathbf{x}^H(n) \mathbf{w} \\ &= \mathbf{w}^H \hat{\mathbf{R}} \mathbf{w} \end{aligned} \tag{3.2}$$

where, in sample-wise notation,

$$\begin{aligned} \hat{\mathbf{R}} &= \frac{1}{N} \sum_{n=1}^{N} \mathbf{x}(n) \mathbf{x}^H(n) \\ \hat{\mathbf{R}} &= \hat{\mathbf{U}}_s \hat{\mathbf{\Lambda}}_s \hat{\mathbf{U}}_s^H + \hat{\mathbf{U}}_n \hat{\mathbf{\Lambda}}_n \hat{\mathbf{U}}_n^H \quad . \end{aligned} \tag{3.3}$$

In this thesis, two basic beamforming approaches will be investigated.

The conventional beamforming technique is the simplest one which relays on the Fourier-based spectral analysis to antenna array output [3]. The purpose is to

maximize the output power of the beamformer from a certain signal propagation direction. If the desired direction is (θ, ϕ), then we can write the array output as

$$\mathbf{x}(t) = \mathbf{a}(\theta, \phi)s(t) + \mathbf{n}(t) \quad . \tag{3.4}$$

If we assume that the noise is spatially white, the maximum output power can be found as;

$$\begin{aligned} &\max_{\mathrm{w}} \mathrm{E}\{\mathbf{w}^{\mathrm{H}}\mathbf{x}(\mathrm{t})\mathbf{x}^{\mathrm{H}}(\mathrm{t})\mathbf{w}\} \\ &= \max_{\mathrm{w}} \mathbf{w}^{\mathrm{H}}\mathrm{E}\{\mathbf{x}(\mathrm{t})\mathbf{x}^{\mathrm{H}}(\mathrm{t})\}\mathbf{w} \\ &= \max_{\mathrm{w}} \{\mathrm{E}|\mathrm{s}(\mathrm{t})|^2|\mathbf{w}^{\mathrm{H}}\mathbf{a}(\theta, \phi)|^2 + \sigma^2|\mathbf{w}|^2\} \quad . \end{aligned} \tag{3.5}$$

Also let $|\mathbf{w}| = 1$, the maximum power can be obtained for the following choice for the w:

$$\mathbf{w} = \frac{\mathbf{a}(\theta, \phi)}{\sqrt{\mathbf{a}^H(\theta, \phi)\mathbf{a}(\theta, \phi)}} \quad . \tag{3.6}$$

This vector matches to the direction of impinging signal and can be thought of as a filter. If we substitute (3.6) into (3.2), the spatial spectrum is obtained as

$$P(\theta, \phi) = \frac{\mathbf{a}^H(\theta, \phi)\hat{\mathbf{R}}\mathbf{a}(\theta, \phi)}{\mathbf{a}^H(\theta, \phi)\mathbf{a}(\theta, \phi)} \tag{3.7}$$

Conventional beamformers shows poor performance when resolving power of two sources spaced closer than a beamwidth. However, a well-known method called Capon's beamforming proposed in [33], resolves this limitation. The cost function of the approach is introduced as

$$\begin{aligned} &\min_{\mathrm{w}} \ \mathrm{P}(\mathbf{w}) \\ &\text{subject to } \ \mathbf{w}^{\mathrm{H}}\mathbf{a}(\theta, \phi) = 1 \quad , \end{aligned} \tag{3.8}$$

which tries to minimize the power contributed by impinging signals coming from other directions than the look direction (θ, ϕ) and noise. One solution of (3.8) is

$$\mathbf{w} = \frac{\hat{\mathbf{R}}^{-1}\mathbf{a}(\theta, \phi)}{\mathbf{a}^H(\theta, \phi)\hat{\mathbf{R}}^{-1}\mathbf{a}(\theta, \phi)} \quad , \tag{3.9}$$

and the spatial spectrum is obtained by inserting the (3.9) into (3.2) as

$$P(\theta,\phi) = \frac{1}{\mathbf{a}^H(\theta,\phi)\hat{\mathbf{R}}^{-1}\mathbf{a}(\theta,\phi)} \quad . \tag{3.10}$$

This spatial spectrum and the constraint given in (3.8) gives the Capon's beamformer the ability of better focusing in the directions where there are multiple sources.

3.1.2 Subspace-Based Methods

Spectral decomposition of a covariance matrix is the starting point of the many spectral methods in DOA analysis. Subspace-based approaches become very popular with the usage of the eigen-structure of the covariance matrix. The interest was mainly due to the introduction of the MUSIC(Multiple SIgnal Classification) algorithm [4, 5].

As stated in the early sections, the spectral decomposition of a covariance matrix can be expressed as

$$\begin{aligned} \mathbf{R} &= \mathbf{A}\mathbf{P}\mathbf{A}^H + \sigma^2\mathbf{I} \\ &= \mathbf{U}_s\mathbf{\Lambda}_s\mathbf{U}_s^H + \sigma^2\mathbf{U}_n\mathbf{U}_n^H \end{aligned} \tag{3.11}$$

where the diagonal matrix $\mathbf{\Lambda}_s$ holds the d largest eigenvalues, assuming $\mathbf{A}\mathbf{P}\mathbf{A}^H$ to be of full rank. Spatial directions of d signal sources are the solutions of the equation;

$$\mathbf{U}_n^H\mathbf{a}(\theta_i,\phi_i) = 0 \tag{3.12}$$

where $\mathbf{U}_n$ contains the noise eigenvectors.

Eigenvectors of the covariance matrix estimate, $\hat{\mathbf{R}}$, are separated into the signal and noise eigenvectors as in Eq.(3.3). Secondly, the orthogonal projector onto the noise subspace is found as

$$\hat{\Pi}^{\perp} = \hat{\mathbf{U}}_n\hat{\mathbf{U}}_n^H \quad . \tag{3.13}$$

Then the spatial spectrum of the MUSIC algorithm is defined as

$$P(\theta,\phi) = \frac{\mathbf{a}^H(\theta,\phi)\mathbf{a}(\theta,\phi)}{\mathbf{a}^H(\theta,\phi)\hat{\Pi}^{\perp}\mathbf{a}(\theta,\phi)} \quad . \tag{3.14}$$

Performance of the MUSIC algorithm is significantly better than the beamforming techniques and provides statistically consistent estimates. However, at low SNR and closely spaced signals scenarios , MUSIC fails to resolve DOAs. This resolution loss is more revealed for highly correlated signals. In the case of coherent signals, Eqn.(3.12) becomes false and the algorithm fails to yield consistent estimates.

The idea behind the MUSIC algorithm is applied to many application areas and led to a multiple of variants. One of the most successful variant is the *weighted MUSIC*, which has a spatial spectrum as

$$P(\theta,\phi) = \frac{\mathbf{a}^H(\theta,\phi)\mathbf{a}(\theta,\phi)}{\mathbf{a}^H(\theta,\phi)\hat{\Pi}^{\perp}\mathbf{W}\hat{\Pi}^{\perp}\mathbf{a}(\theta,\phi)} \quad . \tag{3.15}$$

The effects of the eigenvectors are taken into account through the weighting matrix $\mathbf{W}$. Although uniform weighting usage yields estimates with minimal variance, in some scenarios involving correlated signals, low SNR and short duration signals, a non-uniform weighting improve the resolution of the algorithm considerably with an acceptable increase in the variance [34].

3.2 Parametric Methods

Spectral-based methods discussed in the previous section are very effiecient in terms of computational power. However, they do not provide enough accuracy for different cases. For instance, in correlated signal scenarios, performance of the spectral-based algorithms degrades significantly. Parametric methods fill the gap in coherent signal DOA estimations. These methods provide better accuracy and robustness but at the same time require a multidimensional search to

produce estimates. In this section, deterministic maximum likelihood, stochastic likelihood and subspace-based approximations will be discussed respectively.

3.2.1 Deterministic Maximum Likelihood

In our data model, we assume that the signal carrying the data is emitted from d sources whereas background and receiver noise can be thought of as emanating from a large number of independent sources. As a result, data signals are deterministic and noise is assumed to be a stationary Gaussian white random process [32].

In the case of spatially white and circularly symmetric noise, statistical properties can be written as

$$E\{\mathbf{n}(t)\mathbf{n}^H(t)\} = \sigma^2\mathbf{I} \tag{3.16}$$

$$E\{\mathbf{n}(t)\mathbf{n}^T(t)\} = \mathbf{0} \quad . \tag{3.17}$$

By means of the assumptions above, array output $\mathbf{x}$(t) can be modeled as circularly symmetric and temporally white Gaussian random process having a mean $\mathbf{A}(\theta,\phi)\mathbf{s}(t)$ and covariance $\sigma^2\mathbf{I}$. The probability density function (PDF) of $\mathbf{x}$(t) is the complex L-variate Gaussian:

$$\frac{1}{(\pi\sigma^2)^{L/2}}\, e^{-\|\mathbf{x}(t)-\mathbf{A}\mathbf{s}(t)\|^2/2\sigma^2} \quad , \tag{3.18}$$

where $\|.\|$ denotes the Euclidean norm. Measurements are independent so likelihood function is given as

$$L(\theta,\phi,s(t),\sigma^2) = \prod_{t=1}^{N} \frac{1}{(\pi\sigma^2)^{L/2}}\, e^{-\|\mathbf{x}(t)-\mathbf{A}\mathbf{s}(t)\|^2/2\sigma^2} \quad . \tag{3.19}$$

Direction of arrivals (θ,ϕ), signal waveforms $\mathbf{s}$(t), and the noise variance σ^2 are the parameters that should be estimated. Calculated ML estimates of these unknown parameters maximize $L(\theta,\phi,s(t),\sigma^2)$. In the maximization, the log

likelihood function:

$$l(\theta, \phi, s(t), \sigma^2) = L \log \sigma^2 + \frac{1}{\sigma^2 N} \sum_{t=1}^{N} \|\mathbf{x}(t) - \mathbf{A}\mathbf{s}(t)\|^2 \tag{3.20}$$

is commonly used. The minimizing arguments of the log likelihood function are called as the deterministic maximum likelihood (DML) estimates. Note that the DML estimates for σ^2 and $s(t)$ are:

$$\hat{\sigma}^2 = \frac{1}{L} tr\big\{(\mathbf{I} - \mathbf{A}\mathbf{A}^\dagger)\hat{\mathbf{R}}\big\} \tag{3.21}$$

$$\hat{\mathbf{s}}(t) = \mathbf{A}^\dagger \mathbf{x}(t) \tag{3.22}$$

where $\mathbf{A}^\dagger$ is the pseudo inverse of $\mathbf{A}$ and $\hat{\mathbf{R}}$ is the sample covariance matrix [35, 7].

If we substitute (3.21) and (3.22) into (3.19), the DML estimates for θ and ϕ can be expressed as:

$$\hat{\theta}, \hat{\phi} = \arg\big\{\min_{\theta} \operatorname{tr}\big\{(\mathbf{I} - \mathbf{A}\mathbf{A}^\dagger)\hat{\mathbf{R}}\big\}\big\} \tag{3.23}$$

In order to obtain $\hat{\theta}$ and $\hat{\phi}$, one should solve the non-linear d-dimensional optimization problem. Good initial estimates lead to very accurate DOA estimates. However, as stated before computational complexity is very high.

3.2.2 Stochastic Maximum Likelihood

Stochastic maximum likelihood (SML) method is derived by modeling the signal waveforms as Gaussian random processes. By [8, 9], the accuracy of the parameter estimates are related with correlations and power of the waveforms. Assume that, some properties of the signal is given as

$$E\big\{\mathbf{s}(t)\mathbf{s}^H(t)\big\} = \mathbf{P} \tag{3.24}$$

$$E\big\{\mathbf{s}(t)\mathbf{s}^T(t)\big\} = 0 \quad , \tag{3.25}$$

saying that $\mathbf{x}$(t) is a white, zero-mean and circularly symmetric gaussian random vector having a covariance matrix

$$\mathbf{R} = \mathbf{A}(\theta, \phi)\mathbf{P}\mathbf{A}^{H}(\theta, \phi) + \sigma^2\mathbf{I} \quad . \tag{3.26}$$

where the unknown parameters are (θ, ϕ), $\mathbf{P}$ *and* σ^2.

The likelihood function of the SML is proportional to

$$\frac{1}{N}\sum_{t=1}^{N} \|\Pi_A^{\perp}\mathbf{x}(t)\|^2 = tr\big\{\Pi_A^{\perp}\hat{\mathbf{R}}\big\} \tag{3.27}$$

and for fixed θ, ϕ, the minimum with respect to σ^2 and $\mathbf{P}$ can be given as [10]

$$\sigma^2(\theta, \phi) = \frac{1}{M-d} tr\{\Pi_A^{\perp}\} \tag{3.28}$$

$$\hat{\mathbf{P}}(\theta, \phi) = \mathbf{A}^{\dagger}\big(\hat{\mathbf{R}} - \hat{\sigma}^2(\theta, \phi)\mathbf{I}\big)\mathbf{A}^{\dagger H} \quad . \tag{3.29}$$

If we substitute (3.28) and (3.29) into (3.27), we get the following expression for the SML estimates of θ and ϕ:

$$\hat{\theta}, \hat{\phi} = \arg\big\{\min_{\theta} \log\big|\mathbf{A}\hat{\mathbf{P}}(\theta, \phi)\mathbf{A}^{\mathrm{H}} + \hat{\sigma}^2(\theta, \phi)\mathbf{I}\big|\big\} \quad . \tag{3.30}$$

SML parameter estimates are better than the DML estimates in low SNR and highly correlated signal situations. Moreover, this method provides robust results even if the distribution of the signal waveform is not Gaussian.

3.2.3 Subspace-Based Approximations

We already mentioned that, conventional beamforming techniques are significantly behind the subspace-based methods as far as the performance and the accuracy are our concern. Moreover, in uncorrelated signal scenarios, MUSIC performs identical to DML in accuracy [34]. However, resolution problems occur for finite samples and high source correlation scenarios in spectral-based methods. In this section, some well-known *Subspace Fitting* methods, which offer

the same statistical performance and are computationally very efficient, will be discussed.

Let's restate the eigendecomposition of the array covariance matrix (3.11),

$$\mathbf{R} = \mathbf{A}\mathbf{P}\mathbf{A}^H + \sigma^2\mathbf{I} \tag{3.31}$$

$$= \mathbf{U}_s\mathbf{\Lambda}_s\mathbf{U}_s^H + \sigma^2\mathbf{U}_n\mathbf{U}_n^H \quad . \tag{3.32}$$

We know that if $\mathbf{P}$ is a full rank matrix, then $\mathbf{A}$ and $\mathbf{U}_s$ span the same range space. However, in general, the rank of $\mathbf{P}$ is $\tilde{d}$ which is the number of eigenvectors in $\mathbf{U}_s$. Then $\mathbf{U}_s$ will span a $\tilde{d}$-dimensional subspace of $\mathbf{A}$. Since,

$$\mathbf{I} = \mathbf{U}_s\mathbf{U}_s^H + \mathbf{U}_n\mathbf{U}_n^H \tag{3.33}$$

we have the following equality

$$\mathbf{A}\mathbf{P}\mathbf{A}^H + \sigma^2\mathbf{U}_s\mathbf{U}_s^H = \mathbf{U}_s\mathbf{\Lambda}_s\mathbf{U}_s^H \quad . \tag{3.34}$$

After some simple manipulations on the equation above we obtain:

$$\mathbf{U}_s = \mathbf{A}\mathbf{T} \tag{3.35}$$

where $\mathbf{T}$ is the full rank ($\tilde{d}$) matrix given by

$$\mathbf{T} = \mathbf{P}\mathbf{A}^H\mathbf{U}_s\big(\mathbf{\Lambda}_s - \sigma^2\mathbf{I}\big)^{-1} \quad . \tag{3.36}$$

Equation (3.35) is the basic starting point of the *Signal Subspace Fitting (SSF)* approach [12, 6]. In order to solve the (3.35) one needs a search for the unknown parameters (θ, ϕ) and $\mathbf{T}$. Obviously, resulting (θ, ϕ) are the DOAs. If instead of $\mathbf{U}_s$, an estimate $\hat{\mathbf{U}}_s$ is used then the distance between the $\hat{\mathbf{U}}_s$ and $\mathbf{A}\mathbf{T}$ should be minimized. The SSF estimates are found by solving the following optimization problem:

$$\big\{\hat{\theta}, \hat{\phi}, \hat{\mathbf{T}}\big\} = \arg\min_{\theta,\phi,\mathbf{T}} \big\|\hat{\mathbf{U}}_\mathrm{s} - \mathbf{A}\mathbf{T}\big\|_\mathrm{F}^2 \quad . \tag{3.37}$$

For fixed but unknown $\mathbf{A}$, the estimate of $\mathbf{T}$ is

$$\hat{\mathbf{T}} = \mathbf{A}^\dagger\hat{\mathbf{U}}_s \quad , \tag{3.38}$$

and using this result, the required optimization can be expressed as:

$$\hat{\theta,\phi} = \arg\left\{\min_{\theta,\phi}\left\{\Pi_{\mathrm{A}}^{\perp}\hat{\mathbf{U}}_{\mathrm{s}}\hat{\mathbf{\Lambda}}\hat{\mathbf{U}}_{\mathrm{s}}^{\mathrm{H}}\right\}\right\} \tag{3.39}$$

Another form of a subspace fitting approach is obtained by using the following equation;

$$\mathbf{A}^{H}(\theta,\phi)\mathbf{U}_n = 0 \quad , \tag{3.40}$$

which holds for $\mathbf{P}$ having full rank. After an estimate of $\mathbf{U}_n$ is found, signal parameters can be determined by minimizing the following equation;

$$\hat{\theta},\hat{\phi} = \arg\left\{\min_{\theta,\phi}\mathrm{tr}\left\{\mathbf{A}^{\mathrm{H}}\hat{\mathbf{U}}_{\mathrm{n}}\hat{\mathbf{U}}_{\mathrm{n}}^{\mathrm{H}}\mathbf{A}\mathbf{V}\right\}\right\} \quad , \tag{3.41}$$

which is known as *noise subspace fitting (NSF)* criterion [6, 13]. In this equation $\mathbf{V}$ is a positive definite weighting matrix. For $\mathbf{V} = \mathbf{I}$ and in the case of $|a(\theta,\phi)|$ is independent of (θ,ϕ), this method reduces the MUSIC algorithm. The criterion function is a quadratic function of the steering matrix $\mathbf{A}$. If any of the parameters of $\mathbf{A}$ enter linearly then it is very easy to obtain an analytical solution with respect to these variables [36]. However, NSF fails to produce reliable estimates in coherent signal situations [11, 32].

Chapter 4

HF COMMUNICATION

Modern radio technology actually starts with the publication of James Clerk Maxwell's Treatise on Electricity and Magnetism in 1873, introducing the basic theory of electromagnetic wave propagation. However, the first radio waves were actually detected 15 years later. In 1888, Heinrich Rudolph Hertz showed that disturbances generated by a spark coil showed the characteristics of Maxwell's radio waves. His work impressed Guglielmo Marconi's early experiments with wireless telegraphy using Morse code. By 1896, Marconi had communicated messages over distances of a few kilometers.

In those years, it was thought that radio waves in the atmosphere traveled in straight lines and that they therefore would not be useful for over-the-horizon communication. However, Marconi achieved radio communication over long distances. In 1901 in Newfoundland, Canada, he detected a telegraphic signal transmitted from Cornwall, England,3000 kilometers away using a 120 meters long wire.

Marconi's achievement activated a huge effort on this issue. Eventually Edward Appleton answered the question of how radio waves could be received around the surface of the earth. He discovered that a blanket of electrically

charged, or "ionized", particles in the earth's atmosphere, the "ionosphere", were capable of reflecting radio waves. By the 1920s, researchers had used this theory and developed ways to predict the refractive properties of the ionosphere. Today, with the experience and understanding of the propagating effects of the ionosphere, HF technology provides reliable and effective communication over many thousands of miles. In this chapter, structure and some important properties of this natural satellite will be discussed.

4.1 Structure of the Ionosphere

The ionosphere is composed of a number of ionised regions above the earth's atmosphere, which extends from a height of about 60 km to 600 km. These regions are believed to influence the radio waves mainly because of the presence of free electrons, which are arranged in approximately horizontally stratified layers [37].

The ionisation in the ionosphere is caused mainly by radiation from the sun. This is a process by which electrons, having a negative charge, are stripped from the neutral atoms or molecules to form positively charged ions. It is these ions that give their name to the ionosphere. These electrons under the influence of an electromagnetic wave will absorb and reradiate energy, and modify direction of an electromagnetic wave.

Most of the ionisation in the ionosphere results from ultraviolet light, although this does not mean that other wavelengths do not have some effect. Additionally, each time an atom or molecule is ionised, a small amount of energy is used. This means that as the radiation passes further into the atmosphere, its intensity reduces. It is for this reason that the ultraviolet radiation causes most of the ionisation in the upper reaches of the ionosphere, but at lower altitudes the radiation that is able to penetrate further cause more of the ionisation. Accordingly,

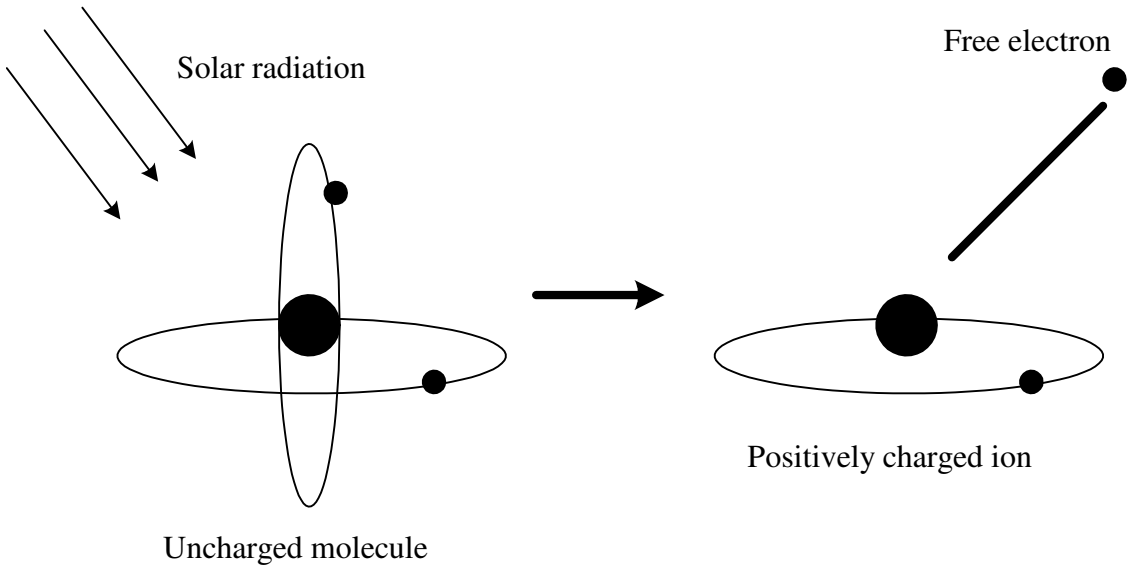

Figure 4.1: Electron production due to solar radiation.

extreme ultra-violet and X-Rays give rise to most of the ionisation at lower altitudes. In addition to this, there is a variation in the proportions of monatomic and molecular forms of the gases, the monatomic forms of gases being far greater at higher altitudes. These and a variety of other phenomena mean that there are variations in the level of ionisation with altitude.

The level of ionisation in the ionosphere also changes with time. It varies with the time of day, time of year, and according to many other external influences. One of the main reasons why the electron density varies is that the sun, which gives rise to the ionisation. While the radiation from the sun causes the atoms and molecules to split into free electrons and positive ions. The reverse effect also occurs. When a negative electron meets a positive ion, the fact that dissimilar charges attract means that they will be pulled towards one another and they may combine. This means that two opposite effects of splitting and recombination are taking place. This is known as a state of dynamic equilibrium. Accordingly the level of ionisation is dependent upon the rate of ionisation and recombination.

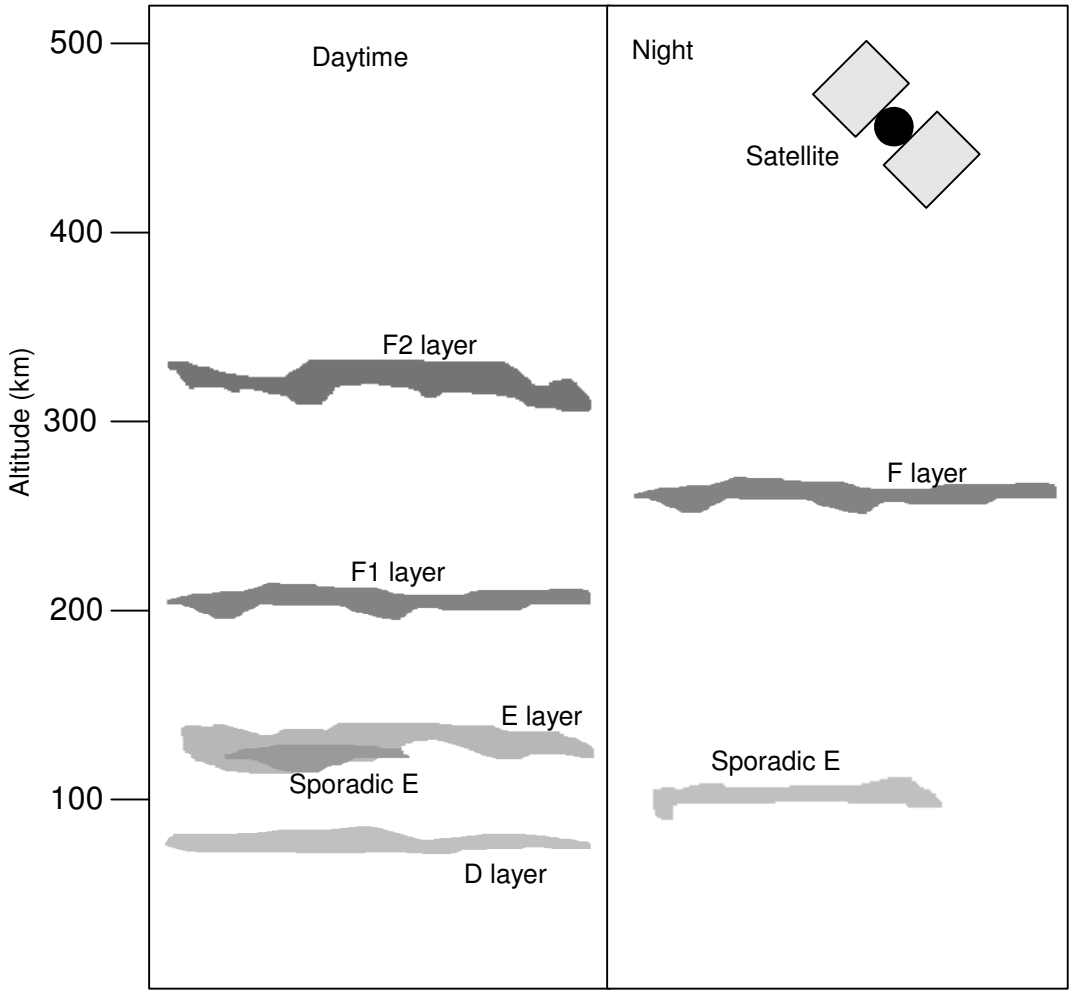

Figure 4.2: Ionosphere layers.

4.2 Layers of Ionosphere

The ionosphere is often described in terms of its component regions or layers which are firstly mentioned by E.V. Appleton. Naming convention were based upon data obtained from a myriad of radiowave measurement schemes involving vertical and oblique geometries, pulsed and CW systems, variable and constant frequencies, and different types of observables such as polarization and signal time delay [38]. For reasons related to historical development of ionospheric research, the ionosphere is divided into three regions or layers designated D,E and F respectively, in order of increasing altitude. The D layer is the innermost layer, within the ionosphere that affects radio signals to any degree. It is present

at altitudes between about 60 and 90 kilometres and the radiation within it is only present during the day to an extent, which affects radio waves noticeably. It is sustained by the radiation from the sun and levels of ionisation fall rapidly when the sun sets. In this region, electron density, which has a maximum value shortly after local solar noon and a very small value at night, exhibits large diurnal variations. The D layer mainly has the affect of absorbing or attenuating radio signals particularly LF and MF slice of the radio spectrum. At night it has little effect on most radio signals.

The altitude range from 90 - 130 kilometres constitutes the E-region and encompasses the so-called 'normal' and sporadic E layers. The former is a regular layer which displays a strong solar zenith angle dependence with maximum density near noon and important only for daytime HF propagation. Sporadic E may form at any time during the day or night. It is difficult to know where and when it will occur and how long it will persist. Sporadic E can have a comparable electron density to the F region. This means that it can refract comparable frequencies to the F region. Sometimes a sporadic E layer is transparent and allows most of the radio wave to pass through it to the F region, however, at other times the sporadic E layer obscures the F region totally and the signal does not reach the receiver which is known as *sporadic E blanketing*. Sporadic E in the low and mid-latitudes occurs mostly during the daytime. At high latitudes, it generally forms at night.

The most important region in the ionosphere for long distance HF communications is the F region. It extends upwards from about 135 kilometres and is divided into the F1 and F2 layers during the daytime when radiation is being received from the sun. Typically the F1 layer is found at around an altitude of 180 kilometres with the F2 layer above it at around 350 kilometres. The F1 layer exists only during daylight and is sometimes the reflecting region of the HF transmission. However, generally obliquely-incident waves that penetrate the E

region also penetrate the F1 layer and are reflected by the F2 layer. At night, F1 layer merges with the F2 layer at a height of about 300 kilometres [37]. Principal reflecting region for long distance HF communication is the F2 layer since it provides us with the capability to achieve the greatest skywave propagation range (by a single hop) at generally the highest allowable frequency in relation to underlying layers. The lifetime of electrons is greatest in the F2 layer which is one reason why it is present at night.

4.3 Wave Propagation through the Ionosphere

In an earth environment, electromagnetic waves propagate in ways that depend not only on their own properties but also on those of the environment itself. Waves travel in straight lines, except where the earth and the atmosphere alter their path. Waves with frequencies above HF travel in a straight line. They propagate by means of so-called space waves. They are sometimes called tropospherеic waves, since they travel in the troposphere. Frequencies below the HF range travel around the curvature of the earth. They are called ground waves or surfaces waves. Waves in the HF range are reflected by the ionised layers of the atmosphere and are called sky waves. Such signals are beamed into the sky and come down again after reflection, returning to earth well beyond the horizon. In this section, having mentioned the structure and the layers of the ionosphere, we will focus on how and in what conditions wave propagation through the ionosphere enables HF communication.

Using the optimum operational frequency is very crucial in HF communication. Not all HF waves are refracted by the ionosphere, saying that there are upper and lower frequency bounds for communication between two stations. The range of usable frequencies will change through out the day, with the seasons, from place to place and with the solar cycle. If the frequency is too low, the

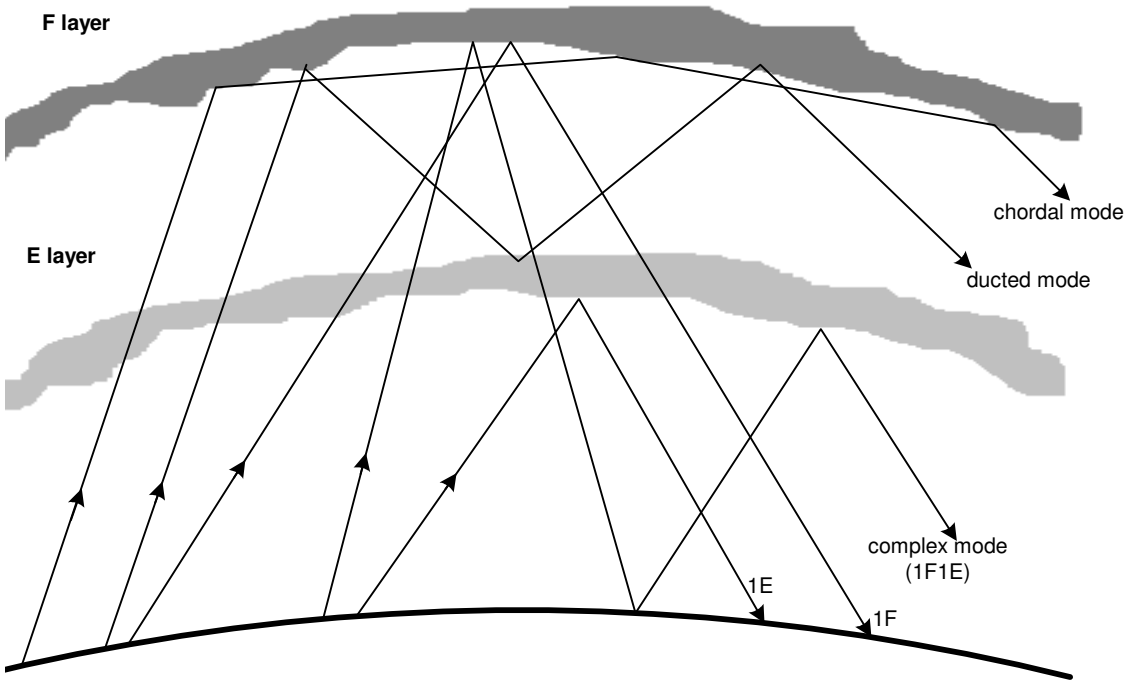

Figure 4.3: Propagation modes.

strength of the signal will be weakened by the D-region. If the frequency is too high the wave will penetrate the ionosphere. Radio waves *hop* from the earth to the ionosphere and back to the Earth. The ground distance covered by a radio signal after it has been refracted once from the ionosphere and returned to earth is called *hop length*. For E and F layer heights of 100 km and 300 km, the maximum hop lengths with an elevation angle of 4°, are approximately 1800 km and 3200 km, respectively. There are many paths by which a sky wave may travel from a transmitter to a receiver. The mode by a particular layer which requires the least number of hops between the transmitter and receiver is called the *first order mode*. If one more hop is needed then it is called *second order mode*. For instance, for a link with a path length of 5000 kilometres, the first order F mode has two hops (2F), while the second order F mode has three hops (3F).

Propagation modes can be classified as simple (modes propagated by one region; F or E layer only) and complicated (modes consisting of combinations of refractions from the E and F layers, ducting and chordal modes) modes as shown in Fig. 4.3. As far as the reflection phenomenon is concerned, many people think

of the regions of the ionosphere as being smooth, nevertheless, the ionosphere fluctuates and moves. This situation affects the refraction of the signals. The ionospheric regions may tilt and when this happens chordal and ducted modes, which involve a number of refractions from the ionosphere without intermediate reflections from the earth, may occur. Occasionally, ionospheric tilting takes place near the mid-latitude trough, equatorial anomaly and in the sunrise and sunset sectors. Since the elapsed time during the D-region traversing is less and attenuation during ground reflections, in the chordal and ducted modes, relatively signals may be strong.

Frequency, path length and antenna elevation angle are three crucial variables, combinations of which changes the ray paths considerably. For a fixed antenna elevation angle as shown in Fig. 4.4, when the frequency is increased toward the maximum usable frequency (MUF), the wave is refracted higher in the ionosphere and the range is increased (paths 1 and 2). At the MUF, maximum range is reached and above the MUF, wave penetrates the ionosphere represented by paths 3 and 4 respectively. In the second scenario, for a fixed point-to-point circuit path length seen in the Fig. 4.5, when the frequency is increased toward the MUF, the wave is refracted from higher in the ionosphere. Therefore, in order to sustain the link operation, the elevation angle should be increased (paths 1 and 2). At the MUF, path-3 operates at the critical elevation angle which is the uppermost angle before penetration. In path-4, the wave penetrates the ionosphere, since the frequency is above the MUF. For the case of fixed frequency given in the Fig. 4.6, the length of the path (path-1) is longest at low elevation angles. The path length decreases and the ray is refracted from the higher in the ionosphere when the elevation is increased represented by path-2 and path-3 successively. If the critical elevation angle is exceeded for that frequency, then the wave penetrates the ionosphere, resulting an area around the transmitter where no sky wave communication can be accomplished.

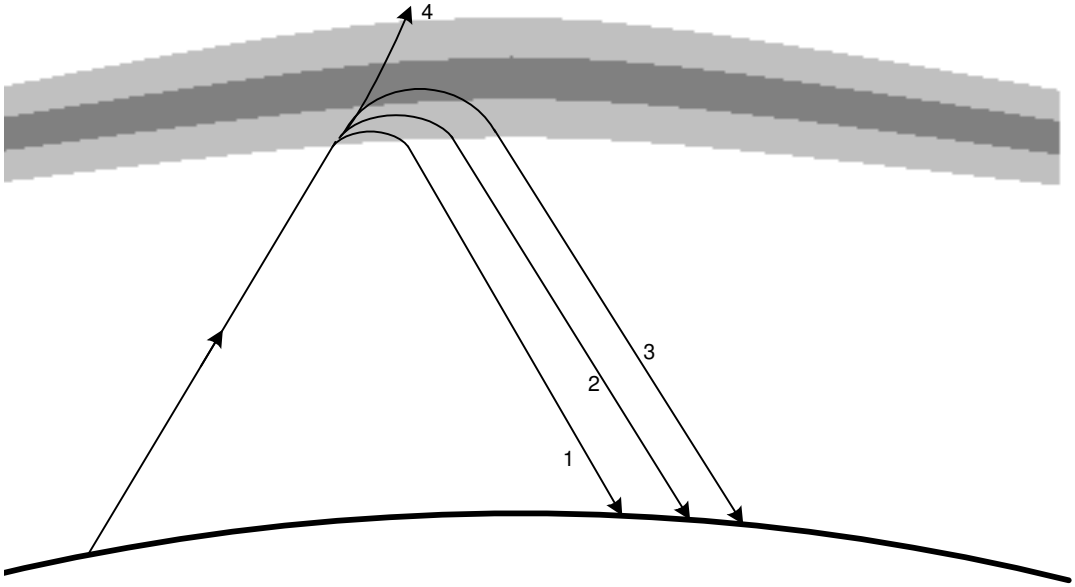

Figure 4.4: Elevation angle fixed.

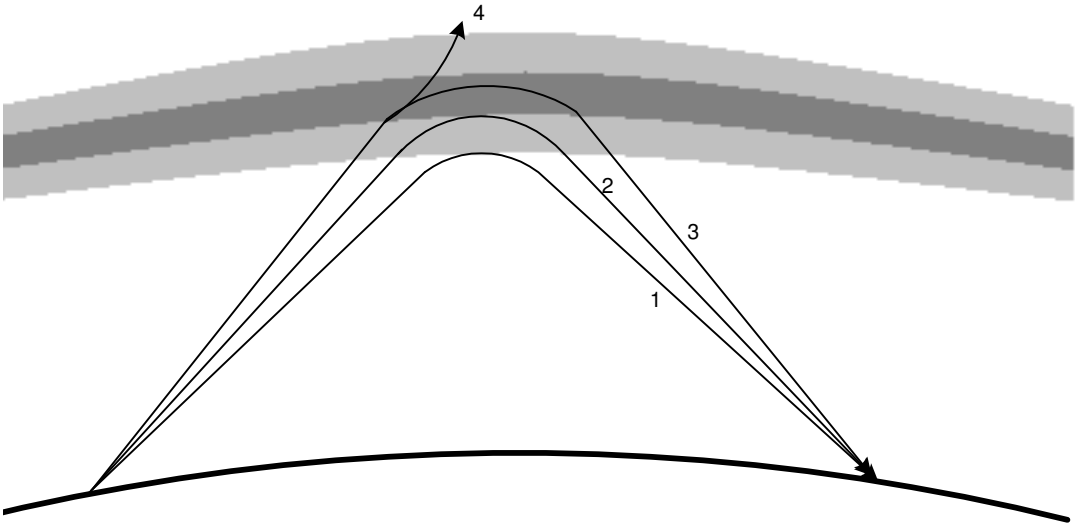

Figure 4.5: Path length fixed.

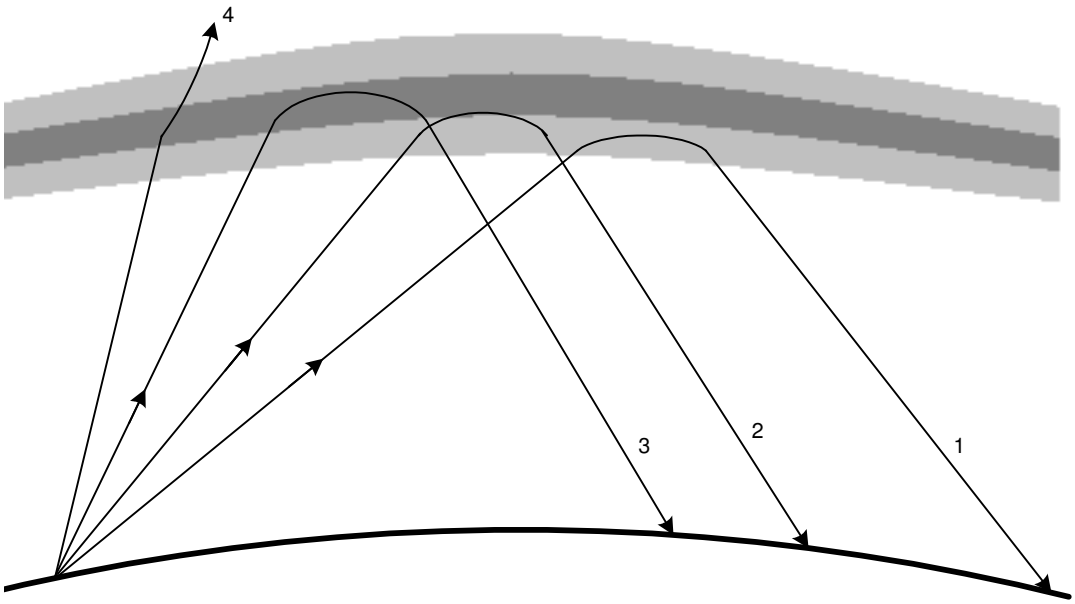

Figure 4.6: Frequency fixed.

Multipath phenomena occurs when the signal is nondispersively distended by multiple reflections from the ionosphere with or without ground reflections or when the signal is distorted by the superposition of multiple and nearly equal amplitude sources within a single layer. Fading is involved in both cases. According to their origin there are a number of different kinds of fading. The main causes are movements and changes of curvature of the electron-dense ionospheric reflector, rotation of the axes of the received polarisation ellipse, time variations of absorption and changes in electron density [37]. Moreover it is extremely important that the ionospheric irregularities within a single layer are generally in pseudorandom motion up and down, therefore in the case of micro-multipath situation one should focus on the doppler spreads.

4.4 High Latitude HF Communication

The terrestrial ionosphere may be categorized as three regions (low, mid and high latitude region) each having different properties according to their geomagnetic latitude. The high-latitude zone is the most interesting part of the ionosphere

and is also known as the our window to the distant magnetosphere. Different than the low and mid latitude zones, here the geomagnetic field runs nearly vertical, and this simple fact of nature leads to the existence of an ionosphere that is considerably more complex [37].

Auroral zones occur within the high-latitude region. Location of these zones depends on the linkage with the magnetosphere. The auroral phenomena include electrojets, which cause magnetic perturbations, and also substorms in which the rate of ionization is greatly increased by the arrival of energetic electrons. Auroral regions may be the most difficult part of the ionosphere to make a stable radio communication. Although the mechanisms causing to the formation of the trough are not completely known, it is known that one fundamental cause is the difference in circulation pattern between the inner and outer parts of the magnetosphere [37].

In closing this chapter, we can conclude that the high-latitude ionosphere is a dynamic and disturbed region containing irregularities which can severely degrade the performance of high-frequency radio systems when signals propagate through these regions. Due to this roughness, characteristics (amplitude, phase, delay, Doppler, DOA) of the signal associated with each propagation mode can be changed.

Chapter 5

ESTIMATION OF DOA, DELAY AND DOPPLER BY USING CROSS-AMBIGUITY FUNCTION

5.1 Introduction

Estimation of DOAs of signals that are delayed and Doppler shifted in the propagation channel has been a challenge for all the previously proposed array processing techniques. Since almost all wireless communication systems as well as radar and sonar systems operate in such conditions, a robust and accurate estimator of DOA's in the presence of delay and Doppler shift is very much needed. To address this challenge, in this chapter, we introduce a novel array processing technique.

Since the proposed technique makes use of cross-ambiguity function computation, we call it CAF-DF technique. It is an iterative technique, where, at each

iteration the DOA, time delay and Doppler shift corresponding to one of the signals impinging onto the array are estimated. Each iteration starts with computation of the CAF at the output of each sensor element. Then, these CAF's are incoherently integrated and the largest peak on the integrated CAF is found. Then the direction of arrival for the observed signal peak is estimated. Once the DOA of this strong signal is found, a coherent integration of the CAF's is obtained to find accurate delay and Doppler estimates. Then, the signal whose parameters are estimated is eliminated from the array outputs to search for the next strong signal component in the residual array outputs. The iterations stop when there is no detectable peak on the incoherently integrated CAF's. In the following sections we will present all the details of the CAF-DF technique.

5.2 The CAF-DF Technique

In this section we introduce a novel array processing technique to estimate DOA's of known signal components which impinge on a sensor array by propagating through paths with unknown delay and Doppler. To simplify the discussion, we will focus on the HF-DF application where the HF propagation channels have variable delay and Doppler shifts due to the dynamically nature of the ionosphere.

When a transmitter pumps a signal waveform towards the ionosphere as in Fig. 5.1, it is reflected back to the earth and intercepted by the array. The received signal at each of the array antenna outputs is an attenuated, delayed and Doppler shifted version of the transmitted one. Using the narrowband assumption, a parameterized compact data model for the array antenna outputs

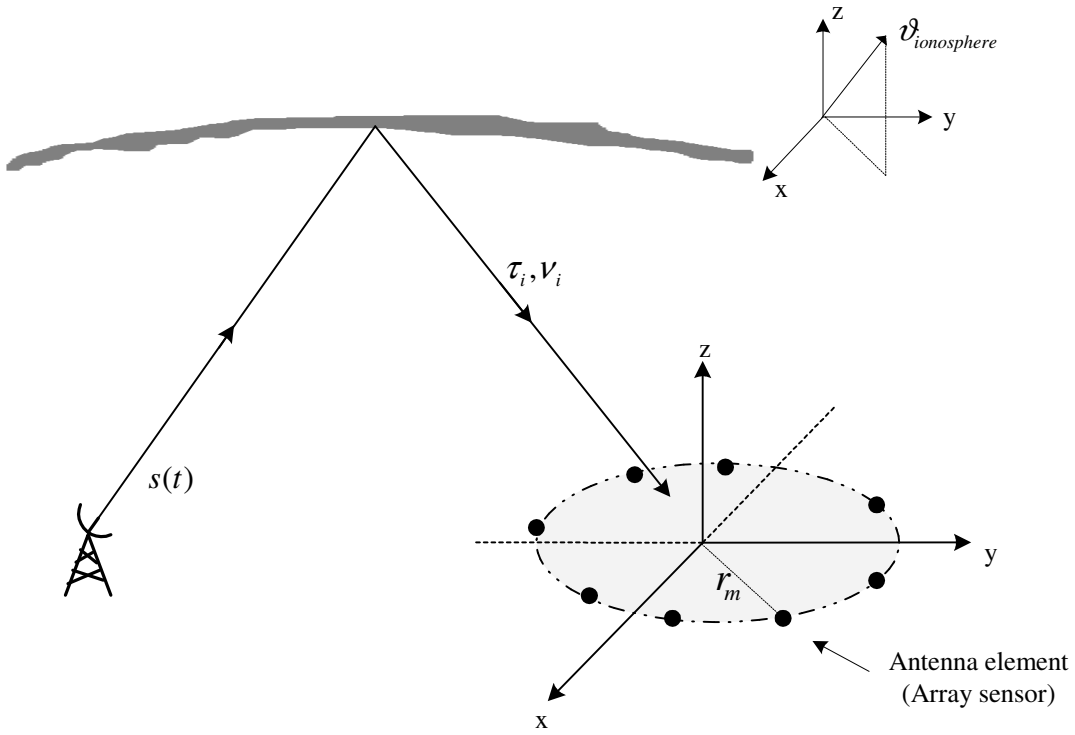

Figure 5.1: Signal transmitted to the ionosphere and reflected back to the sensor array.

were given in Eqn. 2.6 and 2.9 as

$$\mathbf{x}(t) = \begin{bmatrix} x_1(t) \\ \vdots \\ x_m(t) \end{bmatrix} \tag{5.1}$$

$$= \sum_{i=1}^{d} \mathbf{a}(\theta_i, \phi_i) s_i(t) + \mathbf{n}(t) \tag{5.2}$$

$$= \mathbf{A}(\theta, \phi)\mathbf{s}(t) + \mathbf{n}(t) \quad . \tag{5.3}$$

In this chapter, a more detailed open version of this equation, that explicitly includes the Doppler shift due to the dynamical nature of the ionosphere, will be used. In this more informative form, the m^{th} array output for only one signal path can be written as

$$x_m(t) = \zeta_{m,1} s(t - \tau_{m,1}) e^{j2\pi\nu_{m,1}(t-\xi_{m,1}(\theta,\phi))} e^{j2\pi\nu_c(t-\xi_{m,1}(\theta,\phi))} + n_m(t) \quad . \tag{5.4}$$

where $\zeta_{m,1}$ is a complex number including the amplitude attenuations and phase rotations due to reflection, $\tau_{m,1}$ is the delay, $\nu_{m,1}$ is the Doppler shift, ν_c is

the carrier frequency and $\xi_{m,1}(\theta,\phi)$) represents the phase difference of the m^{th} antenna with respect to the phase reference center or the origin of the array.

Since the structure and behavior of the ionosphere is complex, most of the time we have multiple signal paths from the sources to the antenna array. For the multipath situation, the above equation should be modified as a superposition of contributions due to each signal path:

$$x_m(t) = \sum_{i=1}^{d} \zeta_{m,i} s(t-\tau_{m,i}) e^{j2\pi\nu_{m,i}(t-\xi_{m,i}(\theta,\phi))} e^{j2\pi\nu_c(t-\xi_{m,i}(\theta,\phi))} + n_m(t) \quad . \tag{5.5}$$

As seen from the Fig. 5.1, location of the each antenna is different with respect to the origin of the array. Therefore path delay of the signal from transmitter to the each antenna will be different. If we label the path delay of the signal from transmitter to the origin of the array as $\tau_{0,i}$, then we can write that

$$\tau_{m,i} = \tau_{0,i} + \delta_{m,i} \tag{5.6}$$

where $\delta_{m,i}$ is the delay difference of the each antenna, due to their orientation, to the array origin. Hence the m^{th} antenna output can be written as:

$$x_m(t) = \sum_{i=1}^{d} \zeta_{m,i} s(t-\tau_{0,i}-\delta_{m,i}) e^{j2\pi\nu_{m,i}(t-\xi_{m,i}(\theta,\phi))} e^{j2\pi\nu_c(t-\xi_{m,i}(\theta,\phi))} + n_m(t) \quad . \tag{5.7}$$

In order to resolve the phase ambiguities, array antenna spacings should be smaller than or equal to the half of the wavelength. For narrowband signals, the time delay appears as a pure phase delay of the reference signal. Moreover, this phase delay depends only on the spacing between the array elements and the angle-of-arrival of the plane wave and is independent of the time variable. As a result, Eqn. (5.7) can be simplified as;

$$x_m(t) = \sum_{i=1}^{d} \zeta_{m,i} s(t-\tau_{0,i}) e^{j2\pi\nu_{m,i}(t-\xi_{m,i}(\theta,\phi))} e^{j2\pi\nu_c(t-\xi_{m,i}(\theta,\phi))} + n_m(t) \quad . \tag{5.8}$$

A few more simplifications can be done on this equation. Doppler shift corresponding to an impinging signal can be taken same for each sensor:

$$\nu_{m,i} = \nu_i \quad . \tag{5.9}$$

Additionally, for small Doppler shifts:

$$e^{-j2\pi\nu_i\xi_{m,i}(\theta,\phi)} \simeq 1 \quad . \tag{5.10}$$

Lastly, if we convert (5.8) down to baseband, our fundamental equation at the output of the m^{th} antenna becomes

$$x_m(t) = \sum_{i=1}^{d} \zeta_{m,i} s(t-\tau_{0,i}) e^{j2\pi\nu_i t} e^{-j2\pi\nu_c\xi_{m,i}(\theta,\phi)} + n_m(t) \quad . \tag{5.11}$$

Starting point of our algorithm is to estimate the direction-of-arrival information which is hidden in the $e^{-j2\pi\nu_c\xi_{m,i}(\theta,\phi)}$. By using the cross-ambiguity function processing, angle estimates will be extracted from Eqn. 5.11. In order to do that, first of all, lets give the continuous time symmetrical form of the cross-ambiguity function as follow;

$$\chi_{x_m,s} = \int_{-\infty}^{\infty} x_m(t+\frac{\tau}{2})\, s^*(t-\frac{\tau}{2})\, e^{-j2\pi\nu t}\, dt \quad . \tag{5.12}$$

Although theoretically useful, the continuous form of the CAF is not practical for real time computations. Therefore, the discrete form of the CAF should be used in our approach. In the discrete form both τ and ν is discretized and the integral is approximated by a Riemann sum. To compute the discrete values of time delay and doppler, some a priori information is needed which includes the max/min doppler (from largest expected velocity difference) and max/min time delay (from largest expected range difference). The max/min values allow for computation of a precise number of dopplers and time delays that are of interest to use in computation of the CAF. Two other important values needed are the delay spacing (taken from expected/measured signal bandwidth) and the doppler spacing (taken from the observation time interval, T). These values dictate how fine a grid of time delays and dopplers that will be used in conjunction with the number of time delays and dopplers. For lossless digitization, the sampling rate is chosen to be at least twice the maximum frequency responses. The discrete time version of the (5.12) can be written as

$$\chi_{x_m,s}(k\Delta\tau, l\Delta\nu) = \frac{\Delta\tau}{2} \sum_n x_m\big(n\frac{\Delta\tau}{2} + k\frac{\Delta\tau}{2}\big) s^*\big(n\frac{\Delta\tau}{2} - k\frac{\Delta\tau}{2}\big) e^{-j2\pi l\Delta\nu n\frac{\Delta\tau}{2}} \tag{5.13}$$

where $\Delta\tau$ and $\Delta\nu$ represents delay and doppler spacings, k and l are the number of delay and doppler spacings respectively.

One can make this equation look like the Fourier transform of a function by a simple variable modification. Assume that the length of DFT is L and if we make the replacement below

$$2\pi l\Delta\nu n\frac{\Delta\tau}{2} = \frac{2\pi}{L}nl \quad , \tag{5.14}$$

(5.13) becomes

$$\chi_{x_m,s}(k\Delta\tau, l\Delta\nu) = \frac{\Delta\tau}{2}\sum_n x_m\big(n\frac{\Delta\tau}{2} + k\frac{\Delta\tau}{2}\big)s^*\big(n\frac{\Delta\tau}{2} - k\frac{\Delta\tau}{2}\big)e^{-j\frac{2\pi}{L}nl} \tag{5.15}$$

$$= \frac{\Delta\tau}{2}\sum_n x_m\big(\frac{\Delta\tau}{2}(n+k)\big)s^*\big(\frac{\Delta\tau}{2}(n-k)\big)e^{-j\frac{2\pi}{L}nl} \tag{5.16}$$

$$= \frac{\Delta\tau}{2}\sum_n x_m[n+k]s^*[n-k]e^{-j\frac{2\pi}{L}nl} \tag{5.17}$$

$$= \frac{\Delta\tau}{2}\sum_n h_k[n]e^{-j\frac{2\pi}{L}nl} \tag{5.18}$$

$$= \frac{\Delta\tau}{2}DFT_L(h_k[n]) \quad , \tag{5.19}$$

In Chapter 2, we plotted the ambiguity function distribution of a uniform pulse train and observed that doppler resolution is related with the length of the pulse train. For the cases of long duration signals, such as the recorded real ionospheric echo signals whose length can be more than 20000 samples, Eqn. (5.19) becomes inefficient to implement. Moreover, we are not interested in the whole doppler spectrum. Therefore, it would be wise to narrow our doppler search range to the physically expected range of values. One way of achieving this purpose is to use the chirp Z-transform (CZT) [39]. The CZT is proposed to compute Z-transform of a sequence on arbitrary number of uniformly spaced samples lying on circular or spiral contours, such as the ones shown in Fig. 5.2, beginning at any arbitrary point in the Z-transform domain.

By choosing the Z-transform domain contour as a segment of the unit circle, the CZT returns the same result as the DFT, but it is limited to a discrete-frequency band;

$$|l| \leq \frac{\nu_{max}}{\Delta\nu} \tag{5.20}$$

$$-N_D \leq |l| \leq N_D \quad . \tag{5.21}$$

where ν_{max} is the maximum doppler shift and N_D is the number of frequency samples to be focused on. For implementation purposes, lets make the doppler index start from 0 and finish at $2N_D$ by introducing a new variable $\check{l}$,

$$\check{l} = l + N_D \quad . \tag{5.22}$$

If we update (5.18) with this change of variable we get

$$\chi_{x_m,s}(k\Delta\tau, (\check{l} - N_D)\Delta\nu) = \frac{\Delta\tau}{2} \sum_n h_k[n] e^{-j\frac{2\pi}{L}n(\check{l}-N_D)} \tag{5.23}$$

$$= \frac{\Delta\tau}{2} \sum_n h_k[n] e^{j\frac{2\pi}{L}nN_D} e^{-j\frac{2\pi}{L}n\check{l}} \tag{5.24}$$

$$= \frac{\Delta\tau}{2} \sum_n \check{h}_k[n] e^{-j\frac{2\pi}{L}n\check{l}} \tag{5.25}$$

$$= \frac{\Delta\tau}{2} \sum_n \check{h}_k[n] z_{\check{l}}^{-n} \quad . \tag{5.26}$$

The CZT is not restricted to operate along the unit circle. It can evaluate the Z-transform along contours described by

$$z_{\check{l}} = e^{j\frac{2\pi}{N}\check{l}} \qquad \check{l} = 0, ..., 2N_D \tag{5.27}$$

$$= AW^{-\check{l}} \tag{5.28}$$

$$A = A_0 e^{j2\pi\Theta_0} \tag{5.29}$$

$$W = W_0 e^{j2\pi\Phi_0} \tag{5.30}$$

where A is the complex starting point, W is a scalar describing the ratio between points on the contour, and $2N_D + 1$ is the length of the transform. If we have

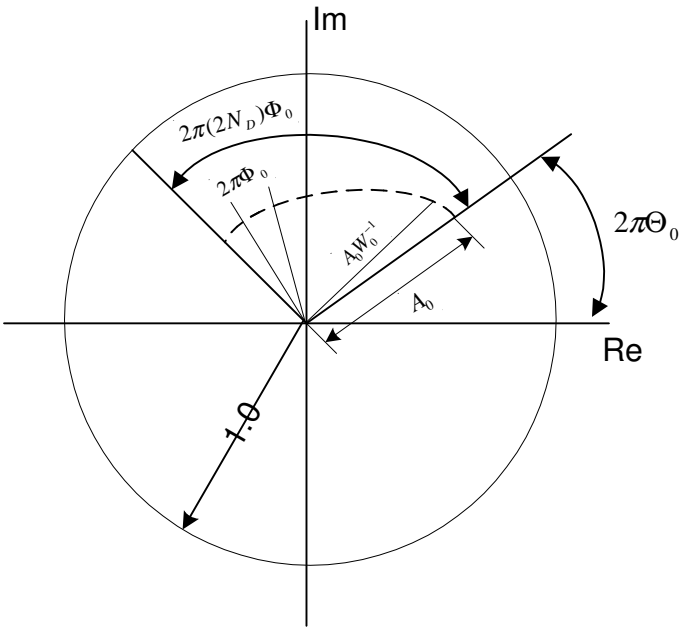

Figure 5.2: z-domain circle

$A = 1$, $2N_D + 1 = N$ and $W = e^{-j2\pi/N}$ then the Z-transform on this contour is simply the DFT. Moreover, if $W_0 = 1$ the contour is an arc of circle. In Fig.5.2, a spiral contour where the Z-transform is evaluated is seen [39]. Having substituted (5.28) into (5.26), we obtain;

$$\chi_{x_m,s}(k\Delta\tau, (\check{l} - N_D)\Delta\nu) = \frac{\Delta\tau}{2} \sum_n \check{h}_k[n] A^{-n} W^{n\check{l}} \tag{5.31}$$

$$for \quad 0 \leq \check{l} \leq 2N_D \quad .$$

Additionally, if we use the substitution described by Bluestein in [40],

$$n\check{l} = \frac{n^2 + \check{l}^2 - (\check{l} - n)^2}{2} \tag{5.32}$$

for the exponent of W in (5.31), we thus get

$$\chi_{x_m,s}(k\Delta\tau,(\check{l}-N_D)\Delta\nu) = \frac{\Delta\tau}{2}\sum_n \check{h}_k[n]A^{-n}W^{[n^2+\check{l}^2-(\check{l}-n)^2]/2} \tag{5.33}$$

$$= \frac{\Delta\tau}{2}\sum_n \check{h}_k[n]A^{-n}W^{n^2/2}W^{\check{l}^2/2}W^{-(\check{l}-n)^2/2} \tag{5.34}$$

$$= \frac{\Delta\tau}{2}W^{\check{l}^2/2}\sum_n \left(\check{h}_k[n]A^{-n}W^{n^2/2}\right)W^{-(\check{l}-n)^2/2} \tag{5.35}$$

$$for \quad 0 \le \check{l} \le 2N_D \quad .$$

This summation is precisely a linear convolution of the two sequences $g_k[n]$ and $p[n]$ of length N defined by

$$g_k[n] = \check{h}_k[n]A^{-n}W^{n^2/2} \tag{5.36}$$

$$p[n] = W^{-n^2/2} \quad , \tag{5.37}$$

with the output of the convolution multiplied by $\frac{\Delta\tau}{2}p[\check{l}]^*$. That is:

$$\chi_{x_m,s}(k\Delta\tau,(\check{l}-N_D)\Delta\nu) = \frac{\Delta\tau}{2}p[\check{l}]^*\sum_n g_k[n]p[\check{l}-n] \tag{5.38}$$

$$for \quad 0 \le \check{l} \le 2N_D \quad .$$

As revealed by this equation, $\chi_{x_m,s}(k\Delta\tau,(\check{l}-N_D)\Delta\nu)$ is a weighted convolution of sequences $g_k[n]$ and $p[n]$, and can be computed efficiently by using FFT based convolution techniques.

In the proposed array signal processing technique, we will make use of this efficient implementation of the CAF computation for each antenna output in the array. In Fig. 5.3, two different views of the CAF computation of the received signal, which is a barker-13 coded pulse train, with the transmitted Barker-13 pulse train signal is given.

If we have more than one signal source impinging on the antenna array, CAF of the transmitted and received signals at each antenna output may have multiple

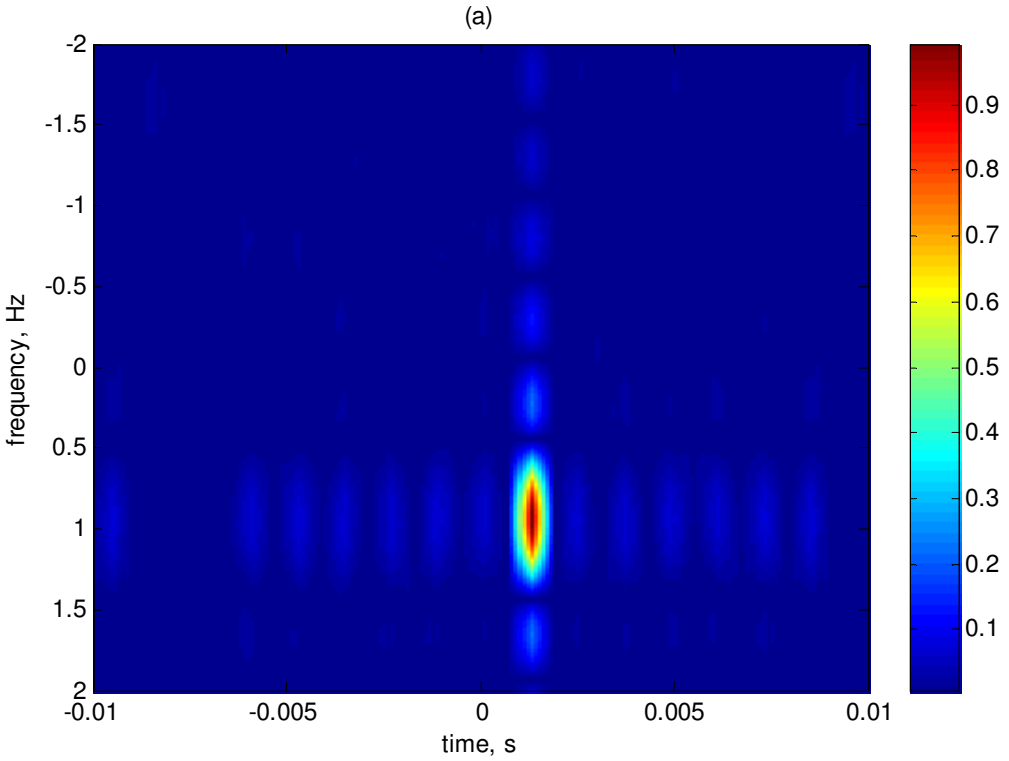

(a) Top view of CAF

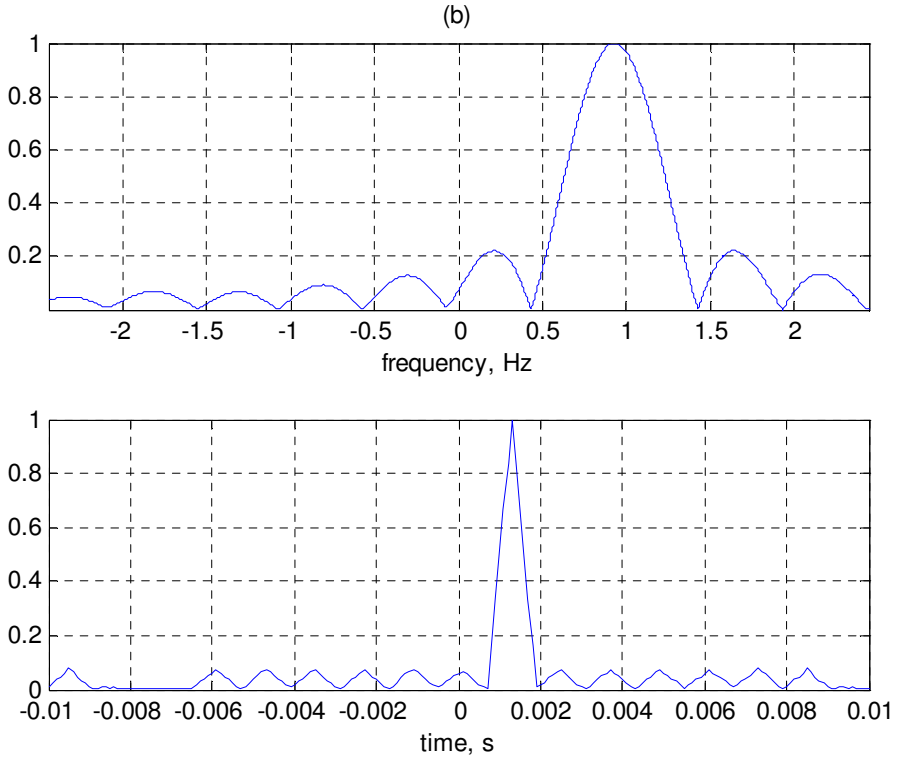

(b) Time and frequency slices of CAF crossing at the peak location

Figure 5.3: Result of the CAF computation for the m^{th} antenna output with transmitted signal when only one signal path exists.

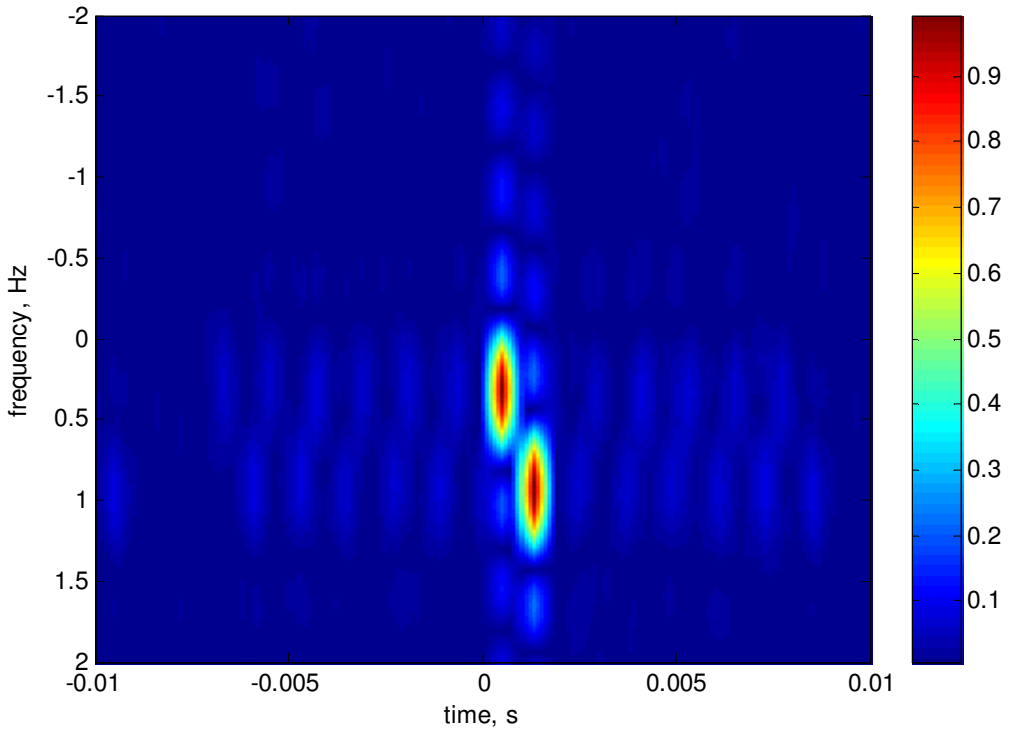

Figure 5.4: Result of the CAF computation for the m^{th} antenna output with the transmitted signal for the case of two signal paths.

discernible peaks as shown in Fig. 5.4. Since the antennas in the array are closely spaced, peak locations of the CAFs will be nearly the same for each antenna. Adding up the absolute values of the CAF of each antenna output provides the following incoherent integration

$$\chi_{total} = |\chi_{x_1,s}| + |\chi_{x_2,s}| + \ldots + |\chi_{x_M,s}| \quad , \tag{5.39}$$

which make it easier to detect the peaks due to actual signal paths above the noise level. Therefore, the SNR at the peak detection phase is improved resulting in more precise detection of the delay and doppler coordinates of the peak. The procedure is illustrated in Fig. 5.5, using a real ionospheric five-element array data set. It is seen from the resultant normalized CAF surface that the noise level is suppressed relative to the peak when compared to the individual CAF surfaces.

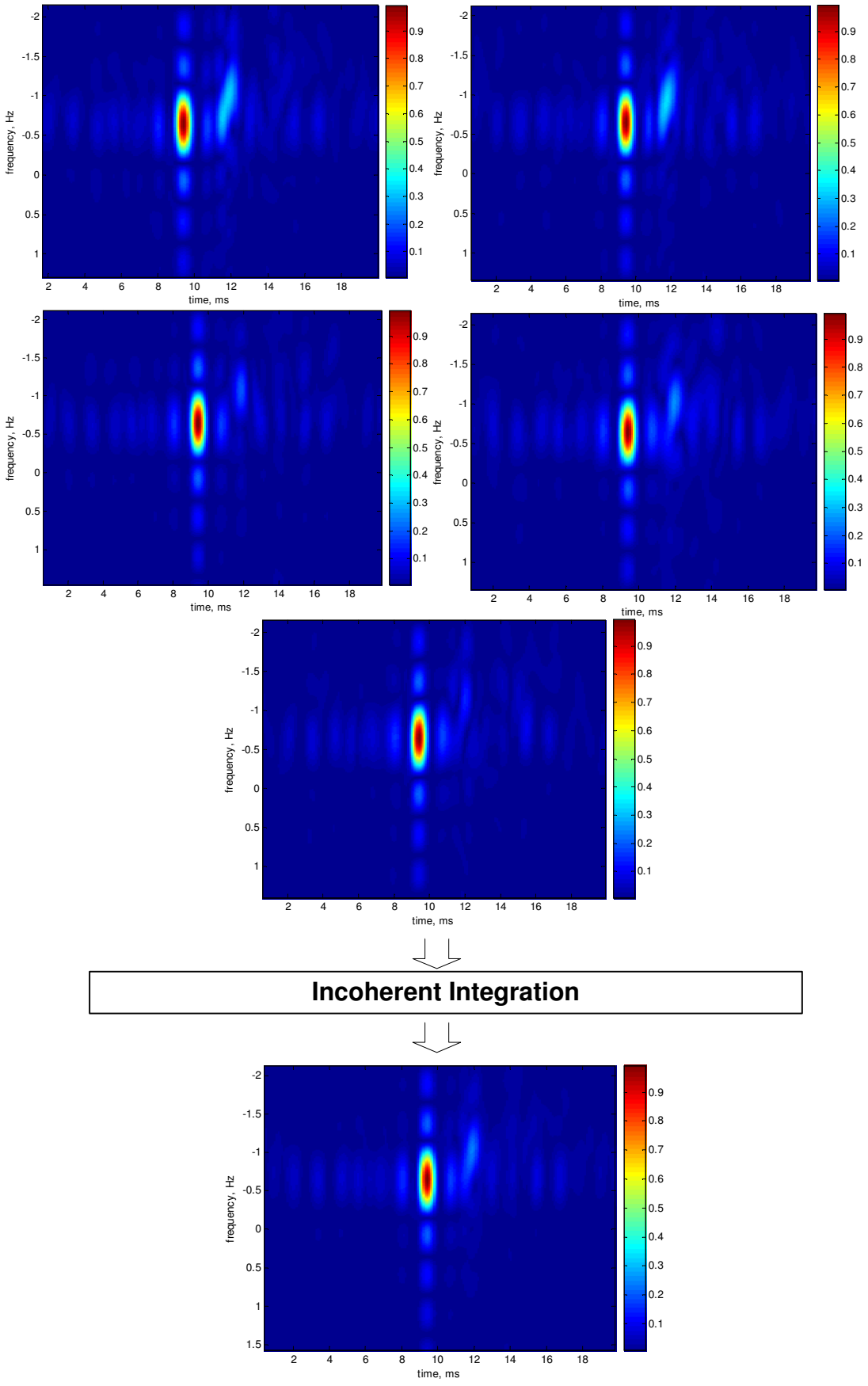

Figure 5.5: Incoherent integration of the CAF surfaces.

Using the delay and doppler location of the highest peak point, a vector will be created as below;

$$\boldsymbol{P}_p = \begin{bmatrix} \chi_{x_1,s}(\tau_p,\nu_p) \\ \chi_{x_2,s}(\tau_p,\nu_p) \\ \vdots \\ \chi_{x_M,s}(\tau_p,\nu_p) \end{bmatrix}_{M,1} = \begin{bmatrix} \left|\chi_{x_1,s}(\tau_p,\nu_p)\right| e^{j\Psi_1} \\ \left|\chi_{x_2,s}(\tau_p,\nu_p)\right| e^{j\Psi_2} \\ \vdots \\ \left|\chi_{x_M,s}(\tau_p,\nu_p)\right| e^{j\Psi_M} \end{bmatrix}_{M,1} . \tag{5.40}$$

As mentioned before, DOA information is captured in the phases of this vector entries. The following vector whose elements include the relative phase of each antenna with respect to the origin due to DOA of a hypothetical signal source impinging on the antenna array will be used to estimate the DOA of the signal corresponding to the highest peak:

$$\boldsymbol{S}(\hat{\theta},\hat{\phi}) = \frac{1}{\sqrt{M}} \begin{bmatrix} e^{j\xi_{1,1}(\hat{\theta},\hat{\phi})} \\ e^{j\xi_{2,1}(\hat{\theta},\hat{\phi})} \\ \vdots \\ e^{j\xi_{M,1}(\hat{\theta},\hat{\phi})} \end{bmatrix} , \tag{5.41}$$

here, $\hat{\theta}$ and $\hat{\phi}$ are the azimuth and elevation angle of the hypothetical signal source. To estimate the DOA of the signal corresponding to the highest peak, we make a search in the $(\hat{\theta},\hat{\phi})$ space and choose an azimuth and elevation pair, which satisfies the following criteria;

$$(\hat{\theta_p},\hat{\phi_p}) = \arg\max_{\hat{\theta},\hat{\phi}} \frac{1}{1 - \dfrac{|\boldsymbol{P}_p^H \boldsymbol{S}(\hat{\theta},\hat{\phi})|}{\|\boldsymbol{P}_p\|}} . \tag{5.42}$$

For the scenario in Fig. 5.4, the search surface for the $\hat{\theta_p}$ and $\hat{\phi_p}$ is illustrated in Fig. 5.6. The location of the peak provides the DOA estimates. Note that, the search is conducted on a discrete grid in the search domain. Therefore, the obtained estimates differ from the actual DOAs related with the grid spacing of $\frac{\Delta\theta}{2}$ and $\frac{\Delta\phi}{2}$ in elevation and azimuth respectively. At high SNR, this grid spacing determines the accuracy of our estimates. Assuming uniform distributions, the error in the obtained estimates will have standard deviations of $\frac{\Delta\theta}{\sqrt{12}}$ and $\frac{\Delta\phi}{\sqrt{12}}$

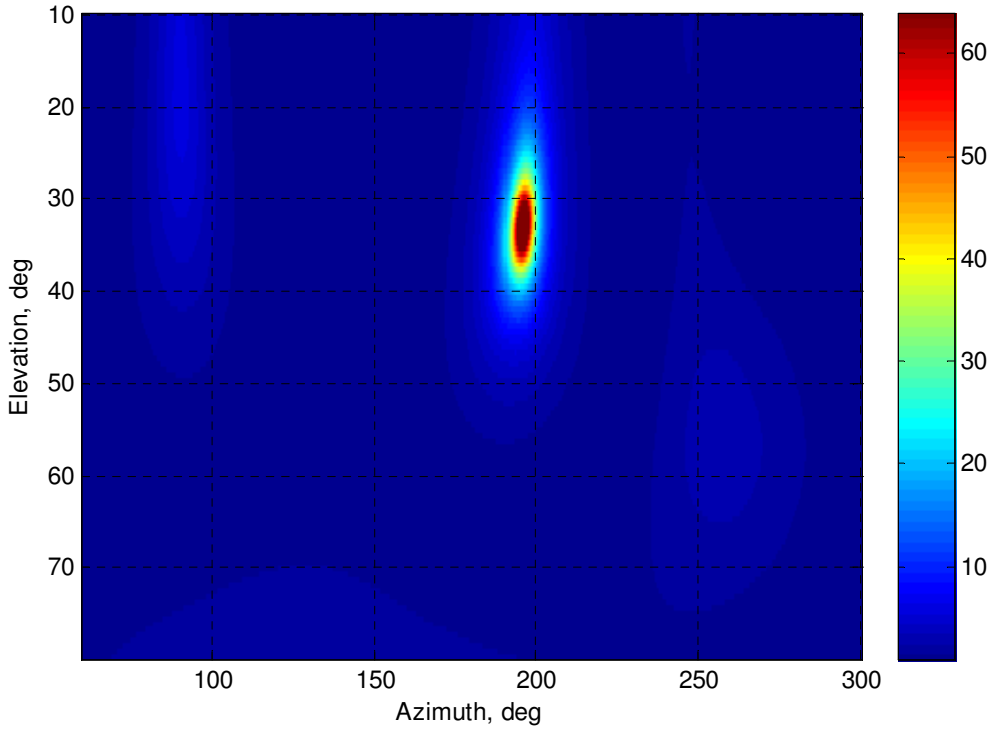

Figure 5.6: Evaluation of the (5.42) and resultant DOA (Azimuth=195.6 deg, Elevation=32.2 deg) estimate.

in elevation and azimuth respectively. This error floor at high SNR can be decreased by using finer grids in the search or by using polynomial fit techniques to the search surface around the estimated peak locations of the grid based search. Although these improvements are leaved as a future work, we derived the Cramer-Rao lower bound for this joint estimation problem and gave the elements of Fisher Information Matrix (FIM) in Appendix-A.

Once $\hat{\theta}_p$ and $\hat{\phi}_p$ estimates are obtained, we can now modify the array outputs for a coherent integration with enhanced signal reception and simultaneous suppression of the undesired noise and interference from other signals. To illustrate the SNR improvement, Eqn. (5.11) may be simplified for a single path as follows

$$x_m(t) = \check{s}(t)e^{-j2\pi\nu_c\xi_{m,1}(\theta,\phi)} + n_m(t) \quad . \tag{5.43}$$

Corresponding input SNR is

$$SNR_m = \frac{E[|\check{s}(t)|^2]}{E[|n_m(t)|^2]} = \frac{\mathbf{E}_{\check{s}}}{\sigma^2} \quad , \tag{5.44}$$

where $\mathbf{E}_{\check{s}}$ is the signal energy. From (5.43) the signal components can be coherently combined if the array outputs are phase shifted by $e^{j2\pi\nu_c\xi_{m,1}(\hat{\theta}_p,\hat{\phi}_p)}$; $m = 1, 2, \ldots, M$ and the signals are added up. Assuming that $\hat{\theta}_p$ and $\hat{\phi}_p$ are accurate, this gives the output signal $x_{total}(t)$ to be

$$x_{total}(t) = \sum_{m=1}^{M} x_m(t) e^{j2\pi\nu_c\xi_{m,1}(\theta,\phi)} \tag{5.45}$$

$$= M\check{s}(t) + \sum_{m=1}^{M} n_m(t) e^{j2\pi\nu_c\xi_{m,1}(\theta,\phi)} \tag{5.46}$$

$$= M\check{s}(t) + n(t) \quad . \tag{5.47}$$

The output SNR in this case is given by

$$SNR_o = \frac{E[|M\check{s}(t)|^2]}{E[|n(t)|^2]} \tag{5.48}$$

$$= \frac{M^2\mathbf{E}_{\check{s}}}{M\sigma^2} \tag{5.49}$$

$$= M.SNR_m \quad . \tag{5.50}$$

As a result, coherent integration of the sensor outputs results in an improvement in the SNR by a factor equal to the number of array elements. The phase compensation procedure in Eqn. (5.47) is illustrated as in Fig. 5.7, where the slow-time versions (sampled version of the pulse train with pulse repetition interval) of the antenna outputs are seen. If phase shifting with respect to the origin occurs with the correct DOA estimates than output slow-time signals overlap as in the Fig. 5.7(b). Now we can make use of the SNR improved signal by calculating CAF response with the transmitted waveform, to estimate the delay and Doppler more accurately. In Fig. 5.8, CAF of the coherently integrated sensor outputs is seen. Note that, interference from other signal paths and noise level is lower than the incoherently integrated CAF. Corresponding time-axis and frequency values of the peak point on this surface are our delay and Doppler estimates.

Thus, we have estimated the azimuth, elevation, delay and Doppler of one of the impinging signals. Using the four estimated parameters, a copy of the

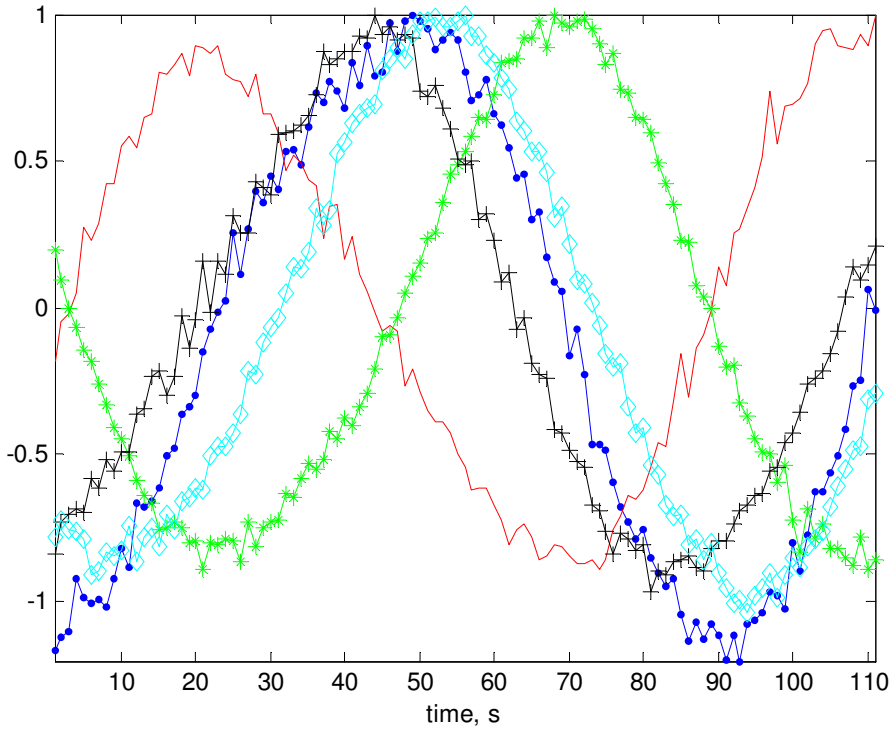

(a)

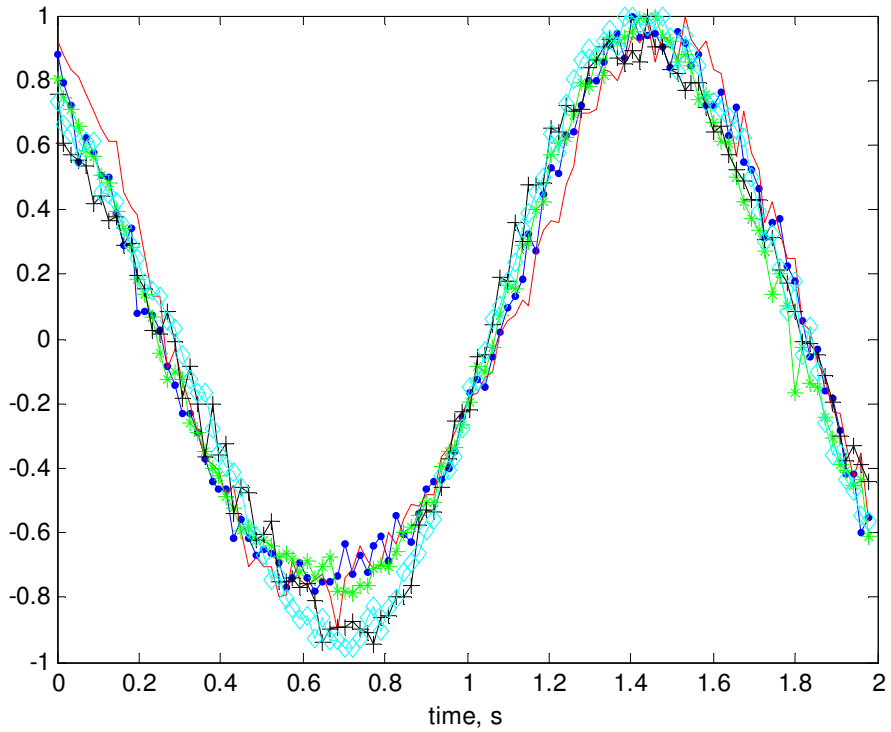

(b)

Figure 5.7: Slow-time representation of the 5-element array output. (a)before phase compensation (b)after phase compensation with the first DOA estimate.

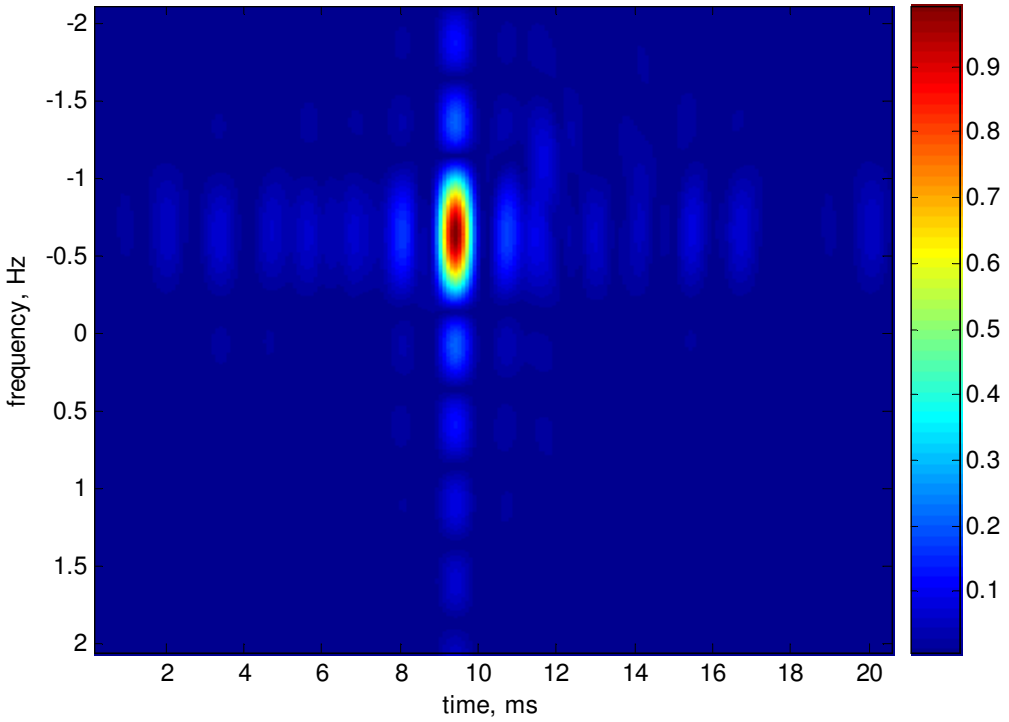

Figure 5.8: CAF of the coherently integrated sensor outputs.

impinging signal at each antenna can be obtained as;

$$x_{m,p_1}(t) = \hat{\zeta}_{m,p_1} s(t - \hat{\tau}_{0,p1}) e^{j2\pi\hat{\nu}_{p1}t} e^{-j2\pi\nu_c \xi_{m,p_1}(\hat{\theta},\hat{\phi})} \quad m = 1, 2, \ldots, M \quad , \quad (5.51)$$

where p_1 represents the first detected path and $\hat{\zeta}_{m,p_1}$ is a complex value, which covers all the phase shifts and attenuation effects and modeled as an uniformly distributed phase between 0 and 2π. Depending on the calibration capabilities of the antenna array, $\hat{\zeta}_{m,p_1}$ value may be different or same for each antenna. A cost function to estimate the fifth parameter of the m^{th} antenna output signal can be;

$$J_m(\zeta_{m,p_1}) = \int_0^T \left| x_m(t) - x_{m,p_1}(t) \right|^2 dt \quad (5.52)$$

The minimizer $\hat{\zeta}_{m,p_1}$ of this quadratic cost function with respect to ζ_{m,p_1} can be obtained easily by the following derivative condition:

$$\int_0^T \frac{\partial\left(\left| x_m(t) - x_{m,p_1}(t) \right|^2 \right)}{\partial \zeta_{m,p_1}} = 0 \quad (5.53)$$

which implies the following two equalities:

$$2\int_0^T s^*(t-\hat{\tau}_{0,p1})e^{-j2\pi\hat{\nu}_{p1}t}e^{j2\pi\nu_c\xi_{m,p_1}(\hat{\theta},\hat{\phi})}\big(x_m(t)-x_{m,p_1}(t)\big)dt=0 \tag{5.54}$$

$$\int_0^T s^*(t-\hat{\tau}_{0,p1})e^{-j2\pi\hat{\nu}_{p1}t}e^{j2\pi\nu_c\xi_{m,p_1}(\hat{\theta},\hat{\phi})}x_m(t)dt=\hat{\zeta}_{m,p_1}\int_0^T s^*(t-\hat{\tau}_{0,p1})s(t-\hat{\tau}_{0,p1})dt\ . \tag{5.55}$$

Hence the $\hat{\zeta}_{m,p_1}$ can be obtained as

$$\hat{\zeta}_{m,p_1}=\frac{\displaystyle\int_0^T s^*(t-\hat{\tau}_{0,p1})e^{-j2\pi\hat{\nu}_{p1}t}e^{j2\pi\nu_c\xi_{m,p_1}(\hat{\theta},\hat{\phi})}x_m(t)dt}{\displaystyle\int_0^T s^*(t-\hat{\tau}_{0,p1})s(t-\hat{\tau}_{0,p1})dt}\ . \tag{5.56}$$

If ζ is assumed to be same for each of the antennas, then (5.56) can be modified as below,

$$\hat{\zeta}_{p_1}=\frac{\displaystyle\sum_{m=1}^{M}\int_0^T s^*(t-\hat{\tau}_{0,p1})e^{-j2\pi\hat{\nu}_{p1}t}e^{j2\pi\nu_c\xi_{m,p_1}(\hat{\theta},\hat{\phi})}x_m(t)dt}{M\displaystyle\int_0^T s^*(t-\hat{\tau}_{0,p1})s(t-\hat{\tau}_{0,p1})dt}\ . \tag{5.57}$$

Having determined the copy of the first signal path at each antenna output, we can eliminate it by simply subtracting its respective copy from each antenna output in order to start our search procedure for other signal paths if they exist. This simple elimination procedure is the key in the success of the proposed approach. The sidelobes in the CAF domain due to the first signal path, may be stronger than the second target's echo. The elimination of the first signal path results in the elimination of the first signal path related sidelobes in the CAF domain as well. Therefore after the elimination, we can start our search for a second signal path in the CAF domain with confidence. In Fig. 5.9, synthetically generated copy of the first signal path on only three antenna output is plotted with real slow-time data. A strong correspondence is seen with the real data. After the elimination, the cross-ambiguity surface is changed such that first dominant peak and all the sidelobes of first signal path are disappeared as in Fig. 5.10 for each antenna. Therefore, better and accurate estimation of the

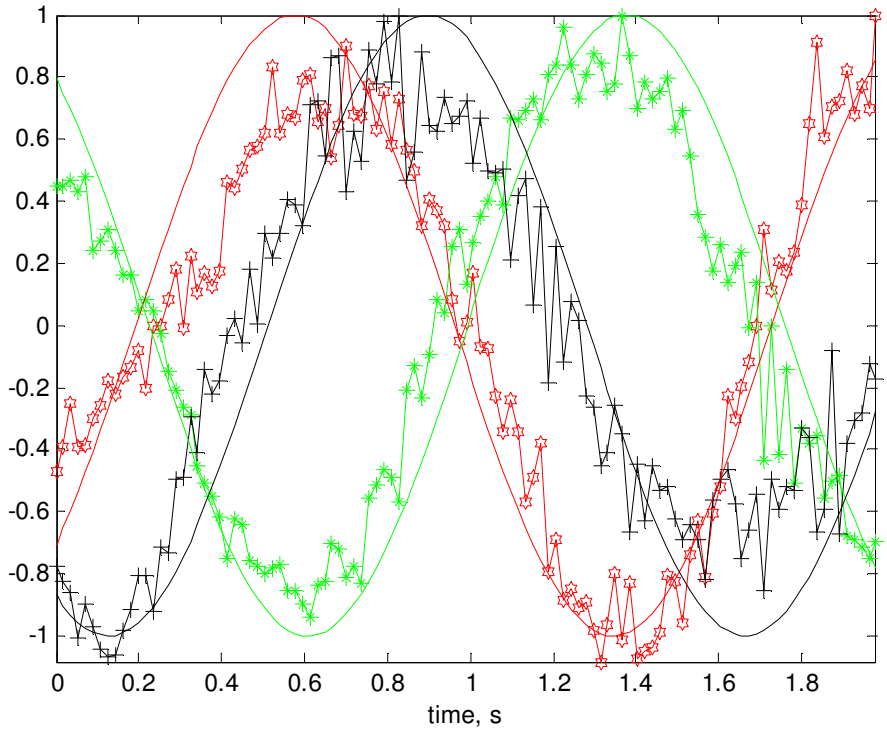

Figure 5.9: Synthetically generated copy of the first signal path on three antenna output with original slow-time data. Marked lines represent the real data and smooth lines for synthetic signal.

second signal path will be possible. The block diagram of the proposed iterative CAF-DF technique is given in Fig. 5.11.

Computational estimation procedure can be divided into mainly two parts as CAF calculation and spatial angle search, as far as the computational complexity is concerned. Number of delay and Doppler samples determine the computational cost of CAF computation. However, in spatial angle search, computational cost is determined by angle resolution of the search grid both in azimuth and elevation.

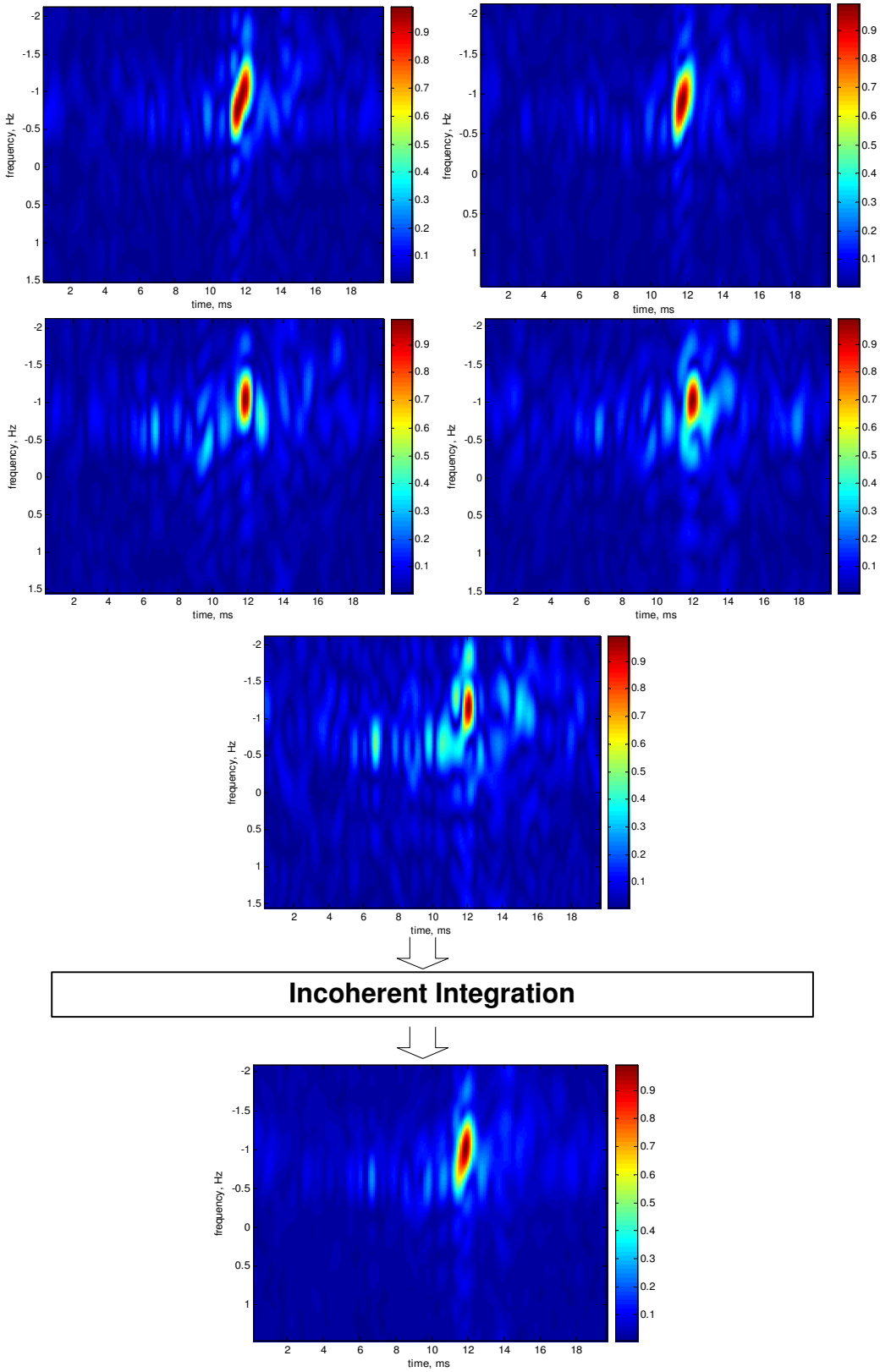

Figure 5.10: Incoherent integration of the computed CAF surfaces of each antenna output for the second path.

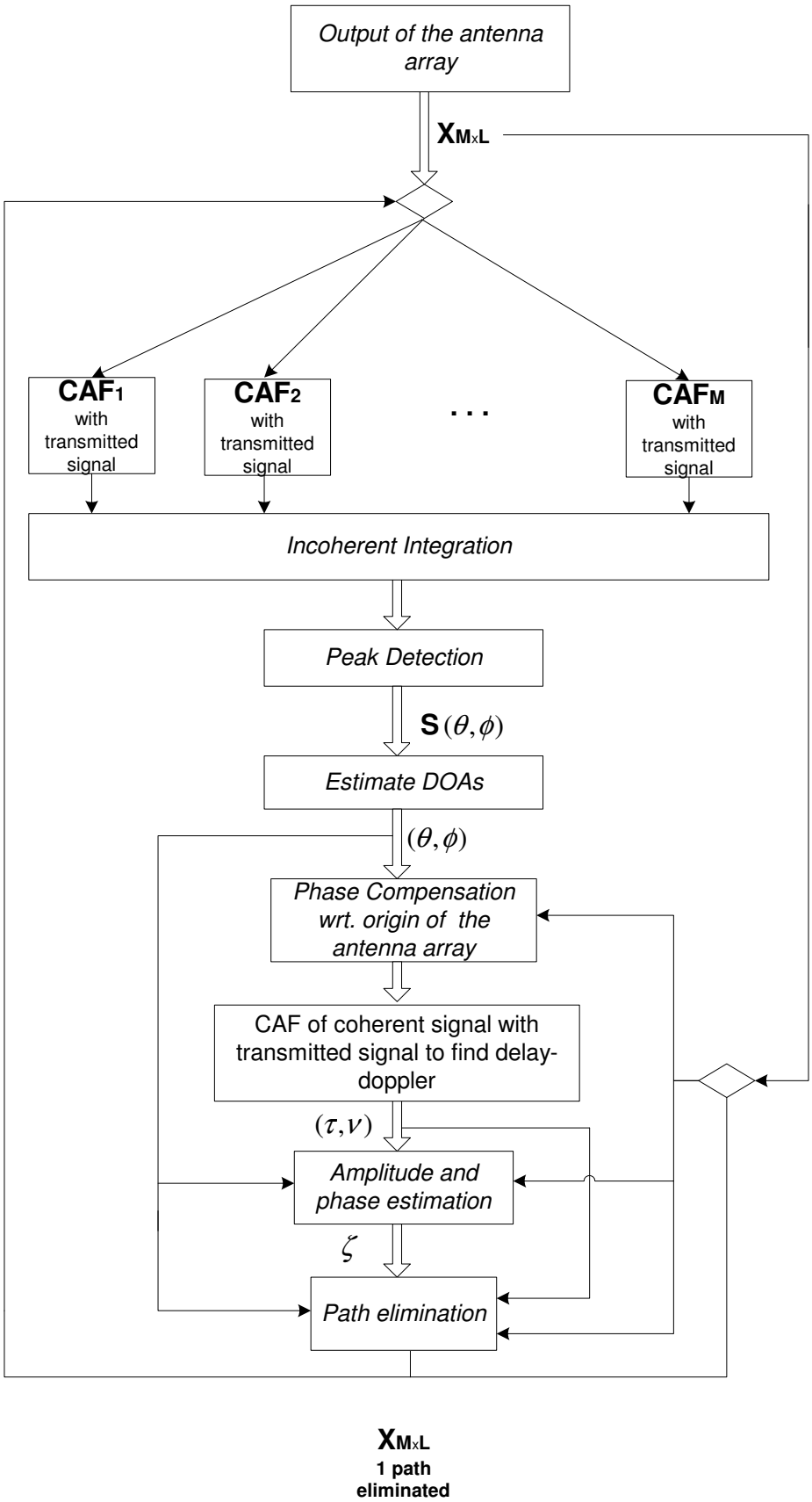

Figure 5.11: Proposed algorithm block diagram.

Chapter 6

COMPARISON OF THE PROPOSED METHOD WITH AN ALTERNATIVE MUSIC BASED APPROACH

Direction-of-arrival estimation plays an essential role in many signal processing applications and MUSIC is one of the most popular techniques for DOA estimation. In this chapter, a MUSIC-based approach estimating not only DOAs but delay and doppler of the impinging signal components is presented. Following the theory of the approach, simulation results and comparisons with the proposed CAF-DF technique are provided.

6.1 A MUSIC based delay-Doppler and DOA Estimation Technique

As stated in Chapter 3, MUSIC is a super-resolution algorithm which is based on the ensemble-averaged correlation matrix of the antenna array output. The MUSIC spectrum is computed by performing an eigen-value analysis on the correlation matrix. The space spanned by the eigenvectors consists of two disjoint subspaces: signal and noise subspaces. In terms of the orthogolonal characteristics of eigenvectors in the signal and noise subspaces, the MUSIC spectrum P, is given as:

$$P(\theta,\phi) = \frac{\mathbf{a}^H(\theta,\phi)\mathbf{a}(\theta,\phi)}{\mathbf{a}^H(\theta,\phi)\hat{\Pi}^{\perp}\mathbf{a}(\theta,\phi)} \tag{6.1}$$

where $\hat{\Pi}^{\perp}$ and $\mathbf{a}$ denote the eigenvectors corresponding to the noise space and the steering vector.

Having rementioned the basic logic behind the DOA estimation by MUSIC, lets now examine the sequential procedure of parameter estimation. First of all, each antenna output is correlated with a pulse duration of Barker-13 sequence as in Fig. 6.1. After that, correlated signal is used as an input for the Superposed Epoch Averaging (SEA) technique which is a statistical method used to resolve significant signal to noise ratio problems. Averaging procedure is demonsrated in Fig. 6.2 where C_m^n is a vector obtained by taking the n^{th} element of each pulse of the m^{th} antenna correlated output, prl is the pulse repetition length in samples, N represents number of pulses and κ is the output of the SEA. Formulation of the κ can be basically given as;

$$\kappa[n] = \frac{1}{M}\sum_{m=1}^{M} \|C_m^n\|^2 \quad . \tag{6.2}$$

Dominant peak points of the $\kappa[n]$ corresponds to probable signal arrival paths. By setting a threshold value, location of the dominant peaks are obtained. Time

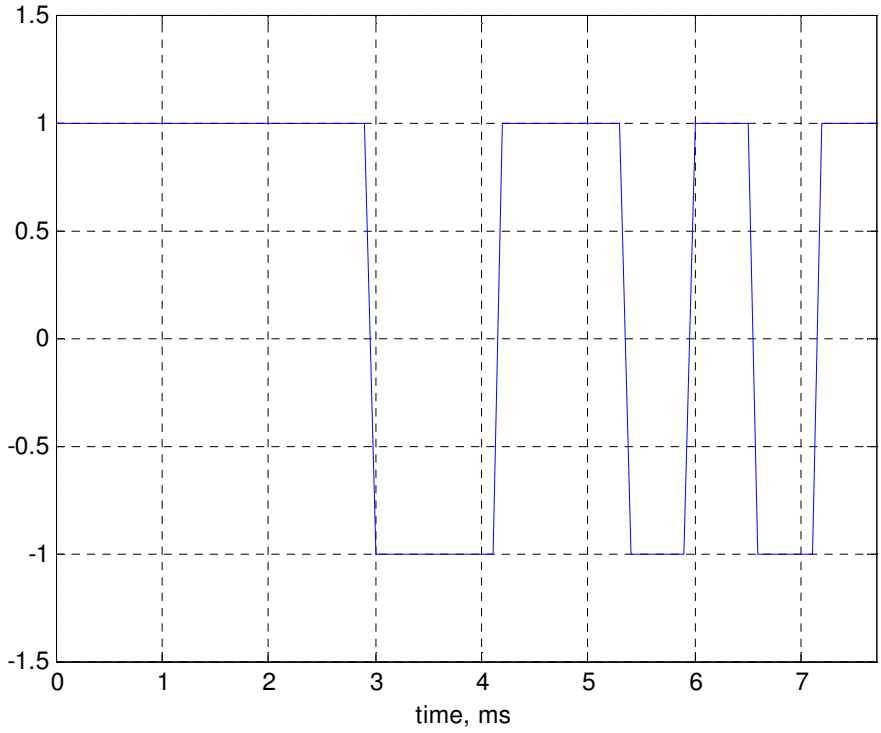

(a)

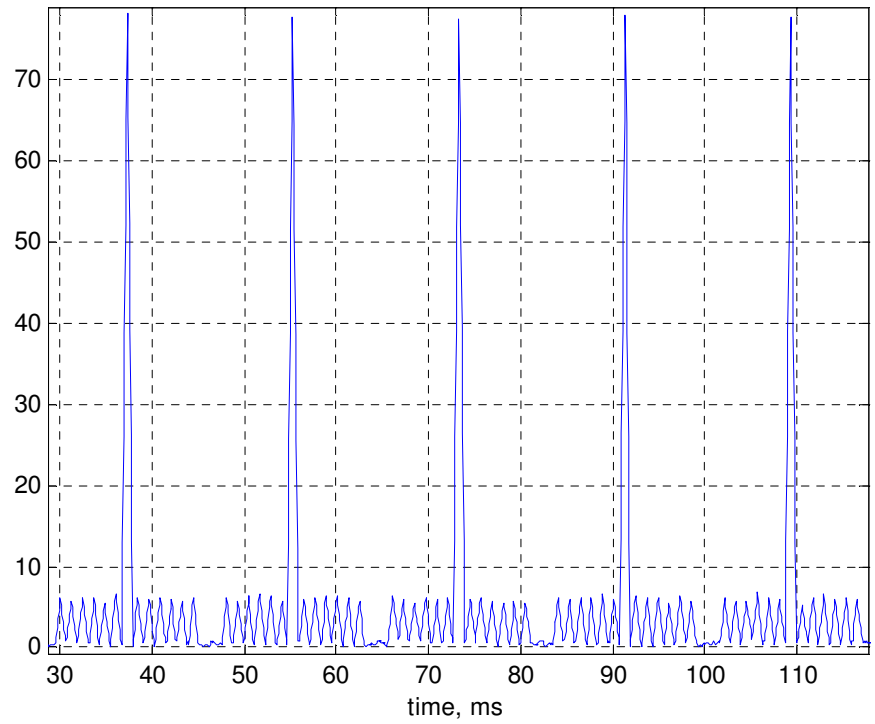

(b)

Figure 6.1: (a)Barker-13 sequence (b)One antenna output correlated with the Barker-13, a short segment.

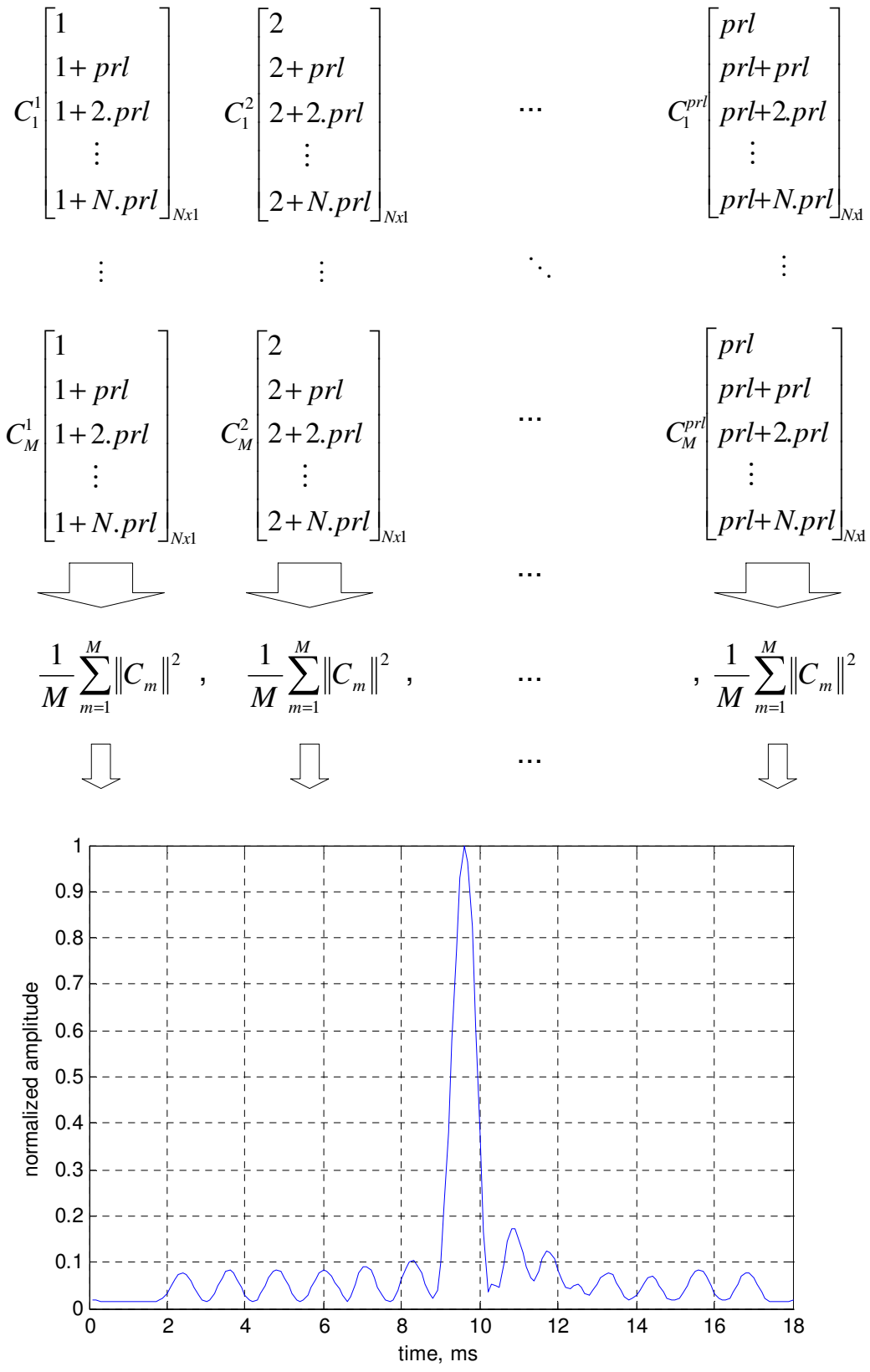

Figure 6.2: Averaging procedure and output($\kappa[n]$) .

domain pair of the indexes are the delay estimates of paths. For each peak, corresponding correlated antenna output vectors, $C_m^n \;\; m = 1, ..., M$, are merged to form an Mxprl matrix. Using this matrix as an input to the classical MUSIC algorithm, DOA of the each path can be found easily. As discussed in Chapter 5, in order to increase the SNR, with the estimated DOA each antenna correlated output is phase corrected with respect to the origin of the array and added up. Lastly, Fourier Transform of the resultant vector is evaluated to find the doppler shift on the arrival signal.

6.2 Simulation Results

In this section, performance of the proposed algorithm is tested by computer simulations and compared with a MUSIC-based technique using various scenarios. The simulation results in this chapter exhibit the characteristics of each method. A six-sensor circular array structure used in the simulations. The distance between the sensors is smaller than the half-wavelength of the signal. This ensures that there is no spatial aliasing.

We used sum of sinusoidal signals each of which is coded with a Barker-13 sequence. The reason for the use of Barker-13 was; real ionospheric echoes were coded like that, so for comparison reasons we preferred to use. Each received sequence from different signal paths consists of 111 Barker-13 coded pulses. Length of a pulse is $0.018\,s$ and total length of a signal is $\sim 2\,s$. The synthetic signal impinging on the m^{th} antenna, used in simulations is

$$s_m(t) = \sum_{i=1}^{d} b_{13}(t - \tau_{0,i}) e^{j(2\pi\nu_i t + \varphi_i)} e^{-j2\pi\nu_c \xi_{m,i}(\theta,\phi)} + n_{m,i}(t) \quad , \tag{6.3}$$

where $n_{m,i}(t)$ represents circularly symmetric gaussian noise, φ_i is a uniformly distributed random phase in $[0, 2\pi]$ and $b_{13}(t)$ represents the barker-13 coded sequence.

	Azimuth θ(deg)	Elevation ϕ(deg)	Delay τ(ms)	Doppler ν(Hz)
scenario-1	191.2	31.3	0.4	0.67
scenario-2	91.2	61.3	0.4	0.67

Table 6.1: Azimuth, Elevation, Delay and Doppler values of two different scenarios in case of 1 signal path. Computational delay and Doppler resolutions are 0.1 ms and 0.0023 Hz respectively.

Firstly, performances are compared when there exists only one signal path arriving at the array. Secondly, in the case of two signal paths, in addition to the root mean squared error (rMSE) performances, ability of the algorithms in path separation is discussed. In both used techniques, delay and Doppler computation resolution is 0.1 ms and 0.0023 Hz respectively. Two scenarios with different parameters for one signal source case are tabulated in Table 6.1. The rMSE of the DOAs, time-delay and Doppler estimates are calculated for each of the algorithms based on 200 Monte Carlo trials for various SNR values and presented in the Figs. 6.3-4. As observed from the simulation results of one signal source case, especially at low SNR, CAF-DF performs significantly better than the MUSIC.

Having discussed the performances of two algorithms for one signal source case, we will now focus on when there exist two closely spaced signals impinging on the antenna array. In Table 6.2, some scenarios are listed. Firstly lets observe the ability of algorithms in separating two signal paths in (θ, ϕ) space having the parameters as in scenario-3. In this situation, it is clearly seen from the Fig. 6.5 and Fig. 6.6 that the MUSIC-based technique cannot separate two signal paths. This crucial difference is also illustrated for various SNR values in Fig. 6.7. In scenario-4, for two paths have nearly same Doppler shift and differ in time-delay, CAF-DF has slightly better performance at low SNR values due to processing delay and Doppler information simultaneously Fig. 6.8. Oppositely, scenario-5 consists of two paths delayed by same amount but separated in Doppler significantly. Now MUSIC-based technique shows poorer performance than the previous case due to being unable to process Doppler difference information Fig.

	Azimuth θ(deg)	Elevation ϕ(deg)	Delay τ(ms)	Doppler ν(Hz)
scenario-3	191.2 ; 189.1	36.3 ; 38.2	0.4 ; 0.6	0.31 ; 0.93
scenario-4	191.2 ; 189.1	36.3 ; 38.2	0.3 ; 1.3	0.70 ; 0.701
scenario-5	191.2 ; 189.1	36.3 ; 38.2	0.6 ; 0.6	0.31 ; 0.93
scenario-6	189.1 ; 189.1	33.2 ; 41.2	0.4 ; 0.7	0.31 ; 0.93

Table 6.2: Azimuth, Elevation, Delay and Doppler values of four different scenarios in case of 2 signal paths. Computational delay and Doppler resolutions are 0.1 ms and 0.0023 Hz respectively.

6.9. Since MUSIC-based technique makes use of the matched filter output, when two signals arrive with very close delay to each other, it will be impossible to separate them without using any other data processing. Lastly, in scenario-6, we examine an important case, which is widely encountered in real HF experiments, where arrival azimuth angles are nearly same but elevation angles differ. Results in Fig. 6.10, shows that CAF-DF is able to separate the two paths and has significantly better delay and Doppler shift estimates for a wide range of SNR values than the MUSIC-based technique.

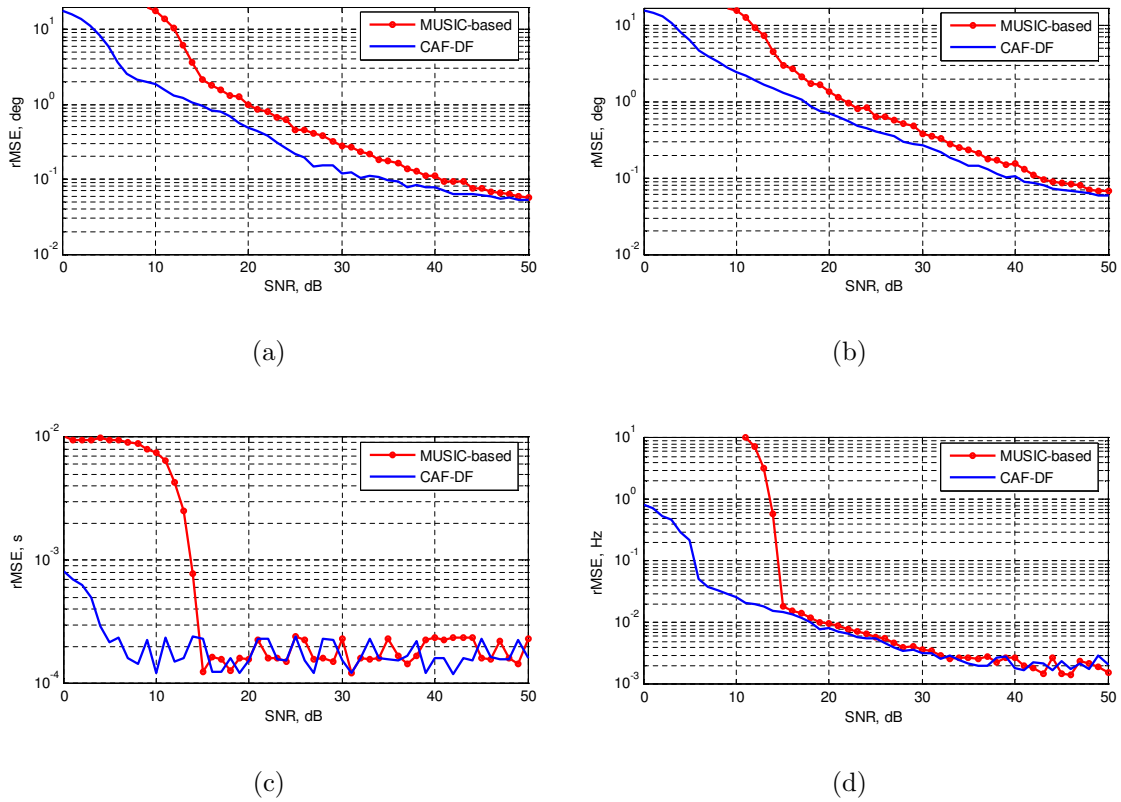

Figure 6.3: rMSE of the proposed estimators as a function of the SNR for Scenario-1. (a)Azimuth θ. (b)Elevation ϕ. (c)Time-delay τ. (d)Doppler shift ν shift.

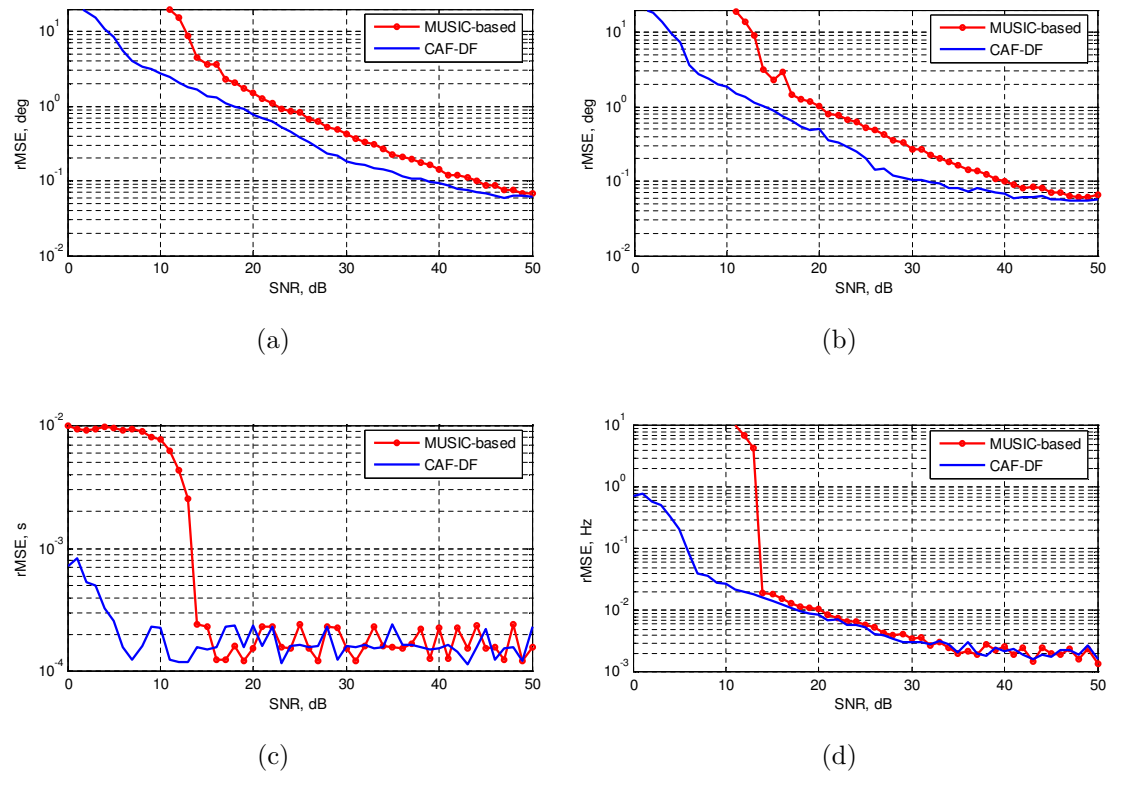

Figure 6.4: rMSE of the proposed estimators as a function of the SNR for Scenario-2. (a)Azimuth θ. (b)Elevation ϕ. (c)Time-delay τ. (d)Doppler ν shift.

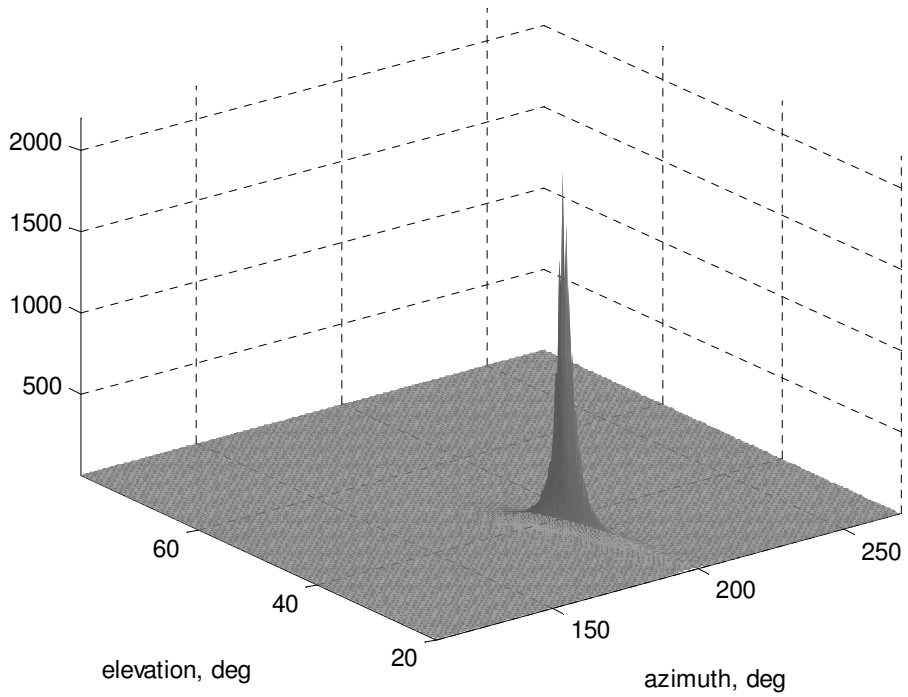

(a)

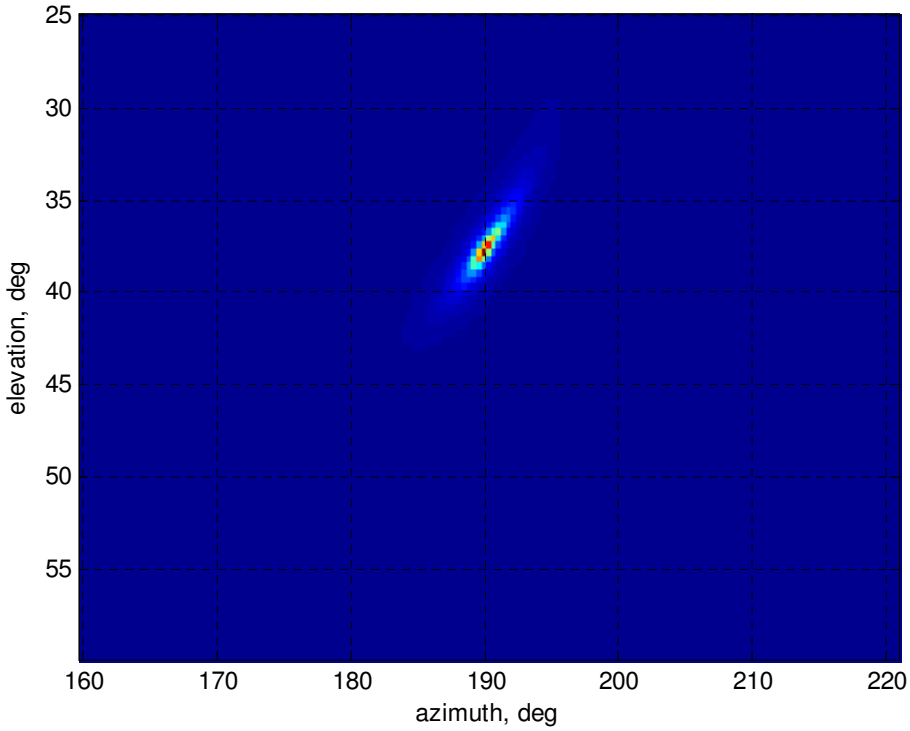

(b)

Figure 6.5: (a) 3-D and (b) 2-D spatial spectra of MUSIC algorithm.

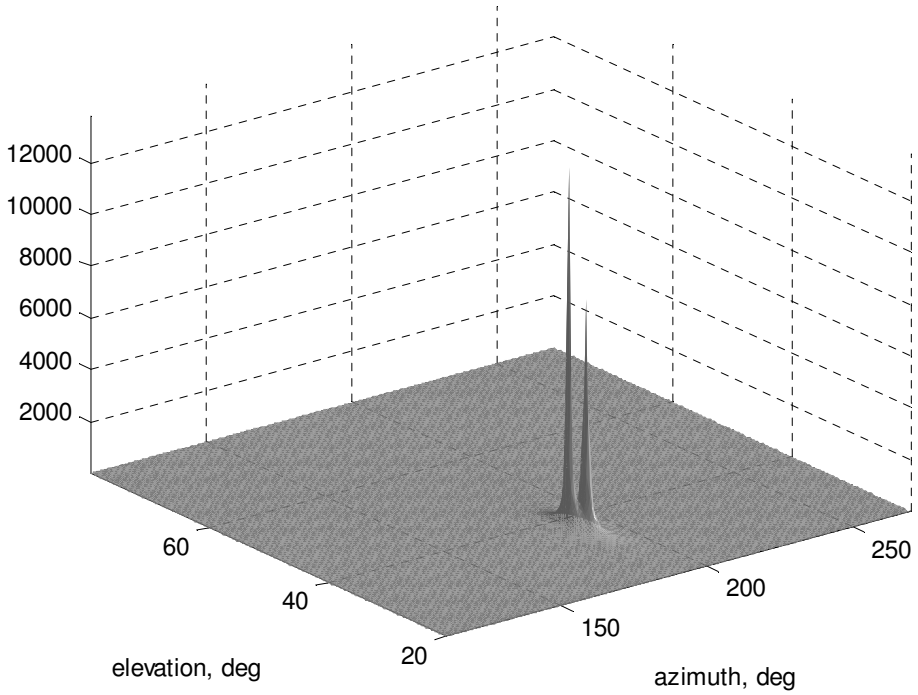

(a)

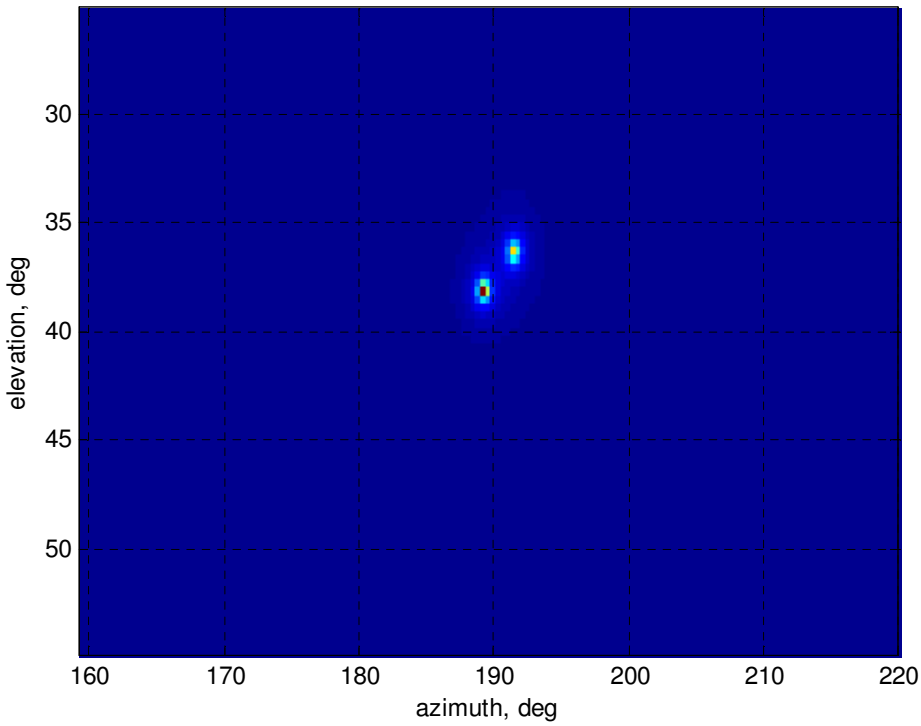

(b)

Figure 6.6: (a) 3-D and (b) 2-D spatial spectra of CAF-DF.

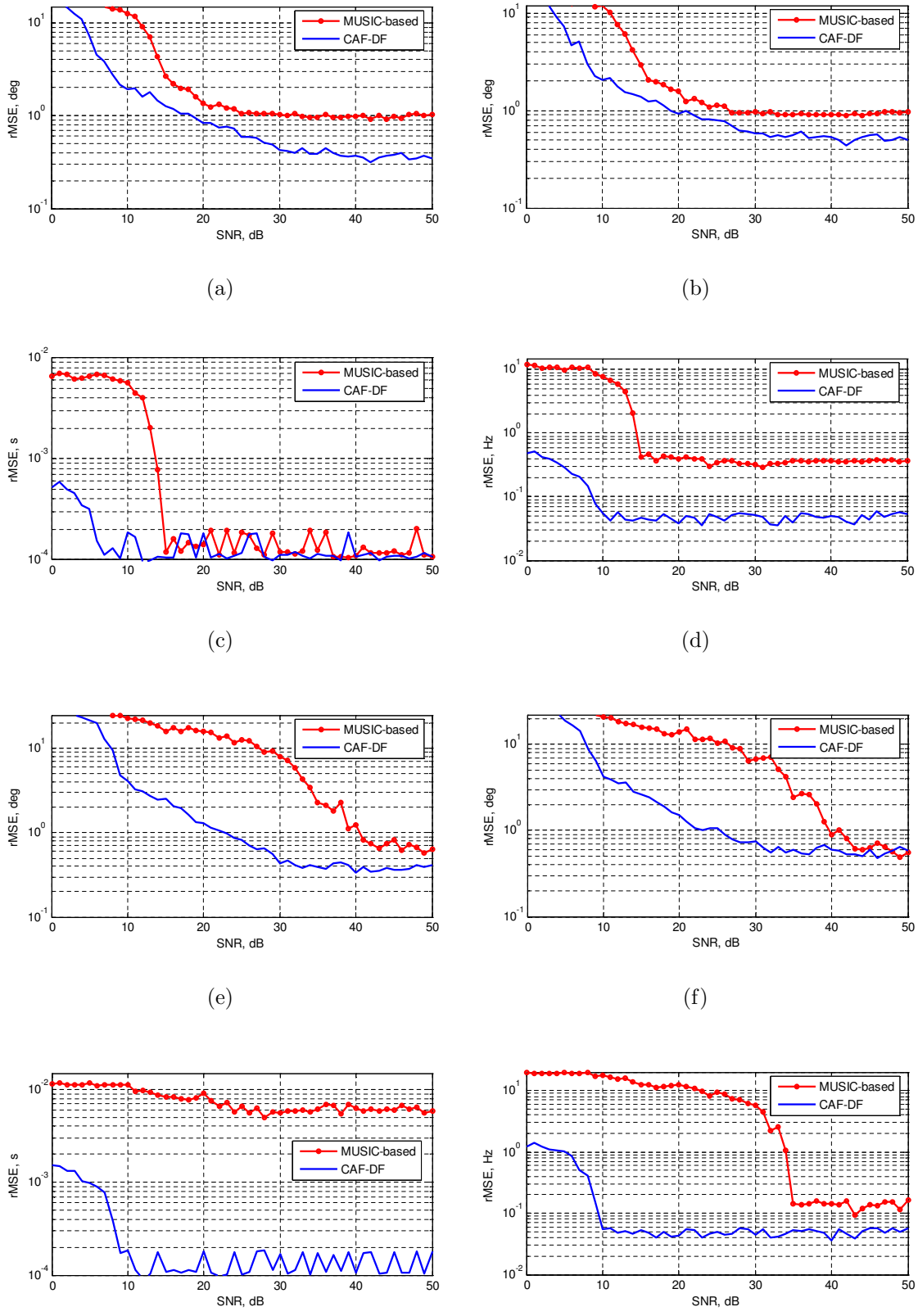

Figure 6.7: rMSE of the proposed estimators as a function of the SNR for Scenario-3. (a)Azimuth θ_1. (b)Elevation ϕ_1. (c)Time-delay τ_1. (d)Doppler shift ν_1. (e)Azimuth θ_2. (f)Elevation ϕ_2. (g)Time-delay τ_2. (h)Doppler shift ν_2. shift.

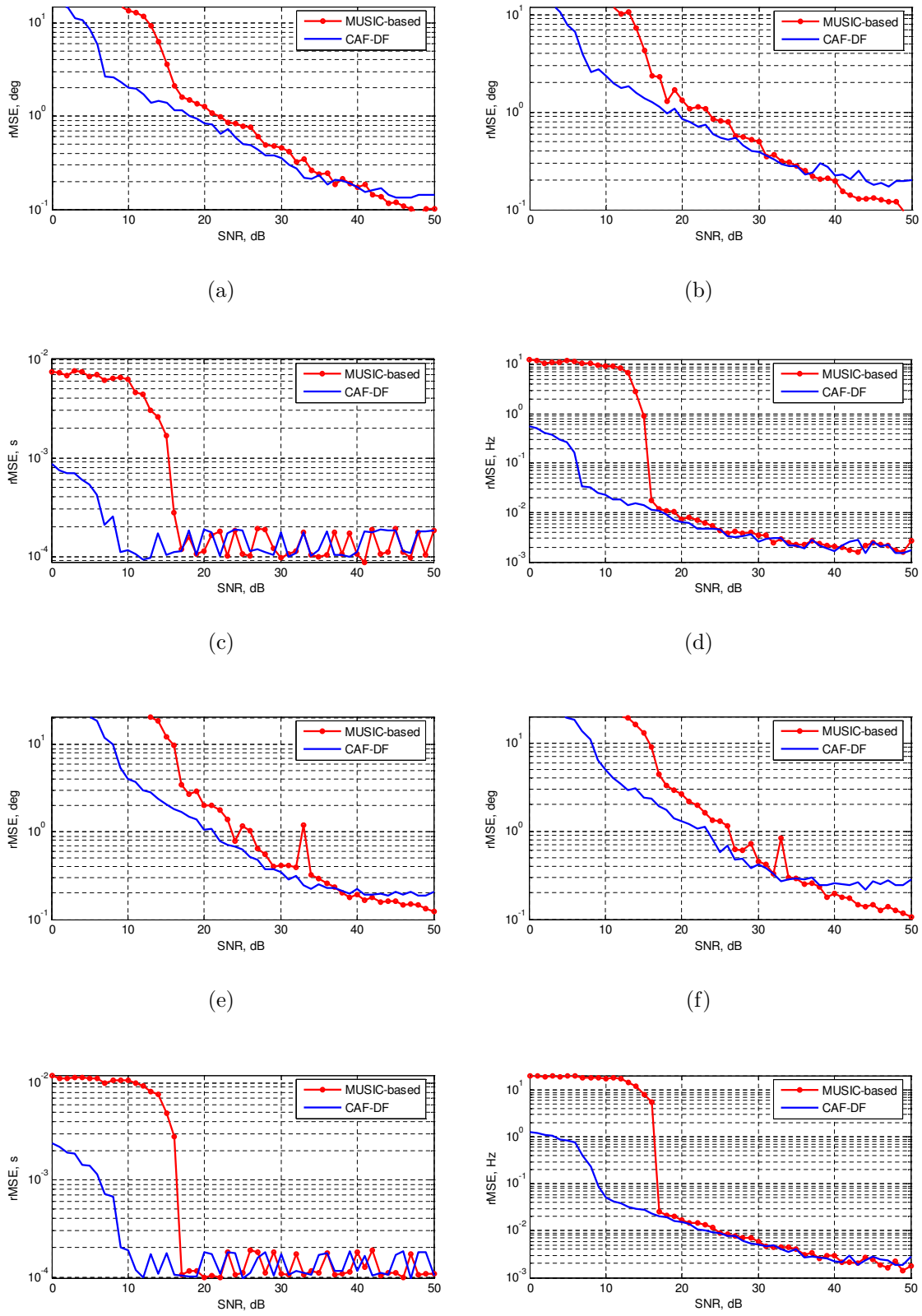

Figure 6.8: rMSE of the proposed estimators as a function of the SNR for Scenario-4. (a)Azimuth θ_1. (b)Elevation ϕ_1. (c)Time-delay τ_1. (d)Doppler shift ν_1. (e)Azimuth θ_2. (f)Elevation ϕ_2. (g)Time-delay τ_2. (h)Doppler shift ν_2. shift.

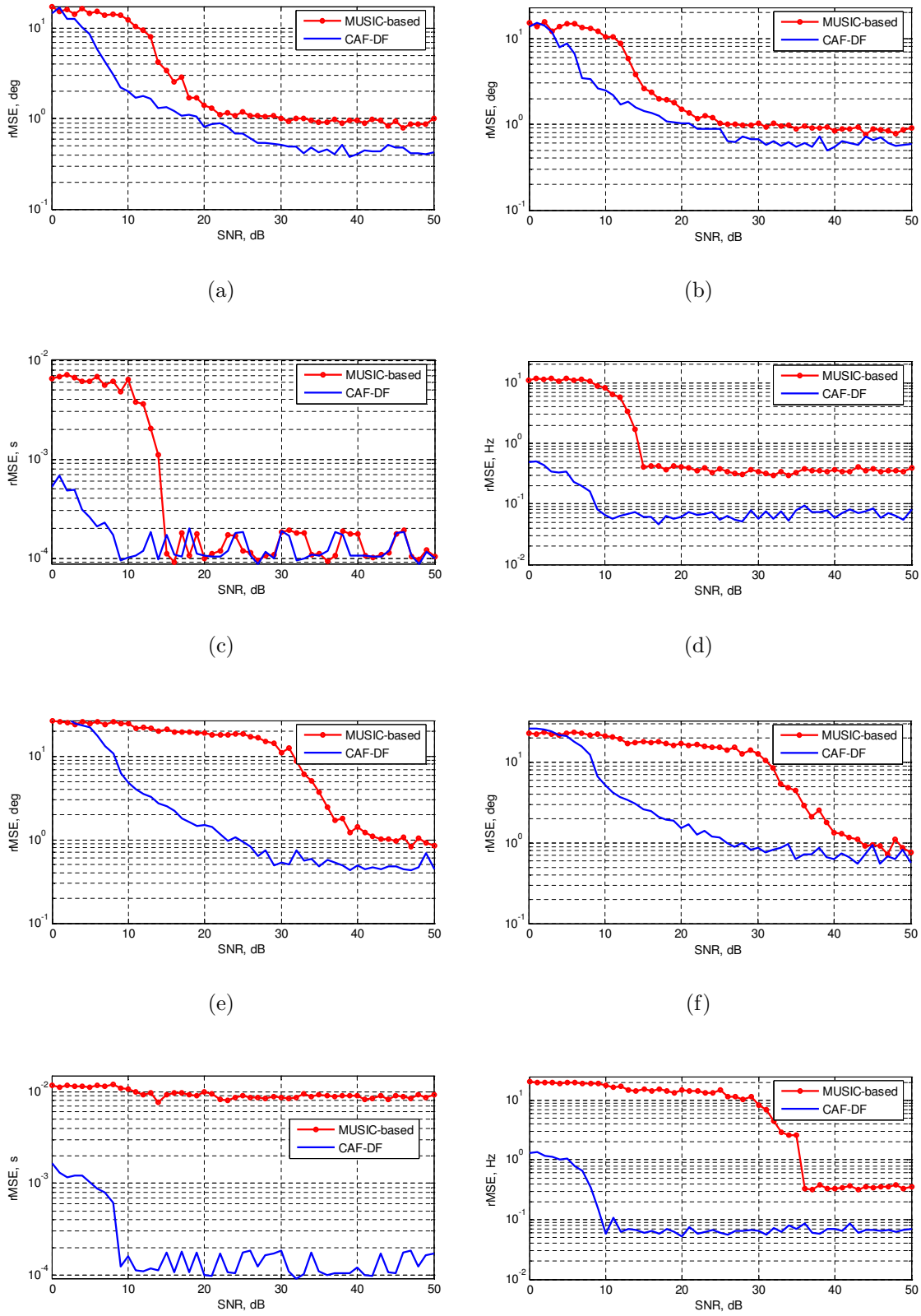

Figure 6.9: rMSE of the proposed estimators as a function of the SNR for Scenario-5. (a)Azimuth θ_1. (b)Elevation ϕ_1. (c)Time-delay τ_1. (d)Doppler shift ν_1. (e)Azimuth θ_2. (f)Elevation ϕ_2. (g)Time-delay τ_2. (h)Doppler shift ν_2. shift.

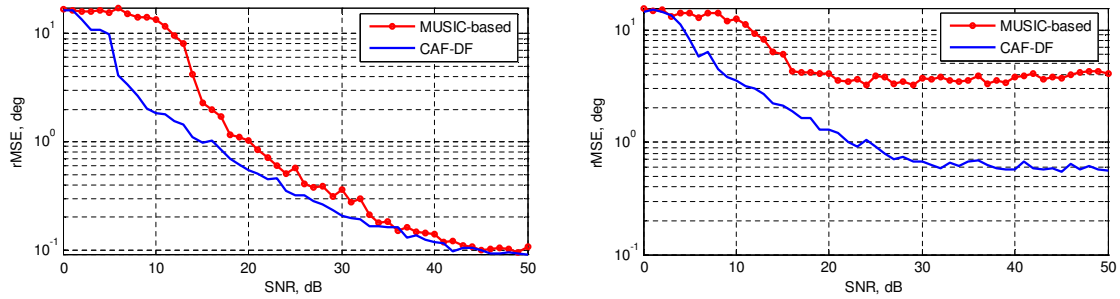

(a)

(b)

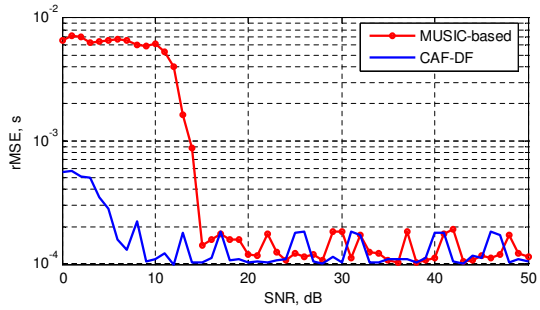

(c)

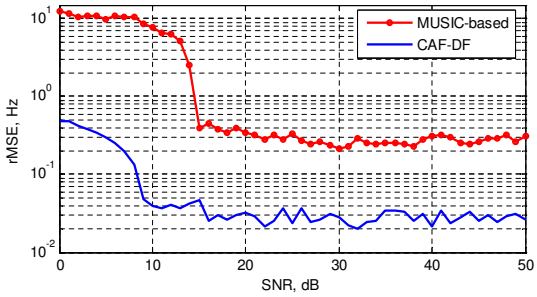

(d)

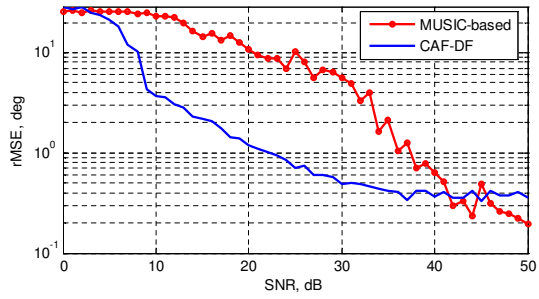

(e)

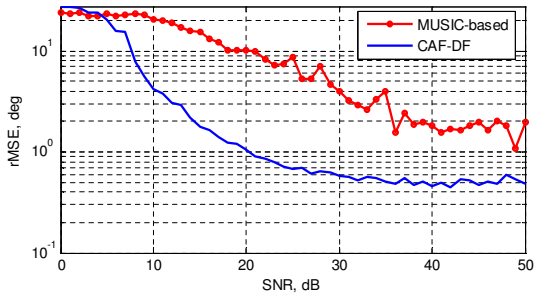

(f)

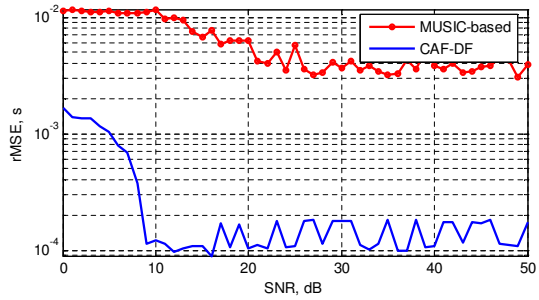

(g)

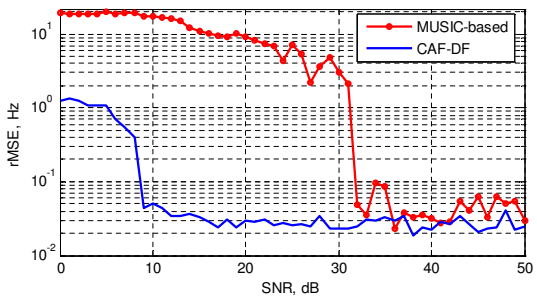

(h)

Figure 6.10: rMSE of the proposed estimators as a function of the SNR for Scenario-6. (a)Azimuth θ_1. (b)Elevation ϕ_1. (c)Time-delay τ_1. (d)Doppler shift ν_1. (e)Azimuth θ_2. (f)Elevation ϕ_2. (g)Time-delay τ_2. (h)Doppler shift ν_2. shift.

Chapter 7

A CASE STUDY: HIGH-LATITUDE HF COMMUNICATION

Performances and results of the proposed CAF-DF and MUSIC-based techniques on real ionospheric signals recorded by the University of Leister, Electrical and Electronics Department will be presented. In this chapter, following a brief description of the experimental system, comparison of the technique will be presented.

7.1 System Description

The signals processed in the simulations were radiated by a DAMSON (Doppler and Multipath SOunding Network) transmitter which is the result of a collaboration between the UK Defence Evaluation and Research Agency, the Canadian

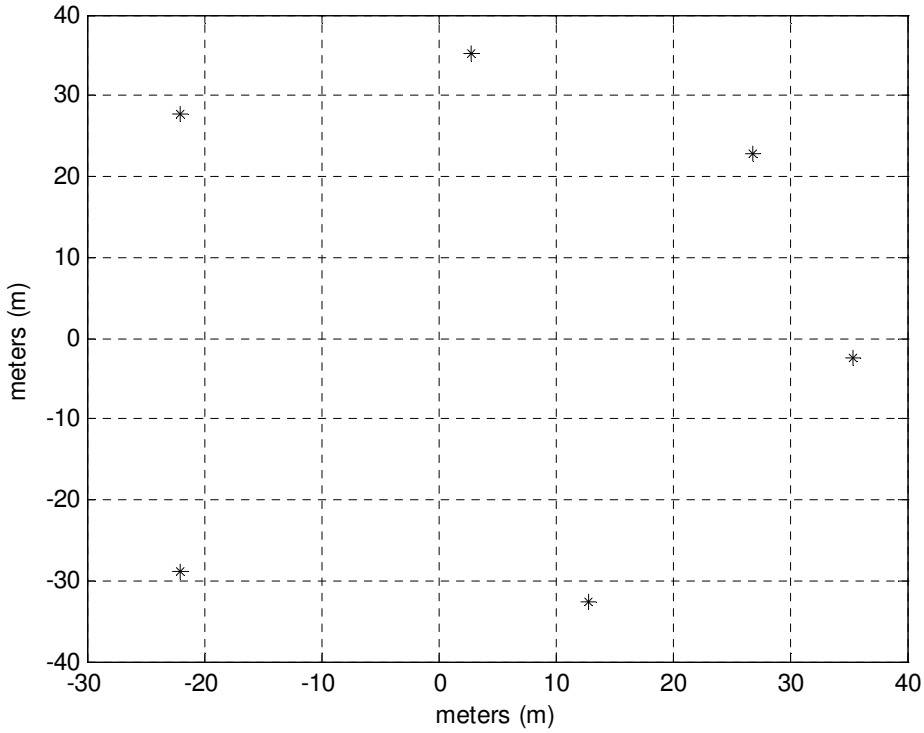

Figure 7.1: Relative positions of the antennas in the receiving array at Kiruna.

Communications Research Center, the Norwegian Defence Research Establishment and the Swedish Defence Research Establishment. This system characterizes the propagation path using a number of sounding signals which can be freely scheduled [41].

The signals were received on a six-element antenna array with a circular arrangement as in the Fig.7.1. However, due some calibration problems, we discarded the third antenna and used the remaining five antennas. The individual elements of which were connected, via a calibration switch, to individual inputs of a multi-channel receiver [42]. The radiated signals consists of Barker-13 coded BPSK pulses modulated at 1667 baud with a repetition rate of 55 coded pulses per second. The total length of the sequence is $\sim 2s$ and a short time segment of the absolute value of the received signal at the output of an antenna element is given in Fig. 7.2. In both used techniques, delay and Doppler resolution is 0.1 ms and 0.0023 Hz respectively. Measurements that we used in the simulations, were made over Uppsala-Kiruna path highlighted with a red line in Fig.7.3.

Figure 7.2: A short time segment of the actual signal at the output of an antenna element.

Figure 7.3: Map showing the path from Uppsala to Kiruna.

7.2 Simulation Results

In this section, two multipath signal sets will be examined using the proposed CAF-DF technique and MUSIC-based technique. Steps in the estimation of parameters corresponding to each signal path will be presented with related plots. Two sets of data will be used namely dataset1 and dataset2.

As previously mentioned, firstly CAF with the transmitted signal is calculated at each antenna and then these resultant CAFs are incoherently integrated as in Fig. 7.4. It is seen from the resultant normalized CAF surface that the noise level is suppressed relative to the peak when compared to the individual CAF surfaces. Then, we make a search in the $(\hat{\theta}, \hat{\phi})$ space and choose an azimuth and elevation pair, which satisfies the criteria in Eqn. (5.42). Once $\hat{\theta}_p$ and $\hat{\phi}_p$ estimates are obtained, we modify the array outputs for a coherent integration as seen in Fig. 7.5 . With correct DOAs, we have overlapped sensor outputs. Then, CAF of the SNR improved signal is calculated in order to estimate delay and Doppler shift accurately in Fig. 7.6. Observe that the CAF of the coherent integrated data is sharper than the previous CAFs. Using the four estimated parameters, a copy of the impinging signal at each antenna is created. In Fig. 7.7, three antenna outputs and copy of the strongest path at these antennas is seen. In this figure, we omitted to plot other two antennas for a clear appearance. Having determined the copy of the strongest signal path at each antenna output, we eliminate it by simply subtracting its respective copy from each antenna output in order to start our search procedure for other signal paths.

Estimation results obtained by CAF-DF and MUSIC-based techniques for dataset-1 are tabulated in Table 7.1 and 7.2. Based on the locations of HF transmitter and receiver on the map in Fig. 7.3, both CAF-DF and MUSIC-based techniques provide very reasonable azimuth estimates. However, they differ in elevation estimates. By making use of the Doppler shift difference between

dataset1	Azimuth(deg)	Elevation(deg)	Delay(ms)	Doppler(Hz)
1.Path	197.30	31.87	9.4	-0.5912
2.Path	198.48	54.79	11.5	-0.9417
3.Path	200.55	22.86	11.5	-0.5125

Table 7.1: Azimuth, elevation, delay and Doppler estimates of CAF-DF for 3 signal paths. Computational delay and Doppler resolutions are 0.1 ms and 0.0023 Hz respectively.

dataset1	Azimuth(deg)	Elevation(deg)	Delay(ms)	Doppler(Hz)
1.Path	197.12	31.80	9.4	-0.5914
2.Path	198.41	57.49	11.5	-0.9586
3.Path	197.67	32.91	10.7	-0.5966

Table 7.2: Azimuth, elevation, delay and Doppler estimates of MUSIC for 3 signal paths. Computational delay and Doppler resolutions are 0.1 ms and 0.0023 Hz respectively.

dataset2	Azimuth(deg)	Elevation(deg)	Delay(ms)	Doppler(Hz)
1.Path	195.82	31.73	9.4	-0.5078
2.Path	194.49	39.56	11.5	-0.5388
3.Path	197.74	18.42	8.7	-0.4291

Table 7.3: Azimuth, elevation, delay and Doppler estimates of CAF-DF for 3 signal paths. Computational delay and Doppler resolutions are 0.1 ms and 0.0023 Hz respectively.

dataset2	Azimuth(deg)	Elevation(deg)	Delay(ms)	Doppler(Hz)
1.Path	195.45	29.58	9.4	-0.5080
2.Path	195.64	31.43	8.1	-0.5042
3.Path	195.64	33.46	10.7	-0.5195

Table 7.4: Azimuth, elevation, delay and Doppler estimates of MUSIC for 3 signal paths. Computational delay and Doppler resolutions are 0.1 ms and 0.0023 Hz respectively.

second and third path, CAF-DF resolves the third path which is at the same delay with the second one. Same procedure is applied to dataset2 and plots are given in Figs. 7.15-7.24. Estimation results of each technique are tabulated in Table 7.3 and 7.4. Again, all estimated azimuth values are in the expected angle range for each signal path. Now the Doppler shifts corresponding to each path are very close to each other with separated delays. MUSIC-based technique elevation angle estimates are nearly same meaning that they are not resolved. However, by making use of the delay difference between signal paths, CAF-DF finds three distinct paths.

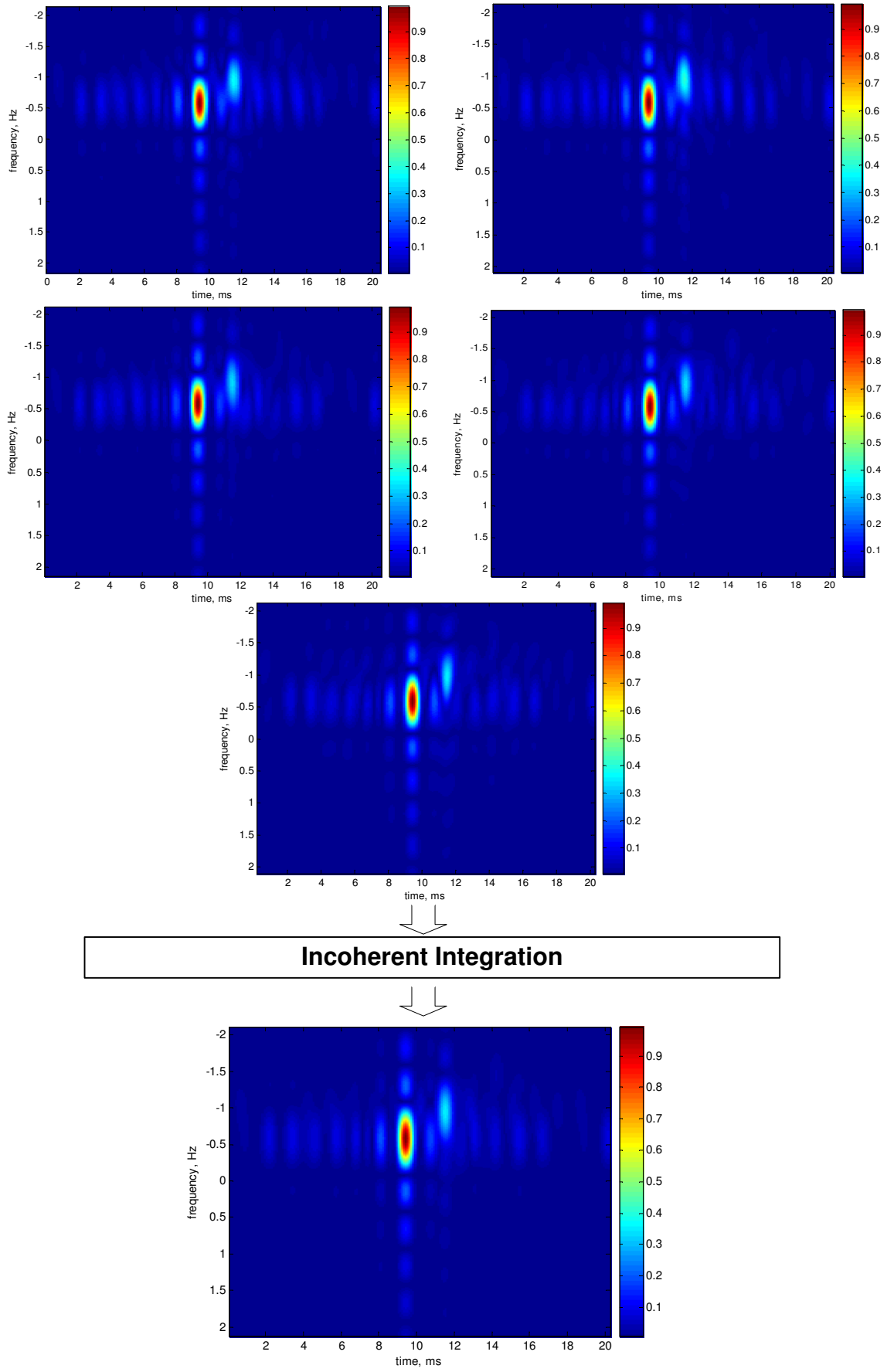

Figure 7.4: Incoherent integration of the CAF surfaces for the strongest path.

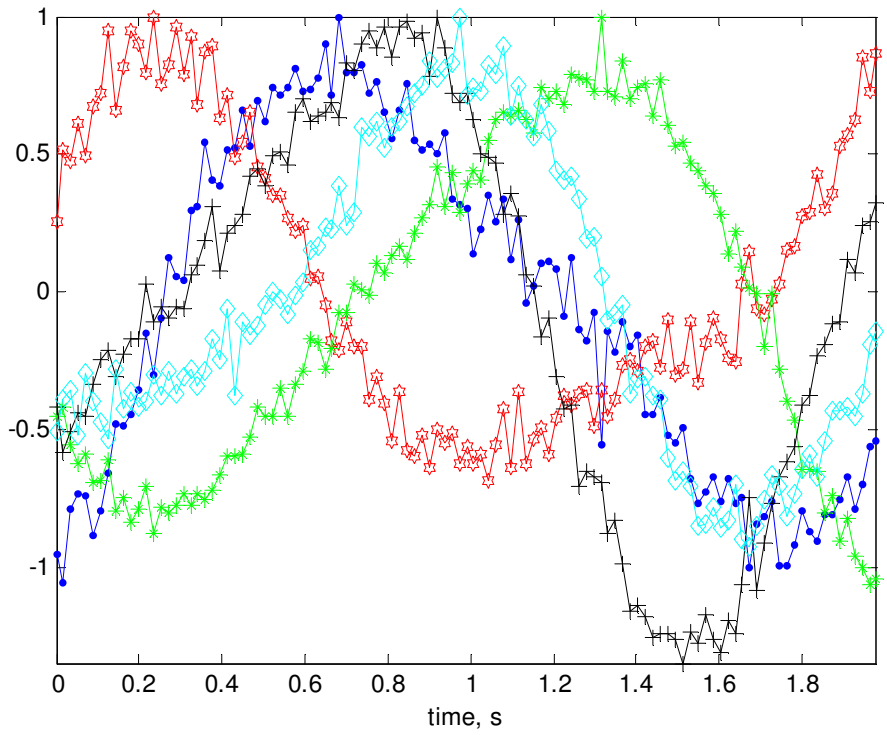

(a)

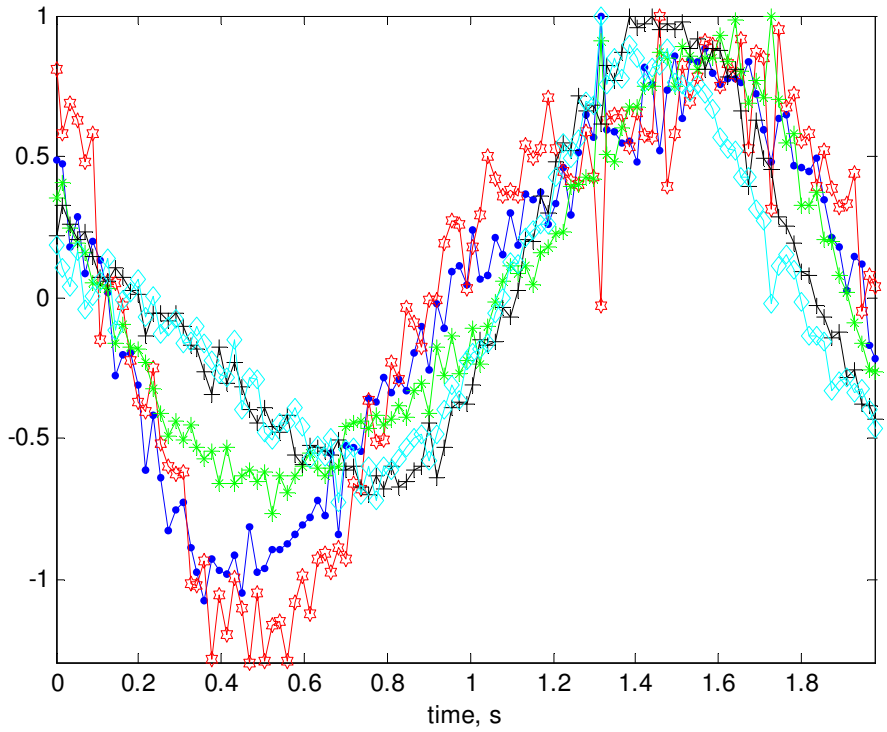

(b)

Figure 7.5: Slow-time representation of the 5-element array output. All signal amplitudes are normalized to 1. (a)before phase compensation (b)after phase compensation with the first DOA estimate.

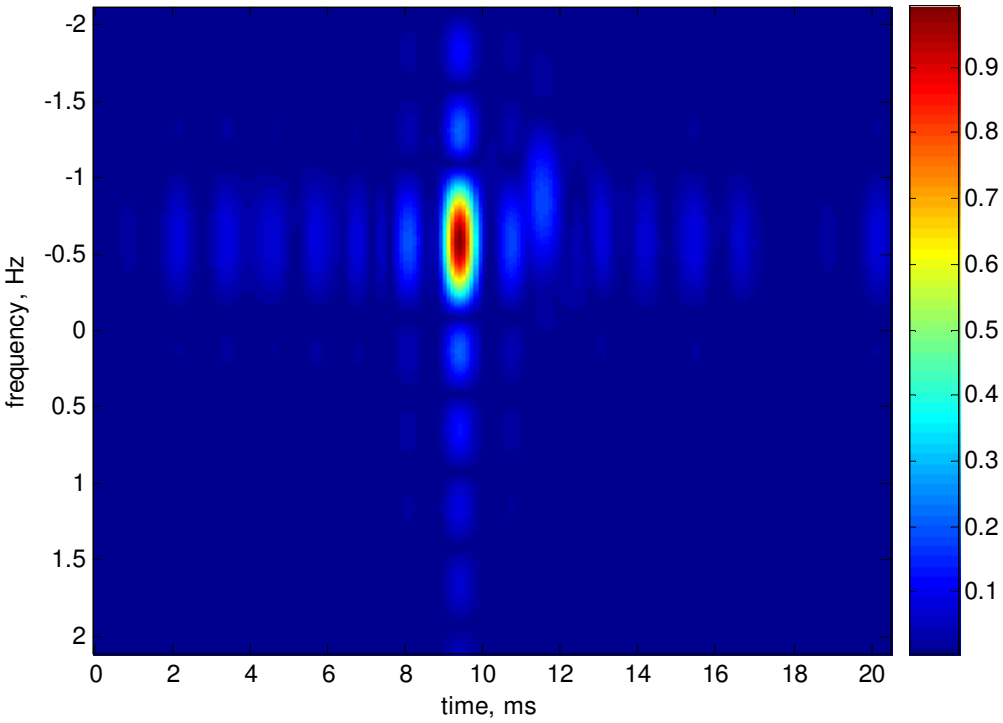

Figure 7.6: Coherently integrated CAFs for the strongest path.

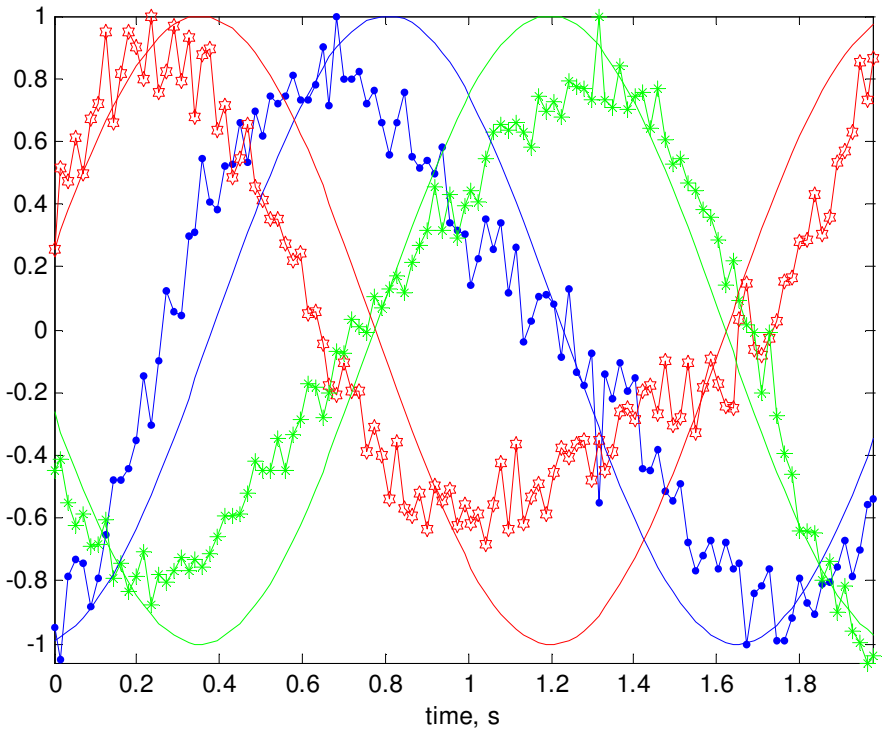

Figure 7.7: Synthetically generated copy of the strongest path at three antenna output with original slow-time data. Marked lines represent the real data and smooth lines for synthetic copy signal. All signal amplitudes are normalized to 1.

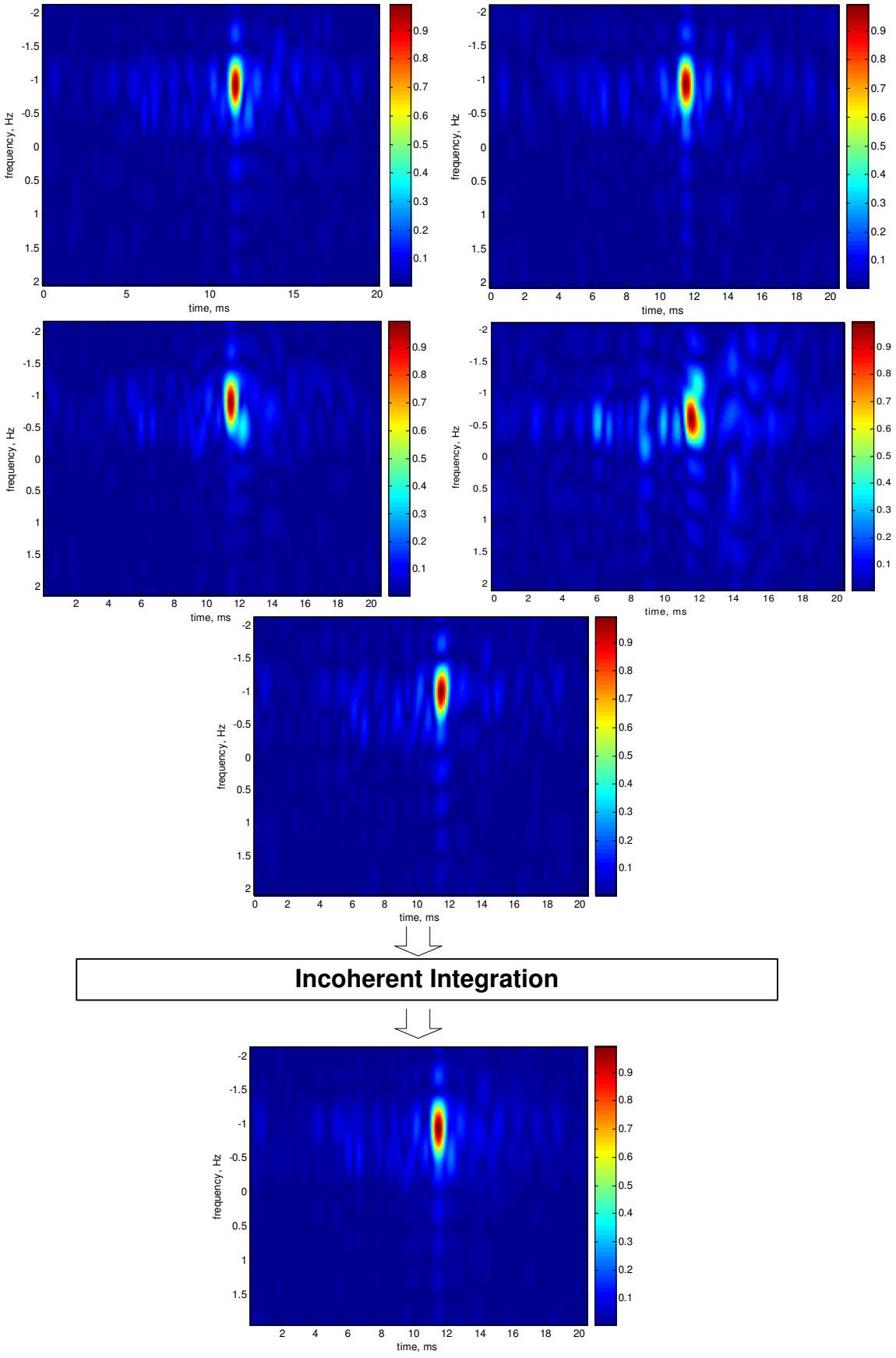

Figure 7.8: Incoherent integration of the CAF surfaces for the second path.

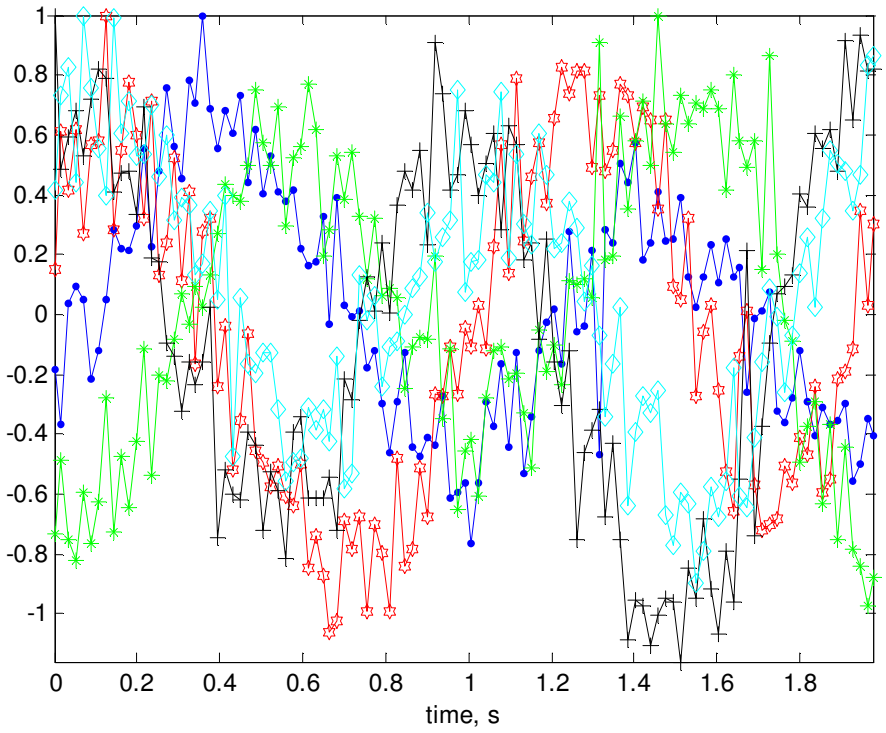

(a)

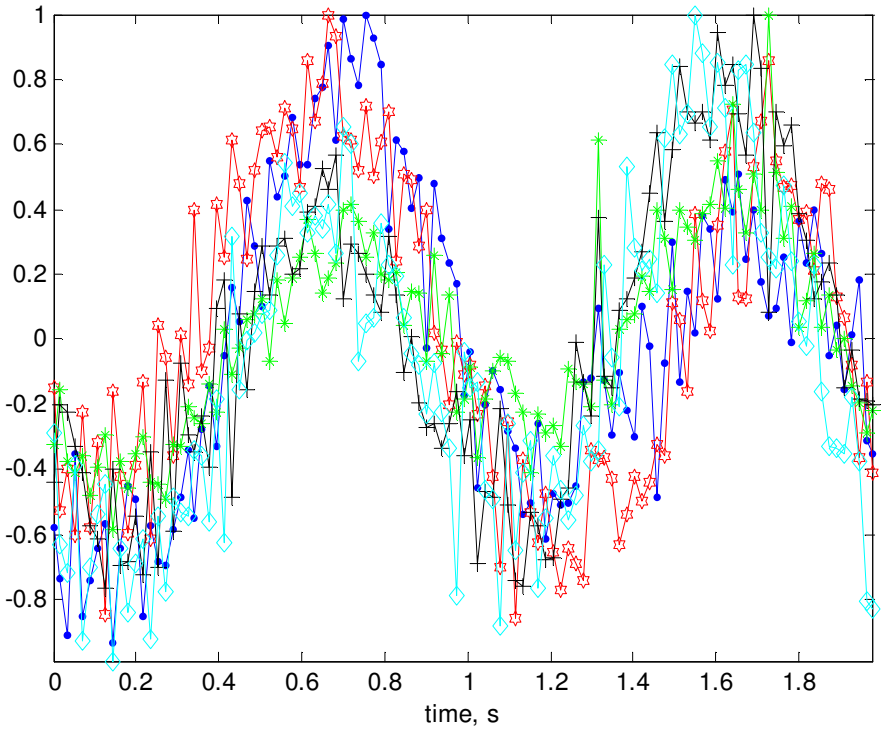

(b)

Figure 7.9: Strongest path eliminated slow-time representation of the 5-element array output. All signal amplitudes are normalized to 1. (a)before phase compensation (b)after phase compensation with the first DOA estimate

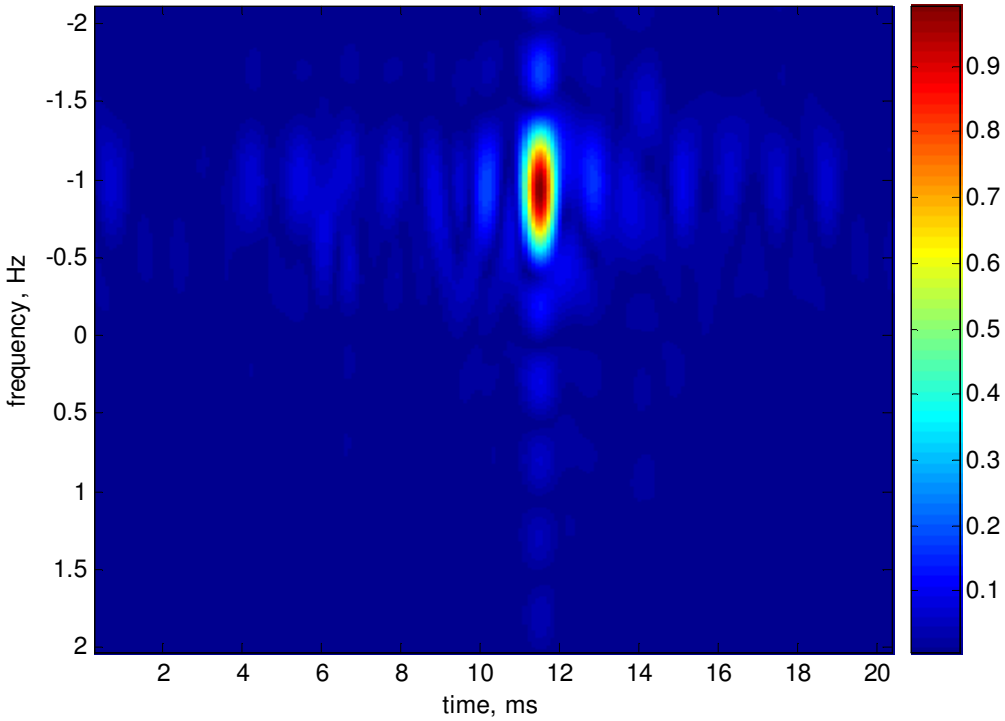

Figure 7.10: Coherently integrated CAFs for the second path.

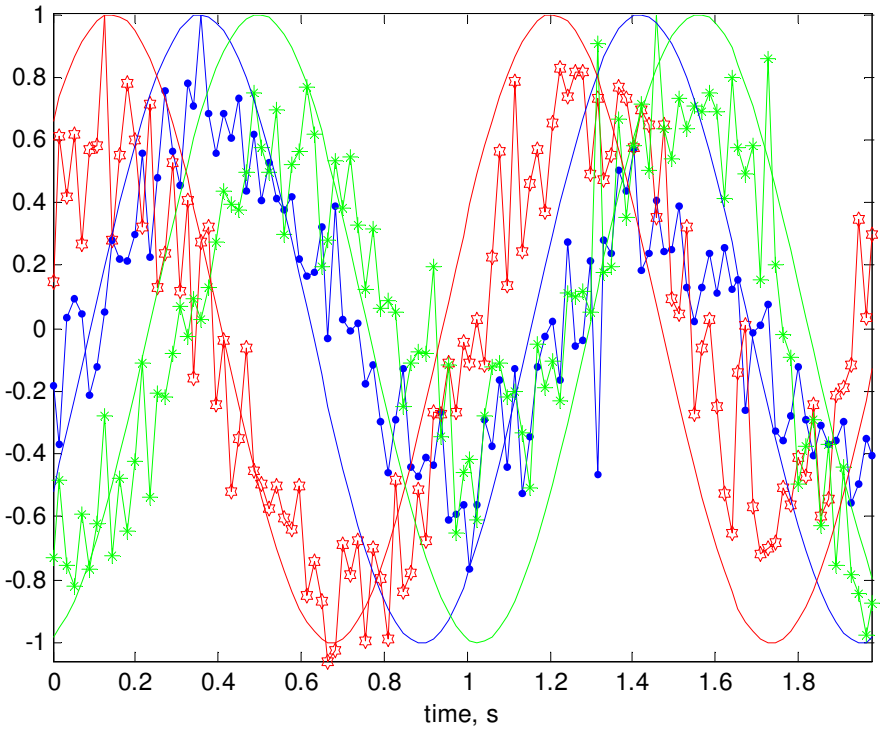

Figure 7.11: Synthetically generated copy of the second path at three antenna output with original slow-time data. Marked lines represent the real data and smooth lines for synthetic copy signal. All signal amplitudes are normalized to 1.

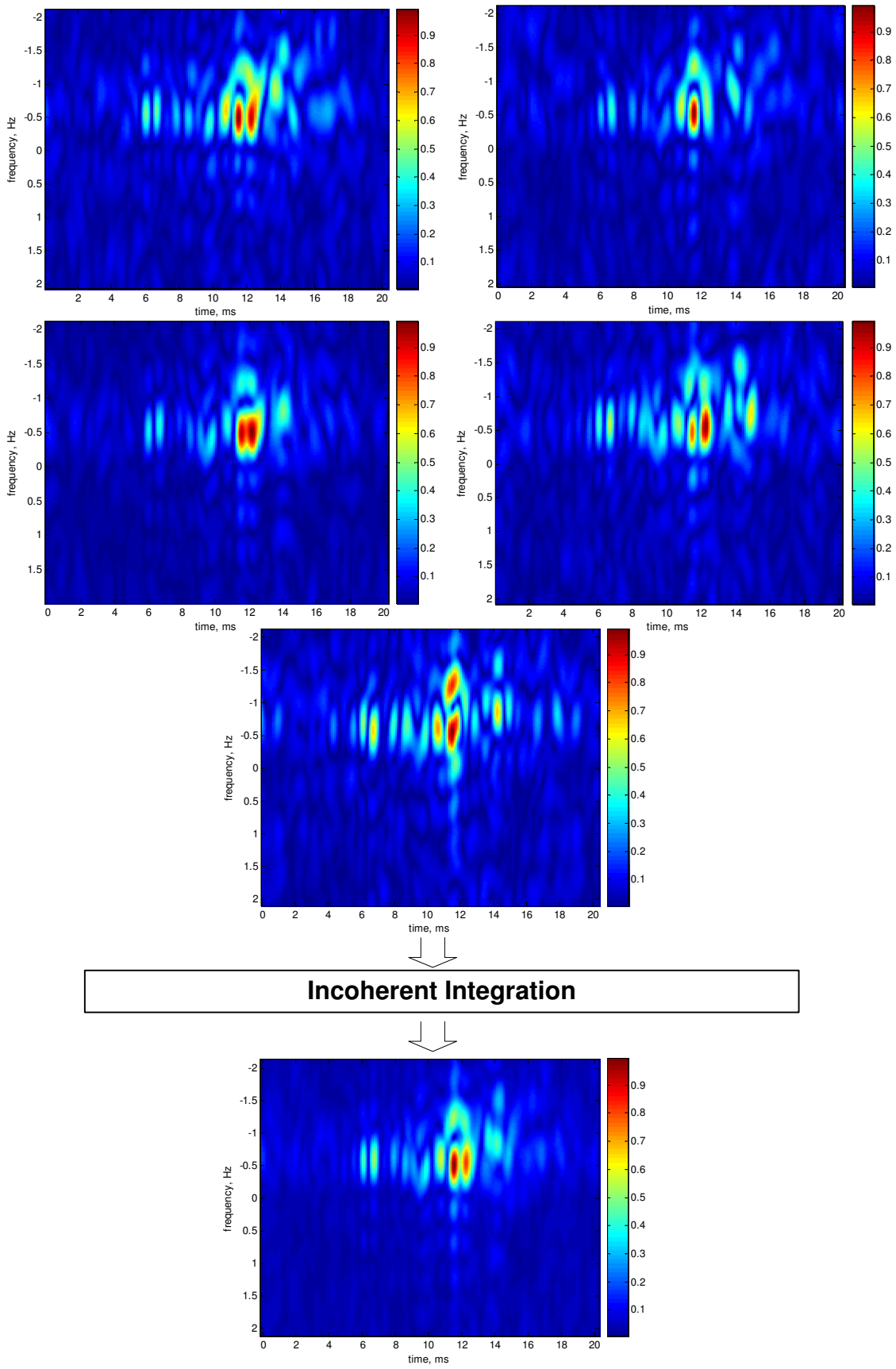

Figure 7.12: Incoherent integration of the CAF surfaces for the third path.

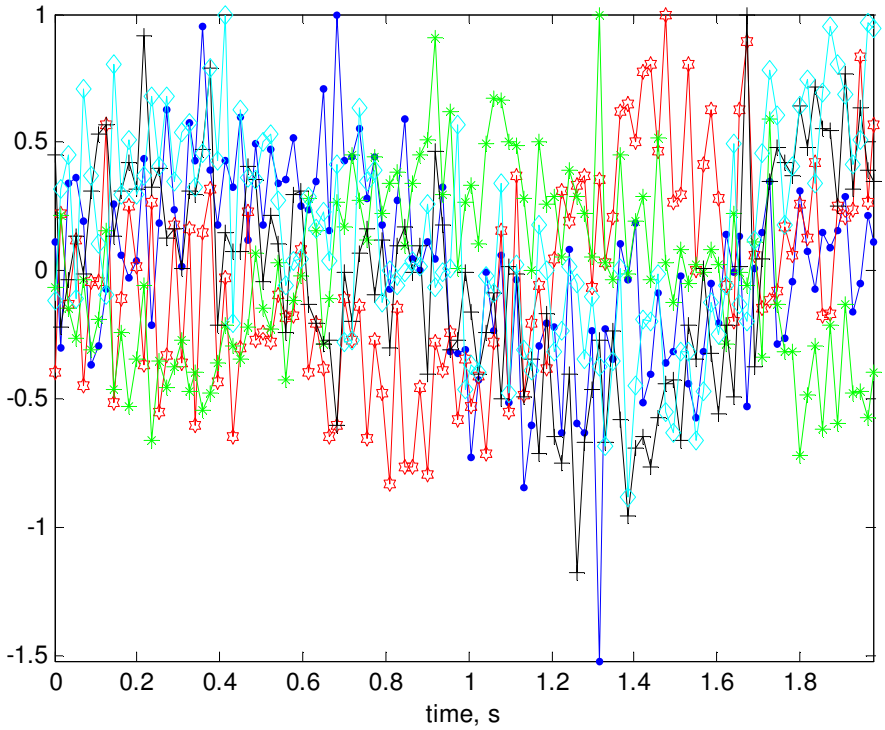

(a)

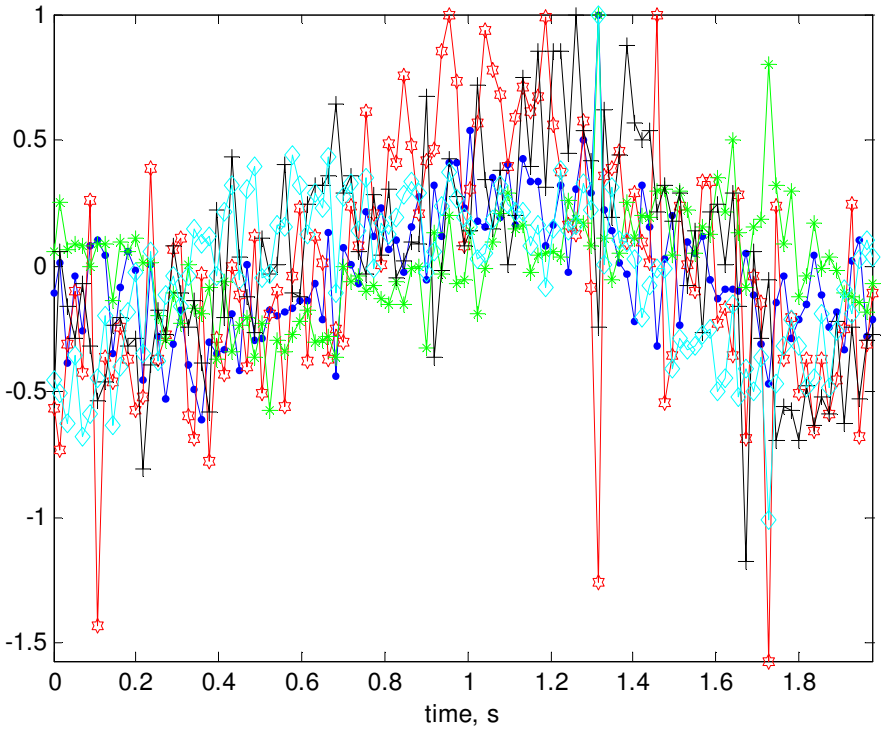

(b)

Figure 7.13: Second path eliminated slow-time representation of the 5-element array output. All signal amplitudes are normalized to 1. (a)before phase compensation (b)after phase compensation with the first DOA estimate

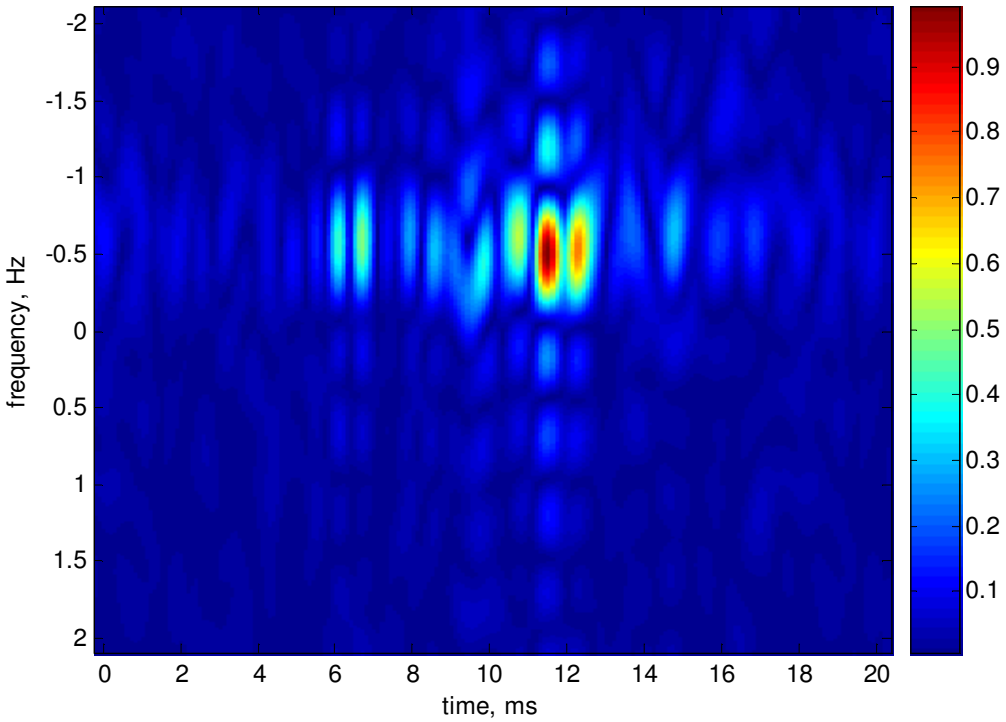

Figure 7.14: Coherently integrated CAFs for the third path.

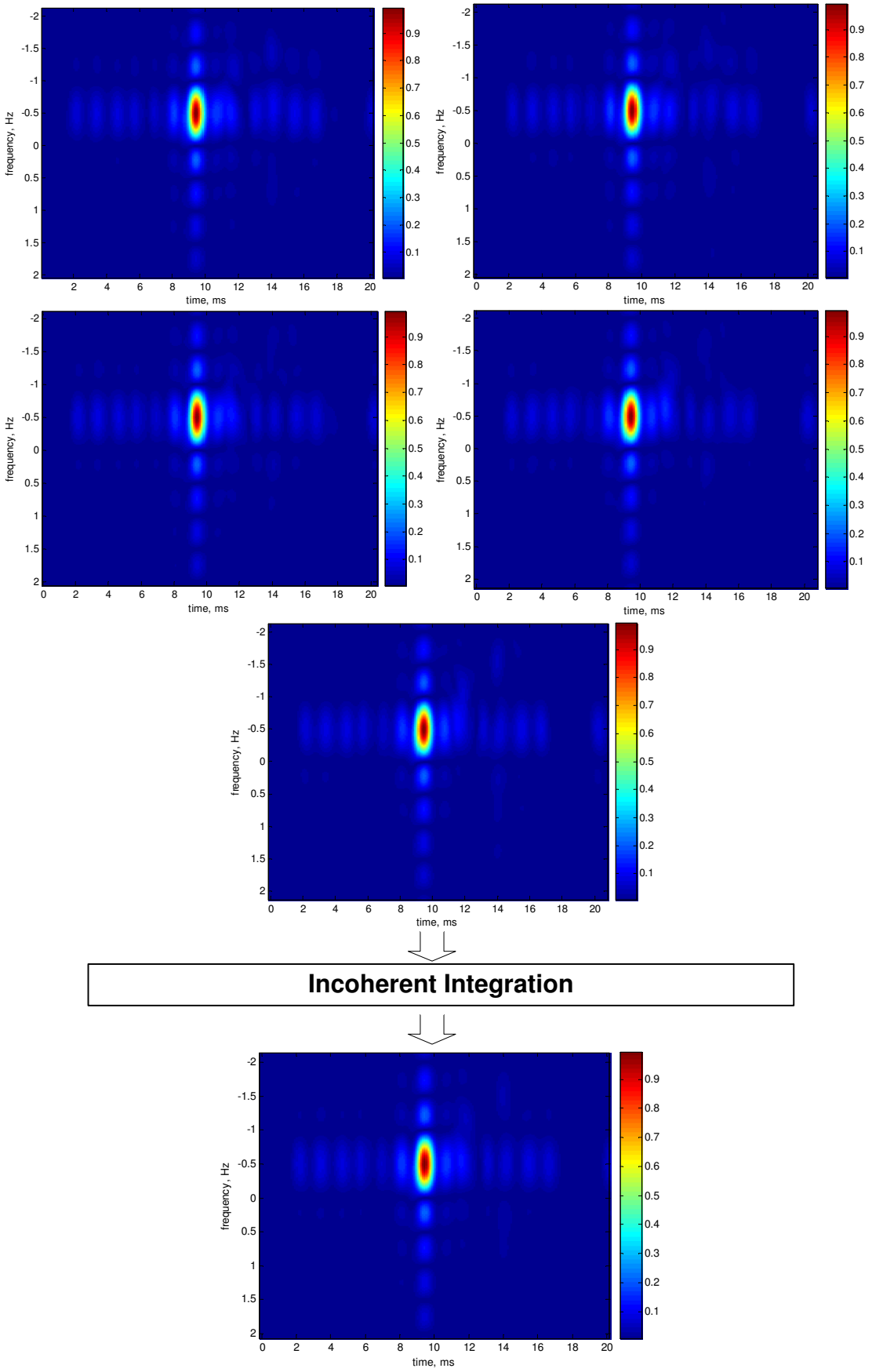

Figure 7.15: Incoherent integration of the CAF surfaces for the strongest path.

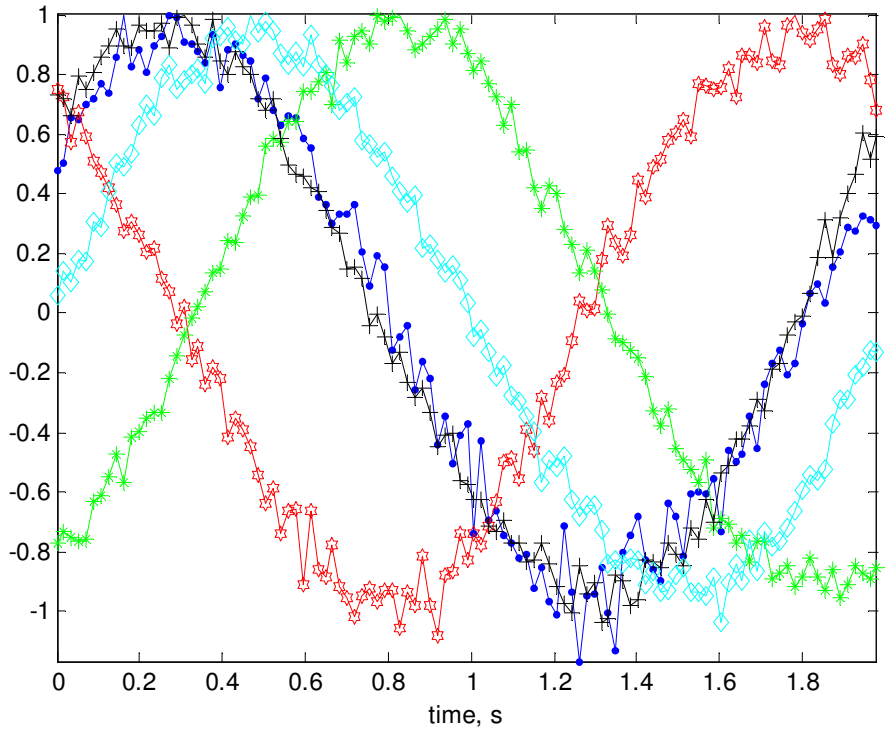

(a)

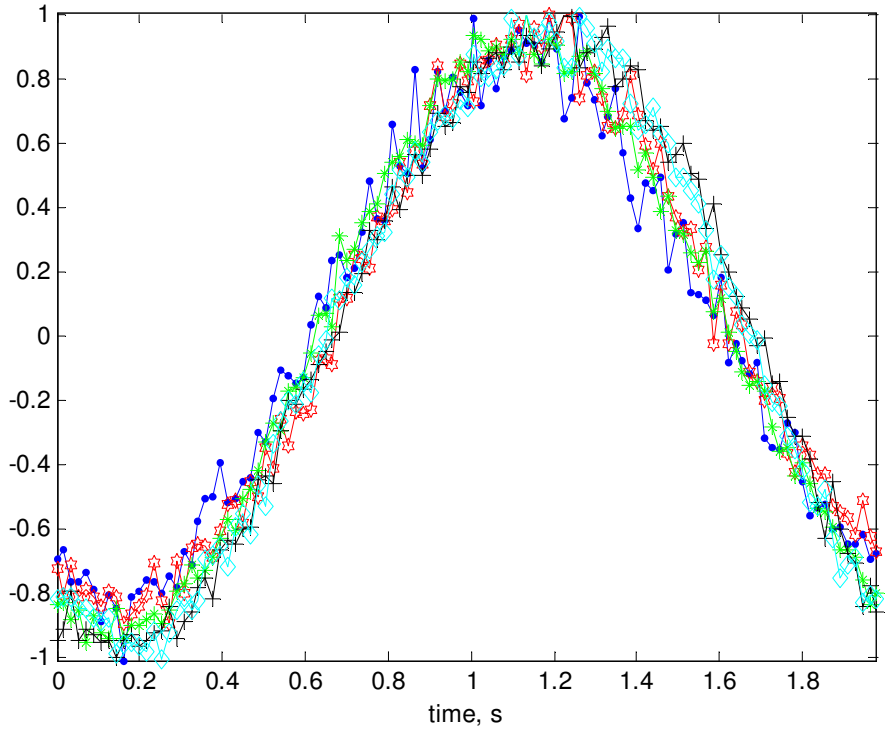

(b)

Figure 7.16: Slow-time representation of the 5-element array output. All signal amplitudes are normalized to 1. (a)before phase compensation (b)after phase compensation with the first DOA estimate

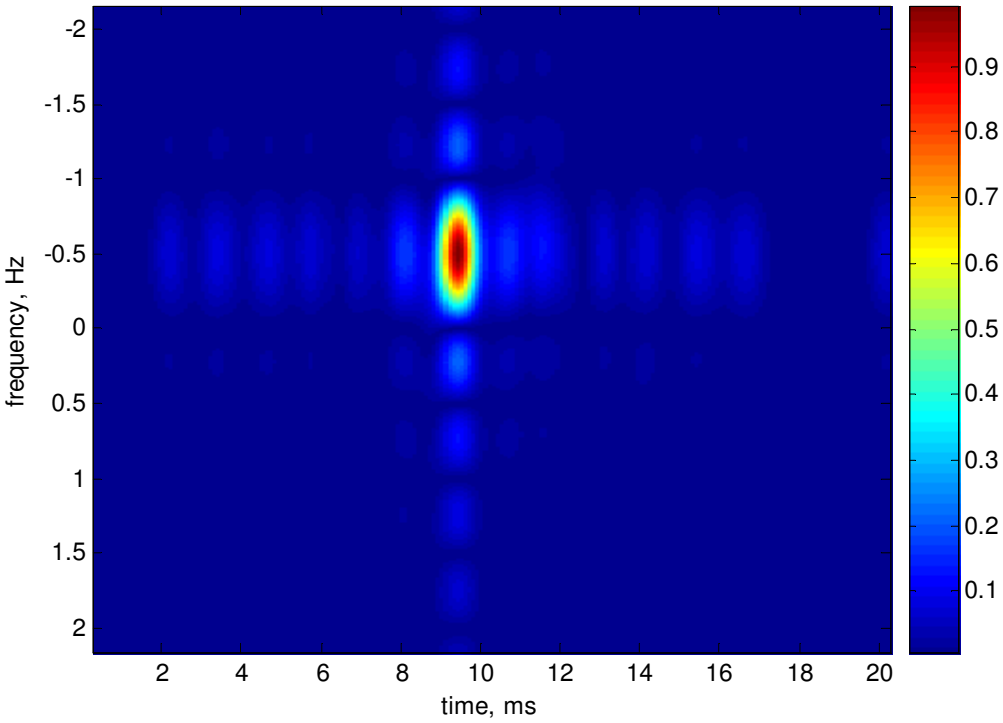

Figure 7.17: Coherently integrated CAFs for the strongest path.

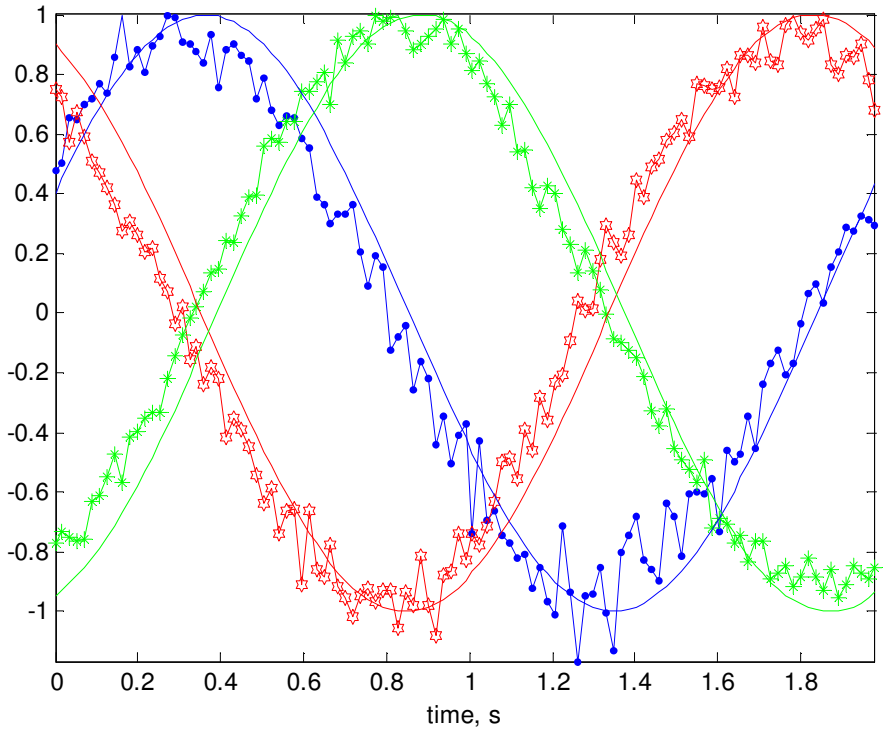

Figure 7.18: Synthetically generated copy of the strongest path at three antenna output with original slow-time data. Marked lines represent the real data and smooth lines for synthetic copy signal. All signal amplitudes are normalized to 1.

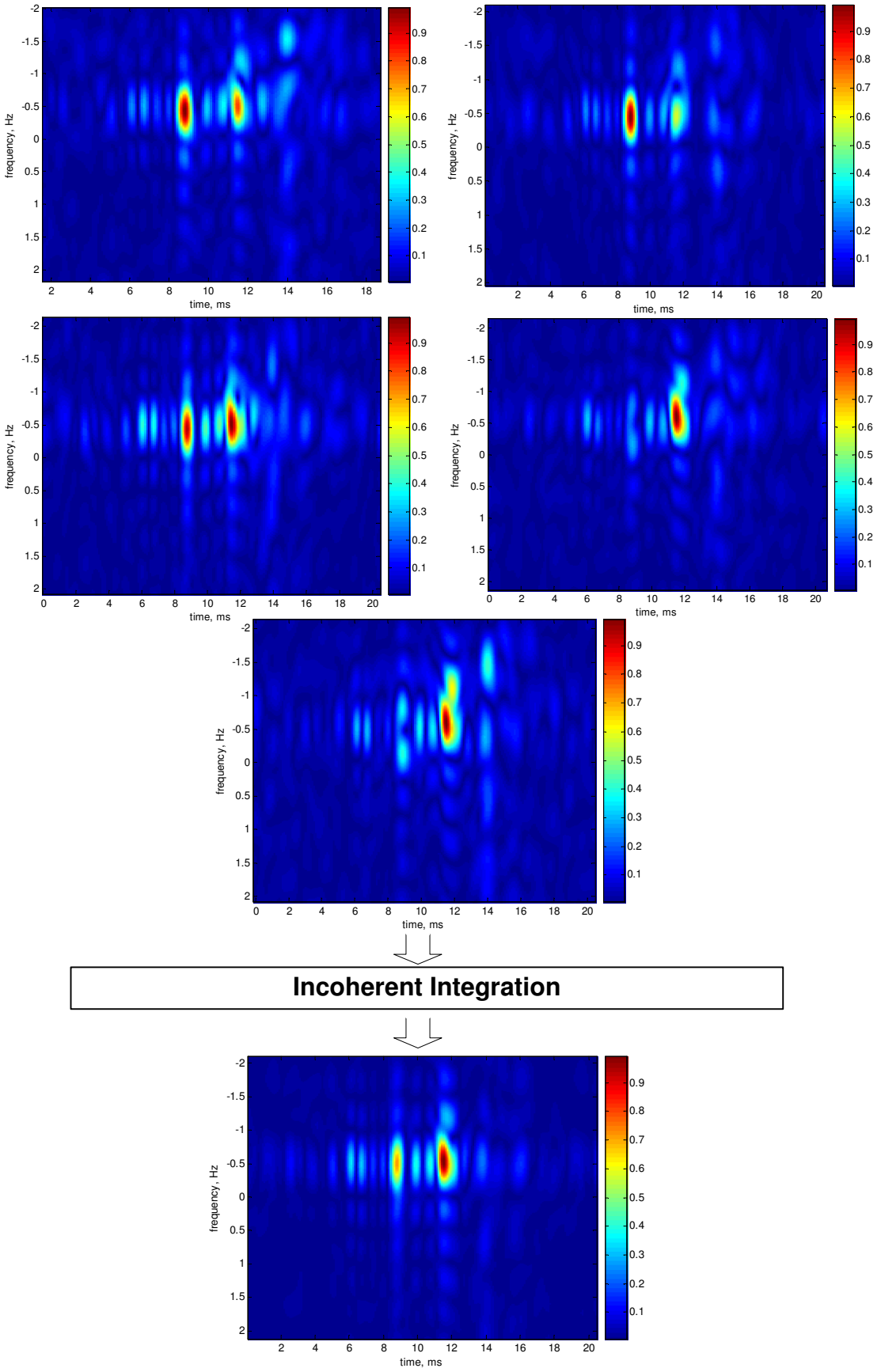

Figure 7.19: Incoherent integration of the CAF surfaces for the second path.

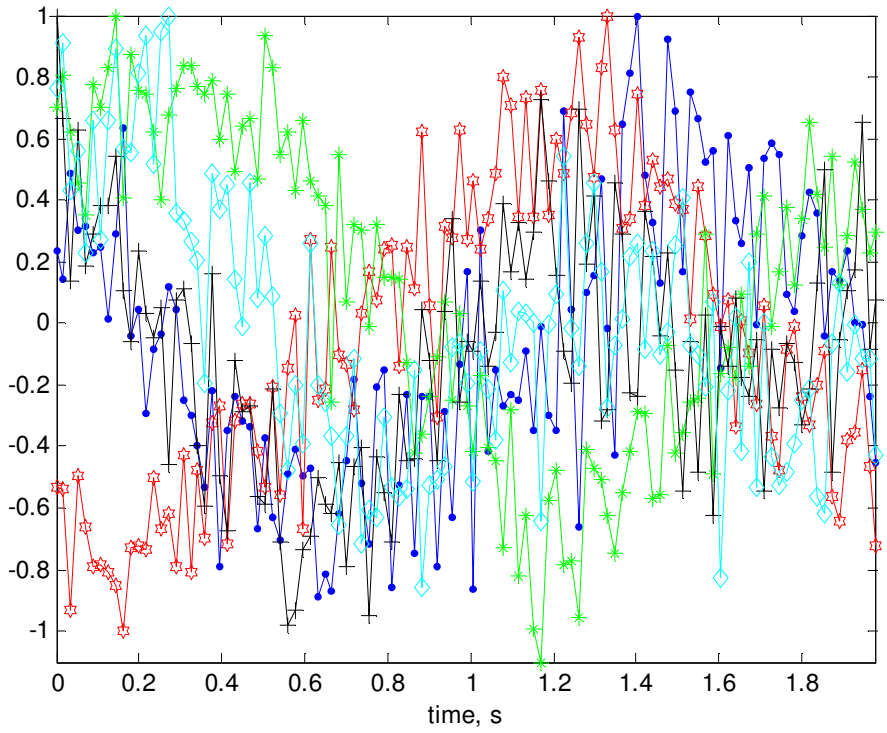

(a)

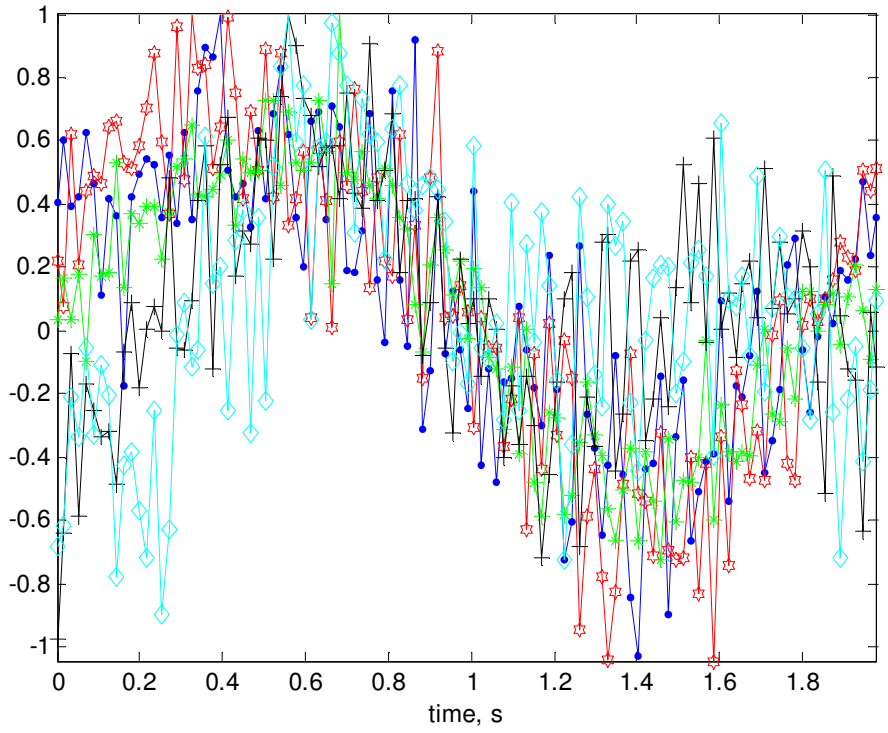

(b)

Figure 7.20: Strongest path eliminated slow-time representation of the 5-element array output. All signal amplitudes are normalized to 1. (a)before phase compensation (b)after phase compensation with the first DOA estimate

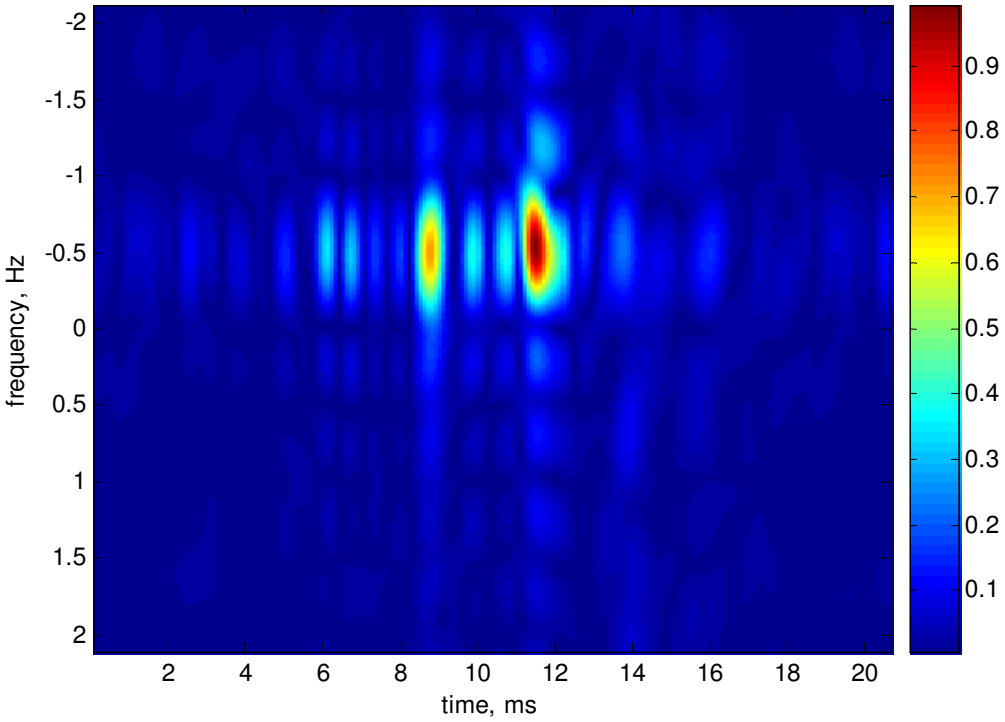

Figure 7.21: Coherently integrated CAFs for the second path.

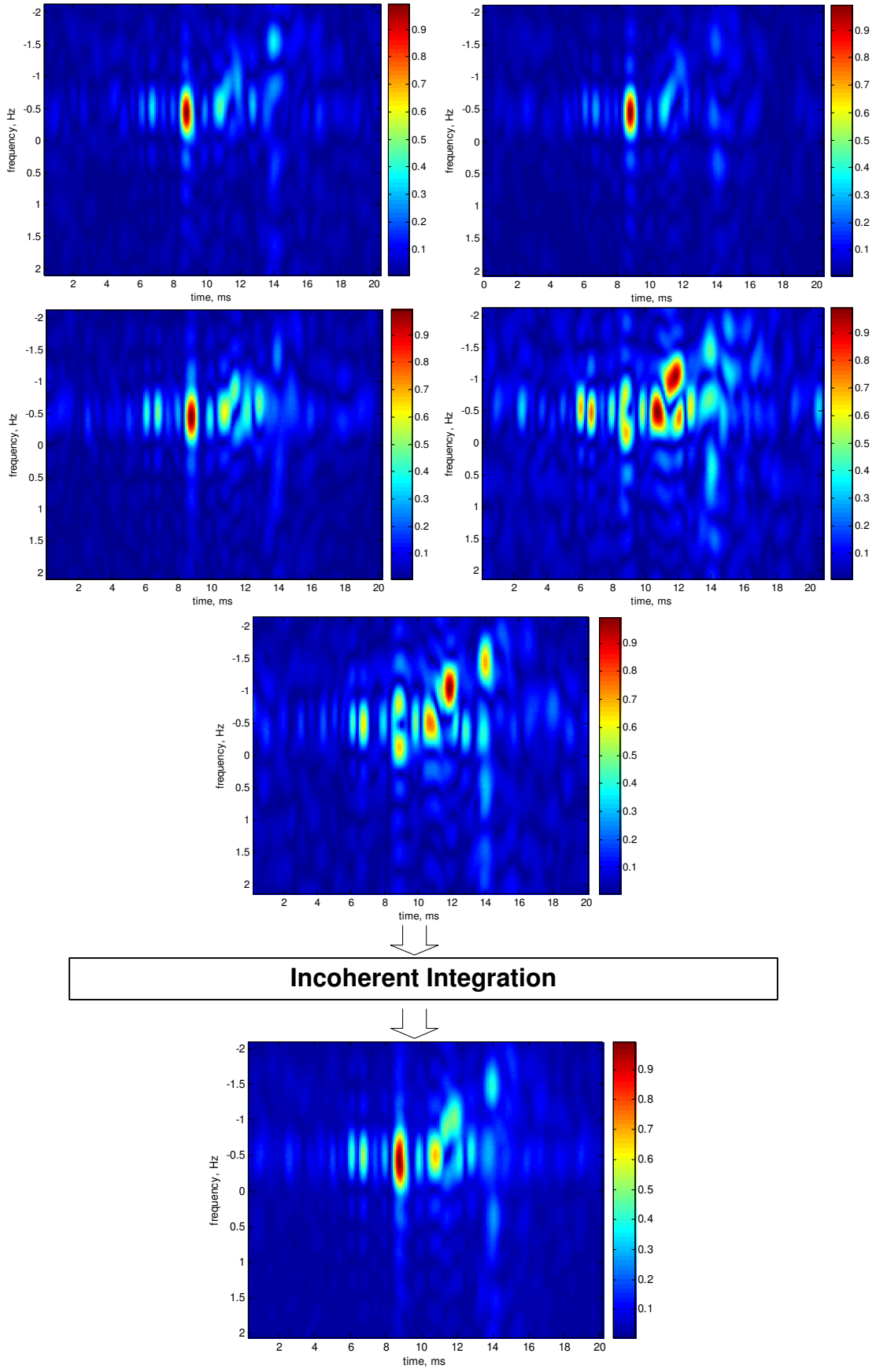

Figure 7.22: Incoherent integration of the CAF surfaces for the third path

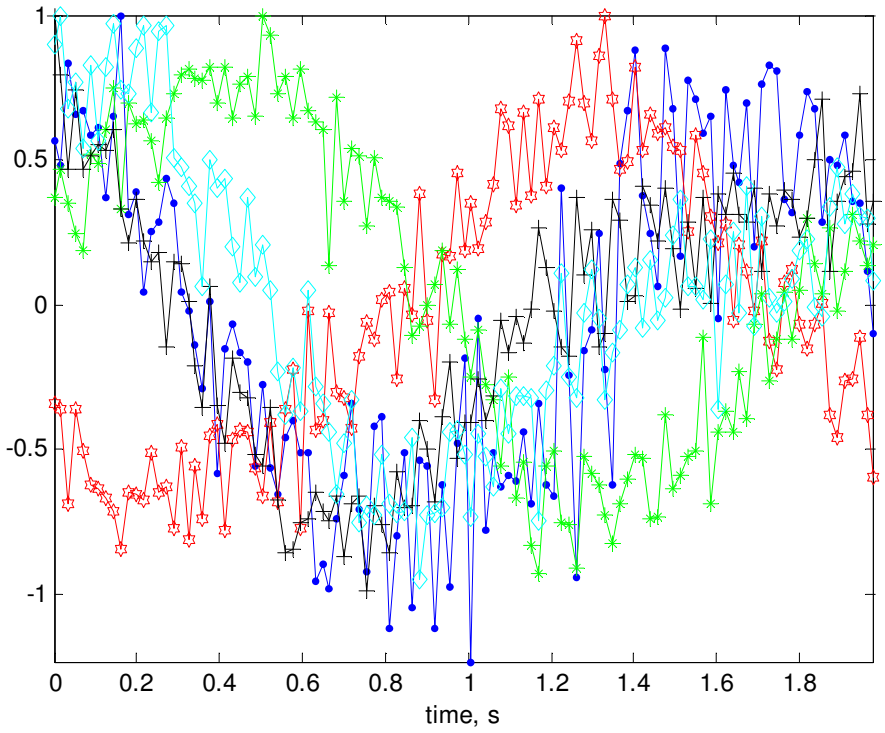

(a)

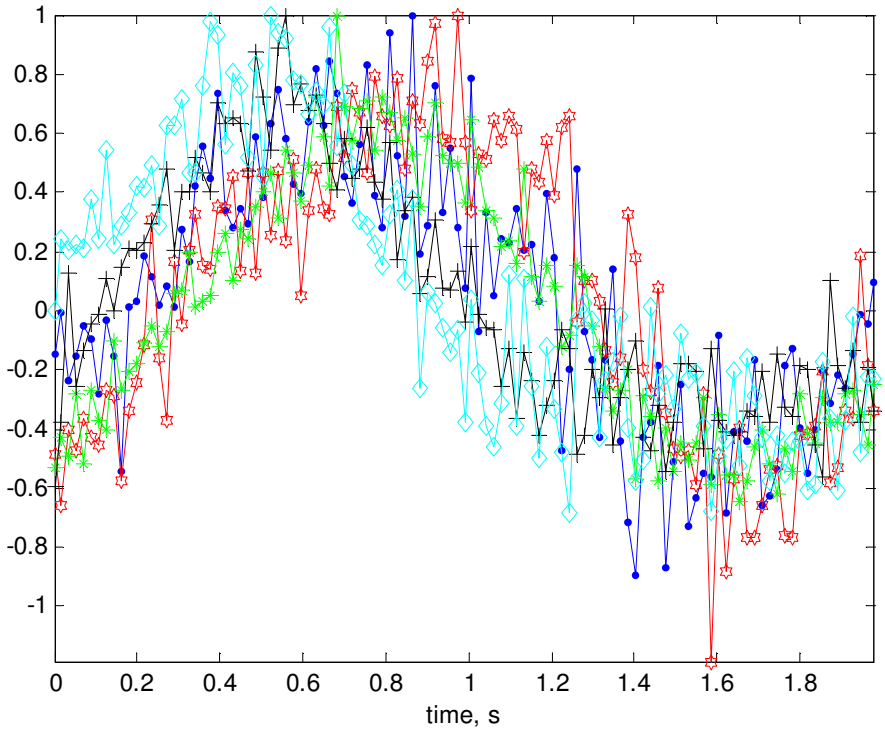

(b)

Figure 7.23: Second path eliminated slow-time representation of the 5-element array output. All signal amplitudes are normalized to 1. (a)before phase compensation (b)after phase compensation with the first DOA estimate

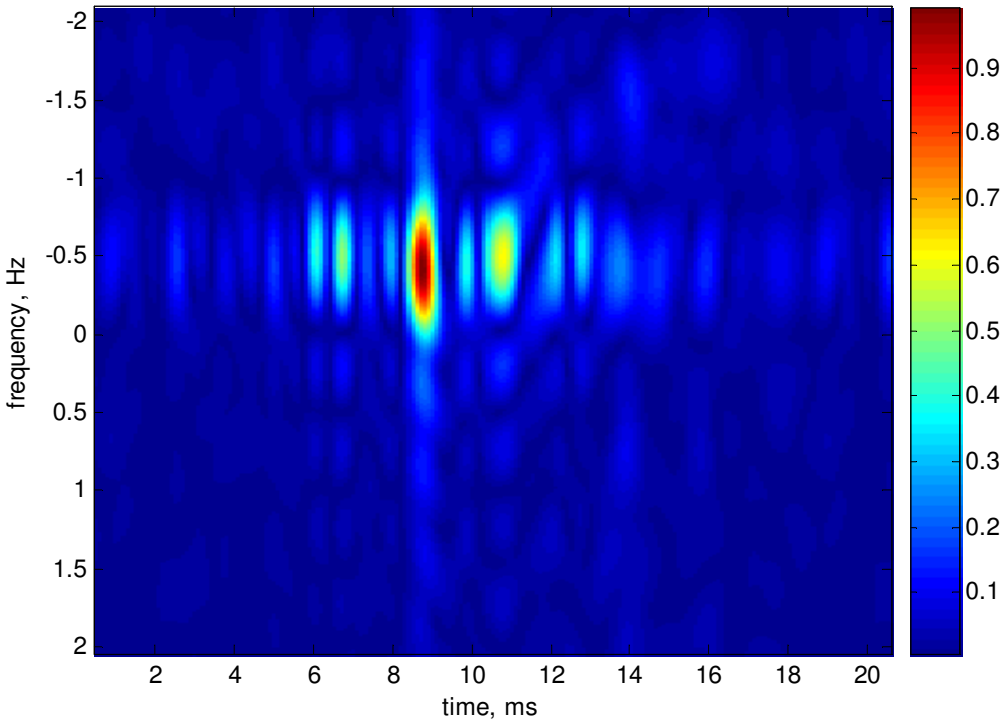

Figure 7.24: Coherently integrated CAFs for the third path.

Chapter 8

CONCLUSIONS and FUTURE WORK

In this thesis, a new array processing technique called as the Cross Ambiguity Function - Direction Finding (CAF-DF) is proposed. The CAF-DF technique estimates DOA, time delay and Doppler shift corresponding to a known transmitted signal impinging on a sensor array. In the case of multipath, the CAF-DF technique provides estimates for the DOAs, delays and Doppler shifts corresponding to each signal path iteratively. Each iteration starts with a CAF computation at the output of each sensor element. Then, using incoherent integration of the computed CAFs, the strongest signal in the delay-Doppler domain is detected. After that, based on the observed phases of the obtained peak across all the sensors, the DOA of the strongest signal is estimated. Using the estimated DOA, signals at the sensor outputs are coherently integrated in order to estimate time delay and Doppler accurately. Finally, the signal whose parameters are estimated is eliminated from the array output to start the next iteration.

The superiority of the proposed CAF-DF algorithm to the MUSIC-based alternatives in several different scenarios is investigated based on simulations.

In the case of a single signal path, especially at low SNRs, CAF-DF performs significantly better than the MUSIC based technique, which is the algorithm of choice in the literature. Even in the scenarios of multipath signals, CAF-DF successively separate each signal path as long as the delays and Doppler shifts of the paths are separable in the cross-ambiguity domain. By using actual ionospheric data recordings, it is shown that the CAF-DF separates existing signal paths better than the MUSIC based alternative described in detail in Chapter 6. In conclusion, the CAF-DF is a powerful and flexible new array signal processing technique that is very useful in the parameter estimation of multipath signals impinging on a sensor array.

Future work on the CAF-DF will be focused on improving the estimation accuracy of the multipath signal parameters by utilizing adaptive search techniques in the DOA plane. For this purpose we are planning to use grids whose dimensions will be a function of the estimated SNR. To further increase the accuracy of the obtained DOA estimates, we will also investigate the polynomial fitting techniques in the vicinity of the observed peak location in the finite resolution search grid. In this way, we believe that the performance of the CAF-DF technique will be very close to the Cramer-Rao lower bound for high SNR cases as well. Furthermore, we will adapt the proposed CAF-DF technique to wireless MIMO communication channels. We expect to obtain significant performance improvements in the estimation of MIMO channel parameters especially for mobile communication.

APPENDIX A

The Cramer Rao Bound

In this appendix derivation of CRB for joint estimation problem is presented. We derive the elements of the Fisher information matrix (FIM) for the case of one signal source. Inverse of the FIM yields the CRB. The log likelihood function can be written as

$$\mathfrak{L} = -MN \log \sigma^2 - \frac{1}{\sigma^2} \sum_{k=1}^{N} \|\boldsymbol{e}(t_i)\|^2 / 2\sigma^2 \tag{A.1}$$

where

$$\boldsymbol{e}(t_k) = \boldsymbol{x}(t_k) - \boldsymbol{\zeta} s(t_k - \tau_0) e^{j2\pi\nu t_k} e^{-j2\pi\nu_c(\boldsymbol{\xi}(\theta,\phi))} \tag{A.2}$$

$$= \boldsymbol{x}(t_k) - \boldsymbol{\zeta} s(t_k - \tau_0) e^{j2\pi\nu t_k} \boldsymbol{a}(\theta,\phi) \quad , \tag{A.3}$$

and N represents number of samples. By differentiation, we get

$$\frac{\partial \mathfrak{L}}{\partial \theta} = \frac{1}{2\sigma^2} \sum_{k=1}^{N} \boldsymbol{x}^H(t_k) \boldsymbol{\zeta} \frac{\partial \boldsymbol{a}(\theta,\phi)}{\partial \theta} s(t_k - \tau_0) e^{j2\pi\nu t_k} \tag{A.4}$$

$$= \frac{1}{2\sigma^2} \sum_{k=1}^{N} \boldsymbol{x}(t_k) \boldsymbol{\zeta}^H \frac{\partial \boldsymbol{a}(\theta,\phi)}{\partial \theta} s^H(t_k - \tau_0) e^{-j2\pi\nu t_k} \tag{A.5}$$

$$= \sum_{k=1}^{N} \frac{1}{\sigma^2} \Re e \left[\boldsymbol{\zeta}^H s^H(t_k - \tau_0) e^{-j2\pi\nu t_k} \frac{\partial \boldsymbol{a}(\theta,\phi)}{\partial \theta} \boldsymbol{e}(t_k) \right] \tag{A.6}$$

$$\frac{\partial \mathfrak{L}}{\partial \phi} = \frac{1}{2\sigma^2}\sum_{k=1}^{N} \boldsymbol{x}^H(t_k)\boldsymbol{\zeta}\frac{\partial \boldsymbol{a}(\theta,\phi)}{\partial \phi}s(t_k-\tau_0)e^{j2\pi\nu t_k} \tag{A.7}$$

$$= \frac{1}{2\sigma^2}\sum_{k=1}^{N} \boldsymbol{x}(t_k)\boldsymbol{\zeta}^H\frac{\partial \boldsymbol{a}(\theta,\phi)}{\partial \phi}s^H(t_k-\tau_0)e^{-j2\pi\nu t_k} \tag{A.8}$$

$$= \sum_{k=1}^{N} \frac{1}{\sigma^2}\Re e\left[\boldsymbol{\zeta}^H s^H(t_k-\tau_0)e^{-j2\pi\nu t_k}\frac{\partial \boldsymbol{a}(\theta,\phi)}{\partial \phi}\boldsymbol{e}(t_k)\right] \tag{A.9}$$

$$\frac{\partial \mathfrak{L}}{\partial \tau} = \frac{1}{2\sigma^2}\sum_{k=1}^{N} \boldsymbol{x}^H(t_k)\boldsymbol{\zeta}\boldsymbol{a}(\theta,\phi)\frac{\partial s(t_k-\tau_0)}{\partial \tau}e^{j2\pi\nu t_k} \tag{A.10}$$

$$= \frac{1}{2\sigma^2}\sum_{k=1}^{N} \boldsymbol{x}(t_k)\boldsymbol{\zeta}^H\boldsymbol{a}(\theta,\phi)\frac{\partial s^H(t_k-\tau_0)}{\partial \tau}e^{-j2\pi\nu t_k} \tag{A.11}$$

$$= \sum_{k=1}^{N} \frac{1}{\sigma^2}\Re e\left[\boldsymbol{\zeta}^H\frac{\partial s^H(t_k-\tau_0)}{\partial \tau}e^{-j2\pi\nu t_k}\boldsymbol{a}(\theta,\phi)\boldsymbol{e}(t_k)\right] \tag{A.12}$$

$$\frac{\partial \mathfrak{L}}{\partial \nu} = \frac{1}{2\sigma^2}\sum_{k=1}^{N} j2\pi t_k\boldsymbol{x}^H(t_k)\boldsymbol{\zeta}\boldsymbol{a}(\theta,\phi)s(t_k-\tau_0)e^{j2\pi\nu t_k} \tag{A.13}$$

$$= \frac{1}{2\sigma^2}\sum_{k=1}^{N} -j2\pi t_k\boldsymbol{x}(t_k)\boldsymbol{\zeta}^H\boldsymbol{a}(\theta,\phi)s^H(t_k-\tau_0)e^{-j2\pi\nu t_k} \tag{A.14}$$

$$= \sum_{k=1}^{N} \frac{2\pi t_k}{\sigma^2}\Im m\left[\boldsymbol{\zeta}^H s^H(t_k-\tau_0)e^{-j2\pi\nu t_k}\boldsymbol{a}(\theta,\phi)\boldsymbol{e}(t_k)\right] \tag{A.15}$$

In order to evaluate the elements of FIM, we will use the following identities whose derivations can be found in [34].

$$E\big[\boldsymbol{e}_j(t_k)\boldsymbol{e}_p^H(t_c)\big] = \delta_{jp}\delta_{kc}\sigma^2 \tag{A.16}$$

$$E\big[\boldsymbol{e}_j(t_k)\boldsymbol{e}_z(t_c)\big] = 0 \tag{A.17}$$

$$E\big[\boldsymbol{e}_j^H(t_k)\boldsymbol{e}_p(t_c)\boldsymbol{e}_n(t_k)\big] = 0 \tag{A.18}$$

$$E\big[\boldsymbol{e}(t_k)\boldsymbol{e}^H(t_k)\boldsymbol{e}(t_j)\boldsymbol{e}^H(t_j)\big] = M^2\sigma^4 + \delta_{t_kt_j}M\sigma^2 \tag{A.19}$$

where $\boldsymbol{e}_j(t_k)$ is the jth component of $\boldsymbol{e}(t_k)$ and δ is Kronecker's delta. Using these identities and from (A.5), we have

$$E\left[\frac{\partial \mathfrak{L}}{\partial \theta}\frac{\partial \mathfrak{L}}{\partial \theta}\right] = \Re e\left[\frac{\partial \boldsymbol{a}^H(\theta,\phi)}{\partial \theta}\frac{\partial \boldsymbol{a}(\theta,\phi)}{\partial \theta}\boldsymbol{\zeta}\boldsymbol{\zeta}^H\sum_{k=1}^{N}\frac{|s(t_k-\tau_0)|^2}{2\sigma^2}\right] \tag{A.20}$$

$$E\left[\frac{\partial \mathfrak{L}}{\partial \phi}\frac{\partial \mathfrak{L}}{\partial \phi}\right] = \Re e\left[\frac{\partial \boldsymbol{a}^H(\theta,\phi)}{\partial \phi}\frac{\partial \boldsymbol{a}(\theta,\phi)}{\partial \phi}\boldsymbol{\zeta}\boldsymbol{\zeta}^H\sum_{k=1}^{N}\frac{|s(t_k-\tau_0)|^2}{2\sigma^2}\right] \tag{A.21}$$

$$E\left[\frac{\partial \mathfrak{L}}{\partial \tau}\frac{\partial \mathfrak{L}}{\partial \tau}\right] = \Re e\left[\boldsymbol{a}^H(\theta,\phi)\boldsymbol{a}(\theta,\phi)\boldsymbol{\zeta}\boldsymbol{\zeta}^H\sum_{k=1}^{N}\left|\frac{\partial s(t_k-\tau_0)}{\partial \tau}\right|^2\frac{1}{2\sigma^2}\right] \tag{A.22}$$

$$E\left[\frac{\partial \mathfrak{L}}{\partial \nu}\frac{\partial \mathfrak{L}}{\partial \nu}\right] = 2\pi^2\,\Re e\left[\boldsymbol{a}^H(\theta,\phi)\boldsymbol{a}(\theta,\phi)\boldsymbol{\zeta}\boldsymbol{\zeta}^H\sum_{k=1}^{N}\frac{|s(t_k-\tau_0)|^2}{\sigma^2}t_k^2\right] \tag{A.23}$$

$$E\left[\frac{\partial \mathfrak{L}}{\partial \tau}\frac{\partial \mathfrak{L}}{\partial \theta}\right] = \Re e\left[\frac{\partial \boldsymbol{a}^H(\theta,\phi)}{\partial \theta}\boldsymbol{a}(\theta,\phi)\boldsymbol{\zeta}\boldsymbol{\zeta}^H\sum_{k=1}^{N}\frac{\partial s(t_k-\tau_0)}{\partial \tau}\frac{s^H(t_k-\tau_0)}{2\sigma^2}\right] \tag{A.24}$$

$$E\left[\frac{\partial \mathfrak{L}}{\partial \tau}\frac{\partial \mathfrak{L}}{\partial \phi}\right] = \Re e\left[\frac{\partial \boldsymbol{a}^H(\theta,\phi)}{\partial \phi}\boldsymbol{a}(\theta,\phi)\boldsymbol{\zeta}\boldsymbol{\zeta}^H\sum_{k=1}^{N}\frac{\partial s(t_k-\tau_0)}{\partial \tau}\frac{s^H(t_k-\tau_0)}{2\sigma^2}\right] \tag{A.25}$$

$$E\left[\frac{\partial \mathfrak{L}}{\partial \tau}\frac{\partial \mathfrak{L}}{\partial \nu}\right] = -\pi\,\Im m\left[\boldsymbol{a}^H(\theta,\phi)\boldsymbol{a}(\theta,\phi)\boldsymbol{\zeta}\boldsymbol{\zeta}^H\sum_{k=1}^{N}\frac{\partial s(t_k-\tau_0)}{\partial \tau}\frac{s^H(t_k-\tau_0)}{\sigma^2}t_k\right] \tag{A.26}$$

$$E\left[\frac{\partial \mathfrak{L}}{\partial \nu}\frac{\partial \mathfrak{L}}{\partial \theta}\right] = -\pi\,\Im m\left[\frac{\partial \boldsymbol{a}^H(\theta,\phi)}{\partial \theta}\boldsymbol{a}^H(\theta,\phi)\boldsymbol{\zeta}\boldsymbol{\zeta}^H\sum_{k=1}^{N}\frac{|s(t_k-\tau_0)|^2}{\sigma^2}t_k^2\right] \tag{A.27}$$

$$E\left[\frac{\partial \mathfrak{L}}{\partial \nu}\frac{\partial \mathfrak{L}}{\partial \phi}\right] = -\pi\,\Im m\left[\frac{\partial \boldsymbol{a}^H(\theta,\phi)}{\partial \theta}\boldsymbol{a}^H(\theta,\phi)\boldsymbol{\zeta}\boldsymbol{\zeta}^H\sum_{k=1}^{N}\frac{|s(t_k-\tau_0)|^2}{\sigma^2}t_k^2\right] \tag{A.28}$$

Bibliography

[1] D. H. Johnson and D. E. Dudgeon, *Array Signal Processing: Concepts and Techniques*. Prentice Halls, N.J., 1993.

[2] J. P. Rossi, J. P. Barbot, and A. J. Levy, "Theory and measurement of the angle of arrival and time delay of uhf radiowaves using a ring array," *IEEE Trans. on Antennas and Propagation*, vol. 45, no. 5, pp. 876–884, 1997.

[3] B. D. V. Veen and K. M. Buckley, "Beamforming: A versatile approach to spatial filtering," *IEEE ASSP Magazine*, vol. 5, no. 2, pp. 4–24, 1988.

[4] R. O. Schmidt, *A Signal Subspace Approach to Multiple Emitter Location and Spectral Estimation*. PhD thesis, Stanford University, 1981.

[5] R. O. Schmidt, "Multiple emitter location and signal parameter estimation," *IEEE Transactions on Antennas and Propagation*, vol. 34, no. 3, pp. 276–281, 1986.

[6] P. Stoica and K. C. Sharman, "Maximum likelihood methods for direction-of-arrival estimation," *IEEE Trans. on Acoustics, Speech and Signal Processing*, vol. 38, pp. 1132–1144, 1990.

[7] J. F. Böhme, "Estimation of source parameters by maximum likelihood and nonlinear regression," *IEEE Proc. ICASSP 84*, pp. 7.3.1–7.3.4, 1984.

[8] B. Ottersten, M. Viberg, and T. Kailath, "Analysis of subspace fitting and ml techniques for parameter estimation from sensor array data," *IEEE Transactions on Signal Processing*, vol. 40, pp. 590–600, 1992.

[9] P. Stoica and A. Nehorai, "Performance study of conditional and unconditional direction-of- arrival estimation," *IEEE Trans. on Acoustics, Speech and Signal Processing*, vol. 38, pp. 1783–1795, 1990.

[10] A. G. Jaffer, "Maximum likelihood direction finding of stochastic sources: A separable solution," *IEEE Proc. ICASSP 88*, vol. 5, pp. 2893–2896, 1988.

[11] A. Jakobsson, A. L. Swindlehurst, and P. Stoica, "Subspace-based estimation of time delays and doppler shifts," *IEEE Trans. on Signal Processing*, vol. 46, no. 9, pp. 2472–2482, 1998.

[12] M. Viberg and B. Ottersten, "Sensor array processing based on subspace fitting," *IEEE Trans. on Signal Processing*, vol. 39, pp. 1110–1121, 1991.

[13] A. Swindlehurst and M. Viberg, "Subspace fitting with diversely polarized antenna arrays," *IEEE Transactions on Antennas and Propagation*, vol. 41, pp. 1687–1694, 1993.

[14] Y. Z. M. G. Amin, A. Belouchrani, "The spatial ambiguity function and its applications," *IEEE Signal Processing Letters*, vol. 7, no. 6, pp. 138–141, 2000.

[15] J. T. G. N. Ma, "Doa estimation for broadband chirp signals," *IEEE Proc. ICASSP*, pp. 261–264, 2004.

[16] C. Helstrom, *Elements of Signal Detection and Estimation.* Wiley, N.J., 1968.

[17] A. Habboosh, R. Vaccaro, and S. Kay, "An algorithm for detecting closely spaced delay/doppler components," *IEEE Proc. ICASSP*, pp. 535–538, 1997.

[18] S. U. Pillai, *Array Signal Processing.* Springer Verlag, N.Y., 1989.

[19] A. Di, "Multiple source location-a matrix decomposition approach," *IEEE Trans. on Acoustics, Speech and Signal Processing*, vol. 33, no. 5, pp. 1086–1091, 1985.

[20] T. J. Shan, M. Wax, and T. Kailath, "On spatial smoothing for directions of arrival estimation of coherent signals," *IEEE Trans. on Acoustics, Speech and Signal Processing*, vol. 33, no. 4, pp. 806–811, 1985.

[21] T. J. Shan, M. Wax, and T. Kailath, "Spatio-temporal spectral analysis by eigenstructure methods," *IEEE Trans. on Acoustics, Speech and Signal Processing*, vol. 32, no. 4, pp. 817–827, 1984.

[22] N. Levanon and E. Mozeson, *Radar Signals.* John Wiley & Sons, N.J., 2004.

[23] M. I. Skolnik, *Introduction to Radar Systems.* McGraw-Hill, N.Y., 2001.

[24] D. K. Barton and S. A. Leonov, *Radar Technology Encyclopedia.* Artech House, N.Y., 1997.

[25] A. J. Viterbi, *CDMA: Priciples of Spread Spectrum Communication.* Addison-Wesley, CA, 1995.

[26] E. G. Ström, S. Parkvall, and B. E. Ottersten, "Near-far resistant propagation delay estimators for asynchronous direct-sequence code division multiple access systems," *Journal of the ACM Processings of the 1994 International Zurich Seminar on Digital Communications*, no. 4, pp. 251–260, 1994.

[27] S. Sakagami, S. Aoyama, K. Kuboi, S. Shirota, and A. Akeyama, "Vehicle position estimates by multibeam antennas in multipath enviroments," *IEEE Trans. on Acoustics, Speech and Signal Processing*, vol. 32, no. 4, pp. 817–827, 1984.

[28] A. J. Fenn, C. J. Diederich, and P. R. Stauferr, "An adaptive-focusing algorithm for a microwave planar phased-array hyperthermia system," *The Lincoln Laboratory Journal*, vol. 6, no. 2, pp. 269–288, 1993.

[29] P. Milanfar, G. Verghese, W. Karl, and A. Willsky, "Reconstructing polygons from moments with connections to arrayprocessing," *IEEE Trans. on Acoustics, Speech and Signal Processing*, vol. 43, no. 2, pp. 432–443, 1995.

[30] J. S. Mosher, R. M. Leahy, and P. S. Kewis, "Biomagnetic localization from transient quasi-static events," *IEEE Proc. ICASSP 93*, vol. 1, pp. 91–94, 1993.

[31] N. Harle and J. Böhme., "Detection of knocking for spark ignition engines based on structural vibrations," *IEEE Int. Conf. on Acoust., Speech and Signal Processing,*, pp. 1744–1747, 1987.

[32] H. Krim and M. Viberg, "Two decades of array signal processing research," *IEEE Signal Processing Magazine*, vol. 13, no. 14, pp. 67–94, 1996.

[33] J. Capon, "High-resolution frequency-wavenumber spectrum analysis," *IEEE Proceedings*, vol. 57, no. 8, pp. 1408–1418, 1969.

[34] P. Stoica and A. Nehorai, "Music, maximum likelihood and cramer-rao bound," *IEEE Trans. on Acoustics, Speech and Signal Processing*, vol. 37, pp. 720–741, 1989.

[35] M. Wax, "Detection and localization of multiple sources in noise with unknown covariance," *IEEE Trans. on Acoustics, Speech and Signal Processing*, vol. 40, no. 1, pp. 245–249, 1992.

[36] M. Viberg and A. Swindlehurst, "Analysis of the combined effects of finite samples and model errors on array processing performance," *IEEE Transactions on Signal Processing*, vol. 42, pp. 3073–3083, 1994.

[37] N. Maslin, *HF Communication A System Approach.* Springer, NY, 1987.

[38] J. M. Goodman, *HF Communications Science and Technology.* Van Nostrand Reinhold, NY, 1992.

[39] L. Rabiner, C. Rader, and R. Schafer, "The chirp z-transform algorithm," *IEEE Transactions on Audio and ElectroAcoustics*, vol. 17, no. 2, pp. 86–92, 1969.

[40] L. Bluestein, "A linear filtering approach to the computation of the discrete fourier transform," *Northeast Electronics Research and Engineering Meeting Record 10*, pp. 218–219, 1968.

[41] N. Davies and P. Cannon, "Damson - a system to measure multipath dispersion, doppler spread and doppler shift on a multi-mechanism communications channels," *Proceedings of AGARD EPP Symposium on Multiple Mechanism Propagation Paths: Their Characterisation and Influence on System Design, Rotterdam*, pp. 36/1–6, 1993.

[42] E. Warrington, "Observations of the directional characteristics of ionospherically propagated hf radio channel sounding signals over two high latitude paths," *IEE Proc.-Microw. Antennas Propag*, vol. 145, no. 5, pp. 379–385, 1998.